TU
Graz

Philipp Breitegger, BSc

Kinetic Monte Carlo Solver
for the Charge Transport in Disordered Solids

MASTER'S THESIS

to achieve the university degree of

Diplom-Ingenieur

Master's degree programme: Technical Physics

submitted to

Graz University of Technology

Supervisor

Dipl.-Phys. Dr.rer.nat. Karin Zojer

Institute of Solid State Physics

Co-Supervisor
Univ.- Prof. Dr. Peter Hadley

Graz, July 2015

AFFIDAVIT

I declare that I have authored this thesis independently, that I have not used other than the declared sources/resources, and that I have explicitly indicated all material which has been quoted either literally or by content from the sources used. The text document uploaded to TUGRAZonline is identical to the present master's thesis dissertation.

_____   _____
Date   Signature

Acknowledgement

First of all I want to thank my supervisor Karin Zojer for giving me the opportunity to work in her group, for teaching me how to investigate scientific problems and for assisting me in structuring my ideas. Chris Groves (Durham University) gave me the opportunity for a research stay in the beautiful city of Durham and always had an open ear when it came to questions regarding the implementation of the KMC code. I further want to thank Peter Hadley for his co-supervision and his experimentalists view on problems.

I also want to thank the colleagues of Karin's group Antón Fernández Fernández and Markus Krammer.

Further I want to thank Egbert Zojer and the (former) members of his group Gernot Kraberger, Lisi Wruß, Elsi Verwüster, Veronika Obersteiner, Iris Hehn, Thomas Taucher, Shashank Harivyasi, Anu Baby, Hermann Edlbauer, and Oliver Hofmann.

I also want to thank my parents and my family for their support, and for giving me the opportunity to study at a university. I want to particularly thank my girlfriend Christine, who cheered me up in the complicated stages of my thesis.

Kurzfassung

In den vergangenen Jahren hat sich die organische Elektronik, im wesentlichen vertreten durch organische Leuchtdioden, am Massenmarkt etabliert. Dennoch, oder gerade deshalb, ist es immer noch von großem Interesse, deren Effizienz zu steigern. Die Effizienz wird besonders von der Ladungsträgerinjektion von den Metallkontakten in den organischen Halbleiter bestimmt. Deshalb ist es von großer Relevanz, die damit verbundenen Effekte zu untersuchen und zu verstehen.

Die derzeitig verfügbaren analytischen Modelle zur Beschreibung von Injektion haben nur einen beschränkten Gültigkeitsbereich bezüglich der Werte die bestimmende Parameter wie Feldstärke, Injektionsbarriere und Grad der Unordnung annehmen können. Das liegt auch daran, dass diese Modelle jeweils nicht alle relevanten Effekte berücksichtigen können. Eine vollständige Beschreibung des gesamten Parameterraums ist daher nur mit Simulationen möglich, die alle relevanten mikroskopischen Effekte berücksichtigen können. Zur Simulation von Ladungstransport in organischen Halbleitern hat sich Kinetic Monte Carlo (KMC) bewährt. Mithilfe dieser Technik lassen sich auch einfache Bauelemente simulieren. Bisher wurde diese Methode jedoch nur unter vereinfachten Annahmen für die Simulation von Injektionsprozessen verwendet. Aus diesem Grund entwickeln wir ein KMC Modell für die Injektion von Ladungsträgern von einer Metallelektrode in einen organischen Halbleiter, welches über bisherige Simulationen hinausgeht indem es neben thermisch aktiviertem Hüpfen auch die Coulomb-Coulomb Wechselwirkungen zwischen den Ladungsträgern berücksichtigt.

Wir ermitteln die injizierte Stromdichte als Funktion des externen Feldes, der Unordnung und der Injektionsbarriere. Es lassen sich zwei Regime als Funktion des unordnungsabhängigen Stroms identifizieren:

Bei niedrigen Barrieren sammeln sich Ladungsträger durch die attraktive Wechselwirkung mit ihren Spiegelladungen an der Grenzfläche an. Die elektrostatische Wechselwirkung mit den so immobilisierten Ladungsträgern führt zur Injektion eines space-charge-limited current (SCLC). Damit ist die Ladungsträgerdichte im Halbleiter konstant und unabhängig von der Barrierenhöhe. Daraus ergibt sich einerseits nur ein vernachlässigbarer Unterschied zwischen den Strom-Feld Kurven bei sehr kleinen Barrieren. Andererseits bricht der Strom für größere Unordnung ein, da auch die Mobilität durch tiefe Traps stark verringert wird. Bei hohen Barrieren identifizieren wir einen Effekt, der durch die unmittelbare Nähe von in der Grenzfläche an der Elektrode akkumulierten Ladungsträgern ausgelöst wird. Die Energie naher Ladungsträger wird derart angehoben, sodass diese tiefer in den Halbleiter hüpfen können. Dieser Effekt führt zu einer Stromzunahme bei zunehmender Unordnung. Wir zeigen außerdem, dass die Injektionsbarriere durch Unordnung verringert wird. Durch die Ergänzung eines klassischen Ausdrucks für die Stromdichte mit einem einfachen Exponentialfaktor kann diesem Effekt allerdings auch hier Rechnung getragen werden.

Abstract

During the last years, organic devices have reached market maturity. Therefore, the improvement of the performance of these devices, such as organic light-emitting diodes and transistors, is in the focus of present research. A crucial process to the performance is the injection of carriers from the metal contacts into the organic semiconductor. Therefore, the study of the underlying processes and its description in a comprehensive model is of high interest.

The behaviour of the injecting contact is expected to be qualitatively different from a Schottky contact to inorganic, doped semiconductors. Current analytical models aiming at describing a metal - organic semiconductor interface are valid in limited ranges of values the parameters, i.e., the electric field, the injection barrier, and the width of the density of states (representing random disorder), can adopt.

Moreover, present models fail to consider all relevant microscopic effects such as the Coulomb-Coulomb-interactions between the charges in one single model. A comprehensive description can be achieved best by simulations which are able to directly consider all relevant microscopic effects. To do so, we utilize the Kinetic Monte Carlo (KMC) technique which was successful to describe systems as large as small devices. However, those simulations remained either incomplete due to partial neglect of interactions, or considered entire devices and, thus, did not permit a clear discrimination of injection-related effects.

We therefore develop a model for the charge injection from a metal electrode into a disordered organic semiconductor. In our approach, we go beyond the only present KMC implementation of injection by incorporating Coulomb-Coulomb-interactions up to a cut-off radius.

By determining the current density over a wide range of parameters, we are able to identify two regimes that determine the dependence of the injected current density on the degree of disorder within the organic semiconductor. In both regimes, i.e., for all barrier values considered, there is a profound accumulation of charges at the metal-organic interface. The regime changes as a function of the barrier value:

For low values of the barrier, charges accumulate in the first layer adjacent to the metal surface due to the interactions with their image charges. The interaction with the such immobilized charges leads to the injection of a space-charge-limited current, associated to a charge-carrier density in the bulk being almost constant over all fields.

A second regime is established for high barrier values ($0.4 \leq \Delta \leq 0.7$ eV). There, the current density increases with disorder, despite the low charge-carrier density at the interface. We are able to explain this behaviour by a disorder-induced lowering of the barrier as well as a "proximity effect". For low barriers, the main event is hopping between the metal and the first organic layer. By that, disorder increases the likelihood that these charges moving in a ping-pong fashion, approach nearest neighbour particles and, in doing so lift their energy, such that they can easily hop further into the bulk.

Contents

1 Introduction

It is known that injection of carriers from a metal contact into an organic semiconductor is crucially determining the performance of organic devices, particularly that of organic light-emitting diodes and transistors. Therefore, the study of the underlying processes and its description in a comprehensive model is of high interest.

The behaviour of the injecting contact is expected to be qualitatively different from a Schottky contact to inorganic, doped semiconductors, as pristine organic semiconductors are, in essence, insulators often possessing a large degree of energetic disorder. As a consequence, organic electronic devices work only if charge carriers are additionally provided, either by injection or by photogeneration.

Current analytical models fall short in the description of injection, as the corresponding critical parameters, i.e., the electric field, the injection barrier, and the width of the density of states (representing random disorder), can adopt a wide range of values. While the injection barrier can vary between 0 and, typically, 1 eV, relevant fields can vary by four orders of magnitude. Moreover, many models fail to incorporate all relevant contributions to net injection. Attempts to explain injection using microscopic KMC simulations remained either incomplete due to partial neglect of interactions (cf. Ref. [1]), or considered entire devices (cf. Ref. [2] and Ref. [3]) and, thus, did not permit a clear discrimination of injection-related effects.

A comprehensive description can, hence, be best achieved by simulations which are able to directly consider all relevant microscopic effects. As we are interested in macroscopic observables, such as the current density, molecular dynamics (MD), Kinetic Monte Carlo (KMC), or drift-diffusion (DD) models might be considered. DD has been shown to be very successful in, e.g., simulating systems of the size of transistors (cf. Ref. [4] and Ref. [5]). The method relies on effective parameters, due to local averaging. By that, microscopic insight is lost. That makes it particularly difficult to describe the region close to the injecting electrode of a transistor. On the other hand, according to Ref. [6], MD simulations would be computationally too costly, when it is aimed to simulate systems of the size we are interested in. KMC, on the other hand, has proven to describe systems of the size of small devices with sufficient accuracy. [1–3]

It is, therefore, the goal of this thesis, to directly explore injection by means of a well-defined model system consisting of an interface between a metal and a disordered semiconductor. Both components are assumed to be spatially homogeneous and their interface to be sharply defined. We will study the injected current across the interface between a metal and an organic semiconductor as a function of the energetic disorder and the superimposed electric field by using Kinetic Monte Carlo.

By varying these parameters, we expect to observe and comprehend the borderline cases that are insufficiently described by the state-of-the-art analytical models in Chapter 2.2. The findings are to be used in the DD simulation of transistors and other more complex devices.

2 Review of the Literature

The aim of this chapter is to give an overview of present works that model injection of charges from a metal into an organic semiconductor and develop arguments, as to why a further investigation of injection with Kinetic Monte Carlo (KMC) is promising. First, an introduction in injection mechanisms is given. Then, an overview of analytical and KMC models follows. Finally, a justification of the importance to go beyond present models is given.

2.1 Introduction

In the context of "classical" metal-semiconductor junctions, so-called Schottky contacts can be formed in which charges need to overcome a barrier to enter the semiconductor. A contact between a metal and a semiconductor results in the formation of a potential barrier. In thermal equilibrium, the Fermi levels of the metal and the semiconductor align and a barrier $\Delta = q(\phi_m - \chi)$ forms as a result of the work function difference between the metal ϕ_m and the semiconductor χ. Injection describes the process to overcome this barrier.[**pp.245**, 7]

The ideas of the "classical" junctions lend the description being used for injection from a metal contact into an organic semiconductor. Here, the barrier Δ is the energy difference between the Fermi level in the metal E_F and the transport level of the organic semiconductor (cf. Figure 2.1, where the equilibrium transport level is shown as a red dashed line).

The potential energy of an electron at a distance x from the electrode is a superposition of the injection barrier Δ, the potential due to the external field F_{ext}, and the Coulomb binding energy of a particles own image charge as described by Equation 2.1:

$$E_{pot}(x) = \Delta - eF_{ext}x - \frac{e^2}{16\pi\epsilon_r\epsilon_0 x},$$ (2.1)

where e is the elementary charge and ϵ_r and ϵ_0 are the relative and the vacuum permittivity. The resulting potential energy as due to Equation 2.1 is shown as a blue line in Figure 2.1), where the position of the metal is indicated with a gold surface on the left.

Due to the shape of the potential energy, described by Equation 2.1, the resulting injection barrier Δ' (cf. Figure 2.1) is effectively lower than Δ, which is known as the Schottky effect[8] and given by:

$$\Delta' = \Delta - \sqrt{\frac{F_{ext}e^3}{4\pi\epsilon_r\epsilon_0}},$$ (2.2)

with the parameters as previously defined.

There are two major mechanisms to realize injection:

The first is tunnelling, which was originally used for the description of field emission into vacuum and is relevant at high fields and large barriers only. This mechanism is neither considered in the analytical models discussed here, nor directly in the KMC models.
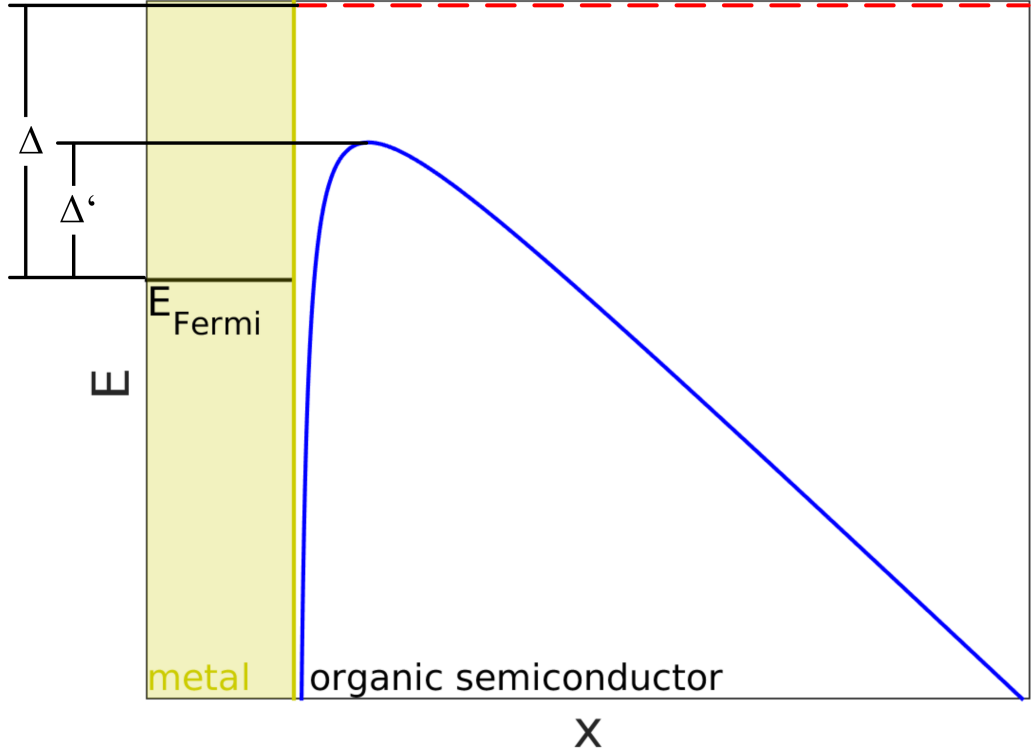
Figure 2.1: Potential energy $E(x)$ (blue) of the transport level in the organic semiconductor due to the Schottky effect as a function of the distance from the metal electrode (gold). The transport level in absence of any image charge and externally applied field is depicted in red (dashed), where a barrier Δ forms between the transport level and the Fermi level E_F (black line in the metal). Due to the Schottky effect, the effective barrier is Δ'.

The second mechanism is thermionic emission, which was originally used to describe glow emission into vacuum. It was used for describing thermionic emission into a semiconductor [**pp.245**, 7] and further adopted for the description of the injection into an organic semiconductor [8]. In the form it is used for organic semiconductors, it describes thermally activated hops across an injection barrier giving rise to a current density

$$j_{RS} = A^* T^2 \exp\left(-\frac{\Delta'}{k_B T}\right), \tag{2.3}$$

where T is the temperature, k_B Boltzmanns constant, and Δ' the reduced injection barrier, given by Equation 2.2. The effective Richardson constant A^* is defined by the following equation [8]:

$$A^* = \frac{4\pi m^* k_B^2}{h^3}. \tag{2.4}$$

Here, h is Planck's constant and m^* the effective mass of the electron, which is somewhat difficult to define in the absence of band structures, i.e., for a disordered material.

Equation 2.3 considers the current density when a single electron is injected into the conduction band. In case of injection into an organic semiconductor, the following effects are not covered with the thermionic emission current (Equation 2.3):

1. organic materials posses localized, electronic states with energetic disorder; low lying states might trap carriers in the bulk

2. charge accumulation (space charge effects) close to the interface due to the image charge of the injected electron and other electrons present

3. a current flowing back to the electrode, being influenced by the above considerations

4. an influence on the current due to the Coulomb-Coulomb- interaction between particles in the bulk

Keeping these effects in mind, macroscopic and KMC models of present publications will be discussed in the following chapters.

2.2 Present modelling approaches of injection

Thermionic emission and recombination current

Scott and Malliaras developed a model for the net current injected from a metal into an organic semiconductor. [9] The main idea is to identify a current expression from the metal into the organic semiconductor and, vice versa, from the organic semiconductor into the metal. It results from translating transport equations known from crystalline semiconductors with delocalized states to amorphous semiconductors with localized states. In former, states in the conduction band are de-localized, whereas in latter, the states are localized.
As the final result, the current density for an applied field F_{ext} reads as

$$j_{SM} = 4\Psi(f)^2 N_0 e \mu F_{ext} \exp\left(-\frac{\Delta}{k_B T}\right) \exp\sqrt{f(F_{ext})}. \tag{2.5}$$

Here, N_0 is the site density and μ the mobility of the organic semiconductor. The field dependent function $f(F_{ext})$ in Equation 2.5, is given by

$$f(F_{ext}) = \frac{e F_{ext} r_c}{k_B T} \tag{2.6}$$

with e the elementary charge, r_c the Coulomb capture radius as given by Equation 2.9 below, and $\Psi(f)$, where f is $f(F_{ext})$ as defined above, given by

$$\Psi(f) = f^{-1} + f^{-1/2} - f^{-1} \cdot \left(1 + 2f^{1/2}\right)^{1/2}. \tag{2.7}$$

The other parameters are as previously defined.
The comparison of the Scott and Malliaras current density to the expression due to thermionic emission (Equation 2.3) yields remarkably:

1. Equation 2.5 contains the same reduced barrier height given by Equation 2.2, as the thermionic emission given by Equation 2.3 due to the factor $\exp\sqrt{f(F_{ext})}$.

2. Equation 2.5 contains a $T-$dependent prefactor $\Psi(f)^2$ being proportional to T^2. [9]

3. The current density j is directly proportional to the mobility μ.

Equation 2.5 roots on the idea to utilize Langevin theory to describe the net current density j_{SM} as a superposition of j_{inj} and j_{rec}:

$$j_{SM} = j_{inj} - j_{rec}. \tag{2.8}$$

The current density j_{rec} is caused by a recombination of charges with their images in the metal whose energy is $k_B T$ lower than the field dependent maximum of the potential energy (cf. Figure 2.1). Those charges get attracted to the electrode and ultimately recombine. For the zero field case, the distance from the metal surface up to which electrons recombine is given by $x_c = r_c/4$, where r_c is the Coulomb capture radius[9]:

$$r_c = \frac{e^2}{4\pi\epsilon_r\epsilon_0 k_B T} \tag{2.9}$$

This distance x_c, however varies when an external field F_{ext} is applied. This variation is described by $\Psi(f)$, given by Equation 2.7.
The recombination current finally reads as

$$j_{rec} = n_0 e \mu F(x_c),$$

with n_0 the charge-carrier density at the interface due to injection (depending on $\Psi(f)$) and μ the carrier mobility.
The current density j_{inj} is assumed to arise from thermionic injection(cf. Equation 2.3). Demanding detailed balance at thermal equilibrium, i.e.,

$$j_{SM} = j_{inj} - j_{rec} = 0,$$

the effective Richardson constant is derived as $A^* = \frac{16\pi\epsilon\epsilon_0 k_B^2 N_0 \mu}{e^2}$.
The main insights with respect to the thermionic emission model in Equation 2.3 are that (1) the current density j_{SM} is directly proportional to the carrier mobility μ and (2) that the effective Richardson constant A^* is much smaller than for the free electron case.

The authors mention that a more accurate result could be found by using a field dependent mobility μ at the field at $x_c(F_{ext})$.
Despite the addition of a field dependent recombination current and the derivation of an effective Richardson constant, the model lacks desirable features needed for a sufficient description of injection. Neither does the model (1) consider disorder or the slope of the density of states, nor are (2) space charge effects or (3) interactions between the injected particles and non-mutual images taken into account. Also, the final result of Equation 2.5 does not describe the case of a negative field applied. Barker *et al.* adopted the model to allow for non-zero current at zero and negative fields[10] in organic photovoltaic (OPV) devices. However, they had to rely on an intermediate expression derived by Scott and Malliaras and accounted for an increase in the barrier for negative fields.

Macroscopic description of injection due to hopping

In the work of Arkhipov *et al.* [11] an analytical expression for the injection current of a metal-organic contact is derived. The organic material is assumed of having a Gaussian DOS of width σ. A barrier of the shape following Equation 2.1 on page 13 is assumed, i.e., a superposition of the injection barrier Δ, the external field F_{ext}, and the Coulomb binding energy of a particles own image charge.
The main idea is now to view injection as a two step process rather than a single jump

of sufficient energy.

The first step is a jump from the metal into the (localized) state in the organic, and the second step a random walk. The latter is approximated by a continuous drift. The first hop, on the other hand is based on the Miller - Abrahams rate equation, used for waiting time calculations in KMC models (cf. Equation 3.7 on page 27).

According to the authors, the current density is dominated by one rate-limiting hop into the organic, i.e., that hop might be (a) up or (b) down in energy as depicted in Figure 2.2. Each case gives rise to an individual expression for the current I.
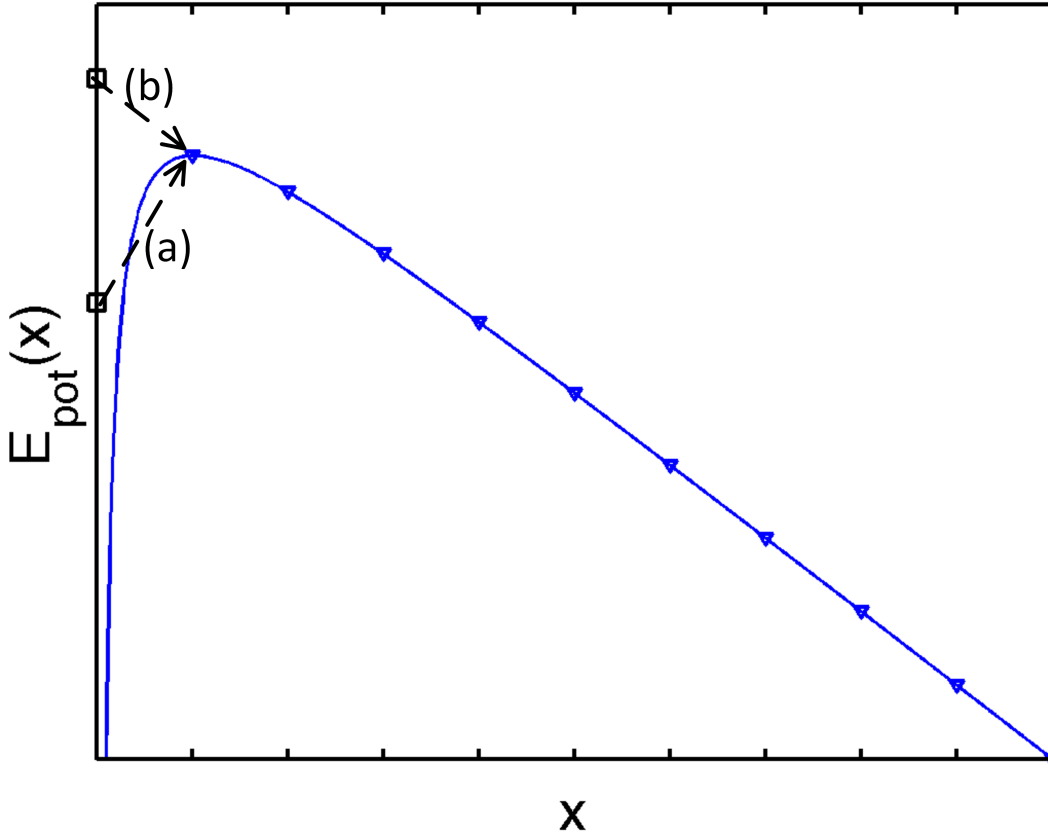

Figure 2.2: Potential energy $E(x)$ (blue) of the transport level in the organic semiconductor assuming vanishing disorder ($0 \, k_B \cdot T$), due to the Schottky effect as a function of the distance x from the electrode. Triangles mark the discrete levels of the hopping sites. Depending on the Fermi level (black squares, left), the rate-limiting hop can be (a) up or (b) down in energy.

For the case of upward jumps being rate limiting, the value of the barrier Δ fulfils the following inequality:

$$\Delta > eF_{ext}a_{latt} + \frac{e^2}{16\pi\epsilon_r\epsilon_0 a_{latt}} + \sigma\sqrt{2\ln\left(\frac{9\sqrt{\pi}}{2\sqrt{2}}\left(\frac{\sigma N_0^{1/3}}{k_B T\gamma}\right)^3\right)}. \qquad (2.10)$$

Here, a_{latt} is the lattice constant of the bulk (i.e. the smallest distance a particle can hop) and γ the overlap factor as described on page 27. All other constants are as previously defined. The condition can be understood, when recalling Equation 2.1 for

the potential energy:

$$E_{pot}(x) = \Delta - eF_{ext}x - \frac{e^2}{16\pi\epsilon_r\epsilon_0 x},$$

and equating x to the shortest initial jump distance a_{latt}. Then, it tells us, that the initial jump is up in energy, if the barrier is higher (i.e. the Fermi energy is lower) than the potential energy at the shortest jump distance plus a disorder σ dependent lowering of that potential energy. The resulting current, with the initial jump over the distance x_0 into a site with the energy E', is derived as:

$$\begin{aligned}
I = e\nu_0 &\frac{1}{\int_{a_{latt}}^{\infty} \exp\left(-\frac{e}{k_B T}\left(F_{ext}x + \frac{e}{16\pi\epsilon_r\epsilon_0 x}\right)\right)dx} \\
&\cdot \int_{a_{latt}}^{\infty} \exp\left(-2\gamma x_0\right)dx_0 \\
&\cdot \int_{a_{latt}}^{x_0} \exp\left(-\frac{e}{k_B T}\left(F_{ext}x + \frac{e}{16\pi\epsilon_r\epsilon_0 x}\right)\right)dx \\
&\cdot \int_{-\infty}^{\infty} \mathrm{Bol}\,(E')P(E_{pot}(x_0) - E'|0,\sigma)dE'
\end{aligned} \tag{2.11}$$

where ν_0 is the attempt frequency, known from the Miller - Abrahams rate equation (Equation 3.7), $g(\epsilon_i|\bar{\epsilon},\sigma)$ is the Gaussian distribution given by Equation 3.9 and $\mathrm{Bol}\,(E)$, the Boltzmann distribution, given by equation Equation 2.12:

$$\mathrm{Bol}\,(E) = \begin{cases} \exp\left(-\frac{E}{k_B T}\right) & E > 0 \\ 1 & E < 0. \end{cases} \tag{2.12}$$

For the case of downward jumps being rate limiting, i.e., the first hop is down in energy or isoenergetic, the following condition needs to be fulfilled:

$$\Delta \le eF_{ext}a_{latt} + \sqrt{\frac{eF_{ext}}{4\pi\epsilon_r\epsilon_0}} + \sigma\sqrt{2\ln\left(\frac{9\sqrt{\pi}}{2\sqrt{2}}\left(\frac{\sigma N_0^{1/3}}{k_B T\gamma}\right)^3\right)}. \tag{2.13}$$

The condition can be understood, when recalling Equation 2.2 for the barrier lowering:

$$\Delta' = \Delta - \sqrt{\frac{F_{ext}e^3}{4\pi\epsilon_r\epsilon_0}}.$$

Then, it tells us, that the Fermi level is higher than the effective injection barrier Δ' plus a disorder σ dependent lowering of Δ'. Hence, the first jump will already be down in energy. The resulting current is then derived as:

$$I = e\nu_0 \exp\left(-2\gamma\left(\frac{3}{2\pi N_0}\right)^{1/3} \mathrm{erfc}\left(\frac{\left(\Delta - e\sqrt{\frac{eF_{ext}}{4\pi\epsilon_0\epsilon_r}}\right)^2}{\sqrt{2}\sigma}\right)\right). \tag{2.14}$$

An advantage over other macroscopic models is the consideration of microscopic hopping processes which also include a Gaussian DOS. Also a recombination current back to the electrode is considered by regarding surface recombination. However, neither are

space charge effects (1), nor Coulomb-Coulomb- interactions between non-mutual particles and their images regarded (2). Another major drawback is, (3), as will become evident later in this thesis, that Arkhipov *et al.* does not allow for other hopping processes, e.g., between interface and bulk as limiting step. Also, (4), there is no unique equation for all parameter sets.

Macroscopic description based on the local electric field

In the work of Neumann *et al.* [12], a one dimensional analytical model for the charge carrier transport is presented. Here, the main idea is derived from a drift-diffusion perspective.

In steady state, the current density must be constant at all distances from the metal-organic interface.

Being able to describe the current in the bulk of the conductor and the organic semiconductor allows one to derive a condition for the electric field distribution at the contact interface. The model assumes, that charges are arranging within a certain screening length inside the conductor (ranging from $1\,\mathring{A}$ to a few nm - the Thomas Fermi screening length). Those charges will form a space charge region within the conductor. This allows the definition of an electrochemical potential $\kappa(x)$ in the conductor.

Assuming the free electron approximation in the conductor, the electrochemical potential $\kappa(x)$ is derived within the conductor as

$$\kappa(x) = \frac{\hbar^2}{2m_{eff}} \left(3\pi^2 n(x)\right)^{2/3} + e\Phi(x). \tag{2.15}$$

Here, $\hbar$ is the reduced Planck constant, m_{eff} is the effective mass in the conductor, $n(x)$ the charge carrier density and $\Phi(x)$ the electrostatic potential. Finally, an equation for the field in the conductor is derived.

For the organic material, a DOS is introduced only in the sense of a total density of states N in the organic as an integral over the DOS. This quantity is part of the electrochemical potential (cf. Equation 2.16) in the organic semiconductor. It is, however, explicitly stated, that the width of disorder is taken as vanishing, where charge-carrier trapping can be neglected.

$$\kappa(x) = k_B T \ln \frac{n(x)}{N} + \Delta + \kappa_\infty + e\Phi(x). \tag{2.16}$$

In Equation 2.16, κ_∞ is the electrochemical potential at an infinite distance from the conductor-organic interface. All the other constants are as previously defined.

Similar to $\kappa(x)$, also the electric displacement is taken to be continuous within device, leading to two requirements which are used to define the integration constants of the differential equations for the corresponding electric fields in the conductor and the organic material (self-consistency).

Using these two conditions, a non-linear differential equation for the field in the organic is derived. The analytical solution of the latter equation is investigated for two different cases: the case of thermal equilibrium (no field applied) and the case of steady state (field applied). In both cases, a formation of space charges is observed in the conductor, as well as in the organic.

By specifying a current density j, the equations can be solved for the fields, which, in turn, determine the voltage V. The $j-V$ characteristic of a such calculated steady-state for a 100 nm device is shown in Figure 2.3, for barriers between 0 and 0.4 eV. For the

0 eV barrier, space-charge limited current (SCLC) behaviour $j_{SCLC} \propto V^2$ is observed for all voltages. For the higher barriers a linear voltage dependence is observed between 1 and 10 V. This is said to be due to the space charge region in the bulk. At higher voltages (above 100 V) and high fields, SCLC is observed for all barriers, as the space-charge region moves closer to the electrode and finally vanishes.
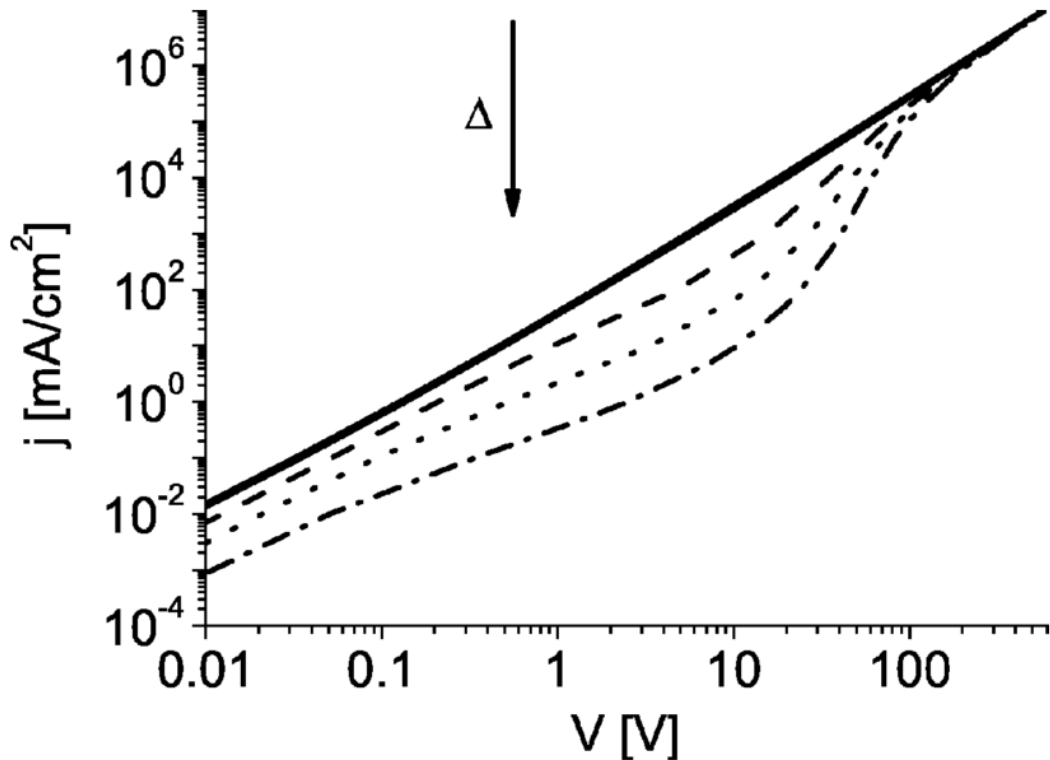

Figure 2.3: $j - V$ characteristics for barrier heights Δ of 0, 0.2, 0.3, 0.35, and 0.4 eV of the model presented in Ref. [12]. Adopted from Ref. [12].

Due to its drift-diffusion-like form of the equation for the field in the organic, the model of Neumann *et al.* enables to account for charge accumulation at the interface and to consider the resulting potential intrinsically. By this, it is possible to account observe a space-charge limited current. However, except for the total density of states, no disorder effects such as trapping are considered (1). Also no Coulomb-Coulomb- interactions in the bulk, apart from the resulting potential are modelled (2). Finally, the model does not yield a closed $j - V$ relation (3) but rather defines the voltages implicitly via the solution of desired values of j.

A simple KMC model of injection

In the work of Wolf *et al.* [1], KMC simulations are utilized for the first time to study the injection efficiency from a metal electrode into a disordered organic. The state energies of the sites were drawn from a Gaussian-shaped density of states of width σ. Instead of treating injection as a hopping event as in [2] and [3], charges are placed randomly in the first two layers of the bulk. The probability that one site of the bulk is chosen for injection, is determined by the formula $P_{ij} = \frac{\nu_{ij}}{\sum\limits_{j \neq i} \nu_{ij}}$, where ν_{ij} is the hopping rate of jumps from a site i in the metal into a possible site j in the bulk. The authors correct

for this direct placement of a charge in the bulk with a factor f, which is multiplied with the injection efficiency of the simulation. A detailed analysis of the method of this paper will be given in Chapter 5.

Injection is only allowed perpendicular to the metal into the first two layers of the bulk. Similarly, a jump back into the metal can only be perpendicular. A charge is regarded as having escaped after reaching the ninth layer of the bulk.

Apart from, (1), not treating the first injection hop as an event also, (2), Coulomb-Coulomb- interactions in the bulk and between the images of non-mutual charges are not considered. Only the Coulomb-attractions between particles and their own images, as described by Equation 2.1 are considered. Due to (2), also charge accumulation close to the interface and its influence on the barrier is neglected (3). Finally, the results of the work of Wolf *et al.* cannot be used to check against the model to be presented here, as an injection efficiency as in their simulation cannot be defined for the injection of interacting charges (cf. Chapter 4.4). Neither are current density simulations that would allow a direct comparison given.

Injection in an OPV simulation using KMC

Marsh *et al.* [2] present a KMC model for an OPV device. Within the organic, Coulomb-Coulomb-interactions between like particles are considered up to the Coulomb capture radius (cf. Equation 2.9). At the electrodes, the mechanism of thermionic injection is used to model dark injection. The authors understand thermionic injection as a hopping event from the electrodes into the organic. Therefore, the electrodes are discretized layers being one mesh cell wide, with the same edge length as the bulk sites. Hopping into the organic semiconductor is described with the same rate equation and the same parameters as in the bulk. All sites of the electrodes can inject into the organic material. In order to decrease computational effort, no Coulomb-Coulomb-interactions are considered for these initial steps. This is well justified, as only low charge carrier densities are expected. The authors mention, that their simple algorithm was checked against an algorithm, which correctly included Coulomb-Coulomb-interactions in the initial step, without any difference. By using this simple approach for injection, the computationally inexpensive first reaction method (FRM, cf. Chapter 3.5) can be used not only for hopping events in the bulk, but also for injection events. It needs to be mentioned, that, although Coulomb-Coulomb-interactions are not regarded for injection, the intrinsic energy ϵ_i of the bulk sites, drawn from a Gaussian DOS (described in Chapter 3.4), is included not only in the bulk hops, but already at initial injection steps.

Injection into a sandwiched organic using KMC

An advanced approach for KMC simulations, including injection was used by van der Holst *et al.* [3]. Here, KMC simulations of a disordered organic, sandwiched between two electrodes are carried out. Similar to Ref. [2] and Ref. [1], disorder is introduced, by using a Gaussian DOS. Similar to Ref. [2], a hop from the metal into the organic and vice versa is treated in the same way as a hop in the bulk. Additionally, all Coulomb-Coulomb-interactions between particles and images are considered already in the initial injection hop.

The methodology used in Ref. [3] is certainly including all Coulomb-Coulomb-interactions and consequential effects. However, it is not possible to deduce laws for pure injection, due to the presence of a second electrode, where image charges are mirrored infinitely and the extraction of charges at the second electrode might influence the current tremendously. A comparison to the results of this work will nonetheless be presented in Chapter

5, in order to check the validity of the presented code and investigate the differences between a single contact and a sandwiched setup. Also, it needs to be mentioned, that the choice of a 1.6 nm lattice constant might be too large to account for the effect of Coulomb-Coulomb-interactions correctly.

2.3 Aim of the thesis

As the discussion of macroscopic models has shown, those are not capable of including all expected effects. Ref. [9] is the first approach of regarding a recombination current back to the electrode, but neglects any microscopic effects, such as disorder, space charges or any Coulomb-Coulomb interactions between particles in the bulk. Ref. [11] on the other hand is the only macroscopic model that explicitly regards disorder. However, it lacks space charge effects and other Coulomb-Coulomb-interactions due to the injected particles. Ref. [12], on the other hand, contains space charge effects, but lacks a deeper consideration of disorder. Any Coulomb-Coulomb-interactions are only considered in terms of the electrostatic potential.

Therefore, a deeper (microscopic) insight into injection can only be achieved by microscopic models. As the review has shown, KMC gradually improved over the past years in describing injection. Ref. [1] contains already disorder, even though injection was not directly included into the methodology but rather by applying some trick and Coulomb-Coulomb-interactions were only considered between particles and their own images. In Ref. [2], only the initial injection hop neglects interactions with other particles, while hops within the organic material account for these interactions. This has been shown to be a reasonable assumption for OPV devices and average injection barriers of 0.4 eV. An approach including all effects described in the introductory chapter was done by Ref. [3]. However, it did not only focus on injection, but also charge extraction, due to the second electrode. Therefore, the $j - V$ relationship described in Ref. [3], are expected not to coincide with the ones for a simple metal-organic semiconductor setup.

It is, therefore, the aim of this thesis to develop a KMC model for describing injection from a metal electrode into a disordered organic semiconductor, which accounts for all effects described in the introduction, going beyond present approaches.

We expect our simulations to reach a SCLC, as described by Ref. [12] for high fields, as a result of an expected accumulation of space charges near the metal-organic semiconductor interface. Moreover, we also expect the current density to be disorder dependent, i.e., decreasing with disorder, which is not accounted for explicitly in Ref. [12]. Compared to Ref. [11], we expect an earlier saturation due to the SCLC regime, originating our considerations of the Coulomb-Coulomb-interactions between particles in the bulk. For low fields, the current is expected to follow an injection limited current, such as in Ref. [9].

3 Mesoscopic Modelling using Kinetic Monte Carlo

KMC is employed to study the time evolution of a system based on events. In the case of hopping transport, it is assumed, that particles hop from localized site i to site j within a material at a certain rate R_{ij} determined e.g., by their different site energies ϵ_i. This is shown schematically in Figure 3.1 for a one-dimensional system.
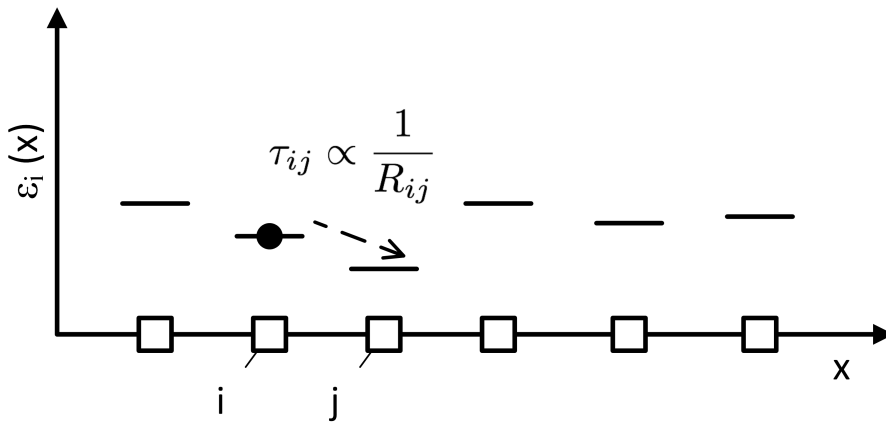

Figure 3.1: Schematic picture of the random site energies in a one-dimensional system. A hop from site i to site j occurs at a rate R_{ij} which can be related to a hopping time τ_{ij}.

Due to an exponential decay, the rate can be related to a waiting time τ_{ij} via a uniform distributed random number X according to Equation 3.1 [6] :

$$\tau_{ij} = -\frac{ln(X)}{R_{ij}} \tag{3.1}$$

The following sections provide the methodological and theoretical background of KMC simulations. First, the theoretical foundations of KMC are presented. Next, an overview of the ingredients of a KMC simulation as well as variations of particular simulation steps is given.

3.1 Theoretical foundations of KMC

A short overview of the Master equation and Poisson processes is given, before the three criteria for a Poisson process, a crucial prerequisite for KMC modeling, are summarized.

3.1.1 The Master equation and the Poisson process

The transport equation capable of describing the hopping of a localized site to another is the Master equation. In general, the Master equation (Equation 3.2 [4]) is known to "describe the time-evolution of a system that can be modelled as being in exactly one

of countable number of states at any given time, and where switching between states is treated probabilistically" [13].

$$\frac{\mathrm{d}P(\sigma,t)}{\mathrm{d}t} = \sum_{\sigma'} W(\sigma' \to \sigma)P(\sigma,t) - \sum_{\sigma'} W(\sigma \to \sigma')P(\sigma,t). \tag{3.2}$$

Here, $P(\sigma,t)$ is the probability of the system being in state σ at time t and $W(\sigma \to \sigma')$ is the transition probability at which the system goes from a state σ to a state σ'. Therefore, the time evolution $\frac{\partial P(\sigma,t)}{\partial t}$ of a particular state σ described in equation 3.2 can be interpreted as the rate of probability of all states going to state σ, minus that of state σ going to any other state of the system.

The Master equation has been formulated and solved for charge transport previously. [3] However, an alternative and intuitive approach to obtain the time evolution of charge transport is Kinetic Monte Carlo. The basic idea, as stated by Fichthorn and Weinberg is that the Master equation describes a Poisson process [4]. Hence, KMC can be used to solve the Master equation, if KMC describes a Poisson process.

A Poisson process obeys the stochastic differential equation (SDE) $dx = \alpha x dt + \beta x dN$ [14], where $\alpha x dt$ is the drift term and $\beta x dN$ the noise term. Here, dN can only take values 0 or 1 and β is a scaling factor. The probability for dN taking the value 1 or 0 is λdt or $1 - \lambda dt$, respectively [14]. Then, the probability density function of $N(t)$, which is the number of jumps within time t follows a Poisson distribution given by $P(n,t) = \frac{(\lambda t)^n e^{-\lambda t}}{n!}$, which is the probability for n jumps in time t. [14]

As an alternative to the SDE, the same problem can be stated in terms of a Master equation (Equation 3.3) [14] :

$$\frac{\mathrm{d}P(n,t)}{\mathrm{d}t} = \lambda \left(P(n-1,t) - P(n,t) \right), n > 0. \tag{3.3}$$

This formulation has the advantage of explicitly containing λ and thus, obliterates difficulties in solving the SDE with respect to time or positive x. The solution $P(n,t)$ is again the Poisson distribution.

3.1.2 Requirements on KMC for being a Poisson process

The theoretical background of KMC relevant for this work is described by Fichthorn and Weinberg [4]. The authors show that the master equation (cf. Equation 3.2) describes a Poisson process.

They further argue, that the following three criteria have to be met by a dynamical interpretation of Monte Carlo, as the authors call it, for being a Poisson process:

1. independence of events

2. transition probabilities satisfy

    a) detailed balance

    b) a dynamical hierarchy

3. time increments are formulated correctly

The first criterion is met for "sufficiently large systems" [4].
The second criterion for the transition probabilities consists of two requirements: (a) At equilibrium, detailed balance must be achieved. I.e., that transitions from state σ to σ'

happen at the same rate as from σ' to σ (cf. equation 3.4, which can be obtained by setting the time derivative in equation 3.2 to zero[4]):

$$W(\sigma' \to \sigma)P(\sigma', t) = W(\sigma \to \sigma')P(\sigma, t). \tag{3.4}$$

Furthermore, (b) away from equilibrium, a dynamical hierarchy has to be achieved, which is, to put it crudely, a transition probability based on a given rate expression W is smaller than unity. A mathematical description is shown in equation 3.5 [4], where $r(\sigma \to \sigma')$ is the rate from σ to σ' .

$$W(\sigma' \to \sigma) = \frac{r(\sigma \to \sigma')}{\xi_{max}}, \xi_{max} \geq sup\{r(\sigma \to \sigma')\} \tag{3.5}$$

The third criterion is met by drawing a time increment from an exponential distribution[4], such as Equation 3.1, if the corresponding event took place. Note that KMC is, thus, only valid on timescales, where only one event happens at a time[4].

3.2 Set-up of the KMC simulations

In the case of this thesis, the three-dimensional system is uniformly discretized into cubes of either $0.6\,nm$, $1\,nm$ or $1.6\,nm$ edge length (a_{latt}). The edge length of $0.6\,nm$ is used in [1] , whereas [2] is using $1\,nm$ and [15] is using $1.6\,nm$. A value of approximately $1\,nm$ is a trade-off between accuracy and the size of a system that can actually be simulated. In particular, an edge length sufficiently larger than $1\,nm$ would underestimate the Coulomb-Coulomb-interaction between close by particles. Additionally, the edge length is related to the size of the molecules of the material and is therefore material specific. In Figure 3.2, such a model system is shown in a two-dimensional representation, where the electrode is depicted in gold on the left.
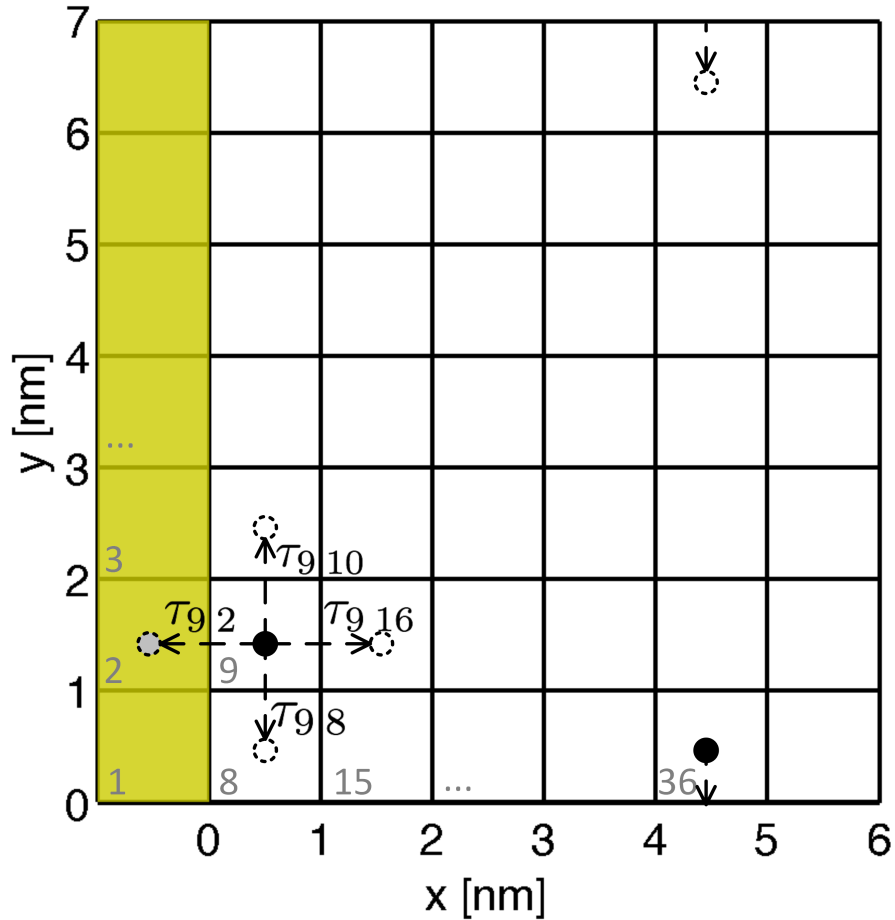

Figure 3.2: Schematic picture of the uniformly discretized model system, shown in two-dimensional representation for clarity. The electrode is depicted in gold on the left. The particle at site $i = 9$ may hop to one of the nearest neighbour sites (other sites are not shown for clarity), where each hop has a particular waiting time. The particle experiences a Coulomb-Coulomb-interaction with its own image charge, depicted in gray on site $i = 2$. A particle might hop to an adjacent site, if periodic boundary conditions apply, as shown for the particle at site $i = 36$.

All sites (voxels) are possible hopping sites, with a particular energy assigned (cf. Chapter 3.4). The waiting time τ_{ij} for a hop from a localized site i to site j is calculated from a rate equation R_{ij} (cf. Chapter 3.3) according to Equation 3.1. The rate depends

upon the energy difference between sites i and j, which contains the Coulomb-Coulomb-interaction with any particle and in presence of a metal interface their image charges (cf. Chapter 3.4). In Figure 3.2, the particle at site $i = 9$ experiences a Coulomb-Coulomb-interaction with its own image charge, depicted in gray on site $i = 2$.

If a metal contact is introduced perpendicular to the $x-$direction, periodic boundary conditions (PBC) in the $y-$ and$z-$directions apply. I.e., particles may experience Coulomb-Coulomb-interactions with periodic replica of other particles. Also, hopping out of the considered volume is possible. This is shown for the particle at site $i = 36$ in Figure 3.2, which hops to a voxel on the top, due to the superimposed PBC.

In order to perform a KMC simulation in a reasonable amount of time, a number of simplifications have been suggested by the literature (cf. Chapter 3.5). However, the most accurate way, to perform a KMC simulation would consist of the following steps:

---

1. Recalculate the waiting time for each particle to jump to any site using formula 3.1, considering the following energies:

   a) Coulomb-Coulomb-interaction with any particle and in presence of a metal interface their image charges, considering the periodic boundary conditions

   b) the intrinsic energy due to a given density of states (DOS)

   c) the energy due to an external electic field F_{ext}.

2. Choose the smallest waiting time and perform the corresponding hop.

3. Go back to step 1.

Figure 3.3: KMC steps for solving the Master equation.

3.3 Rate equations for charge carriers

As explained in the beginning of this chapter, the waiting time for a hop from site i to site j is calculated from a rate R_{ij} (cf. Equation 3.1). In literature, two rates are used to describe a transition as a function of the site energy difference ΔE_{ij} and the temperature T.

In Ref. [16], a hopping rate R_{ij}^M following Marcus theory (Equation 3.6) is derived from the Holstein model for large electron-vibrational coupling and high temperatures.

$$R_{ij}^M = \nu_0 \exp\left(-\frac{(\Delta E_{ij} + E_{reorg})^2}{4 E_{reorg} k_B T}\right) \tag{3.6}$$

In contrast to that theory, the Miller Abrahams equation (Equation 3.7) is valid for weak electron coupling and low temperatures[16].

$$R_{ij}^{M-A} = \nu_0 \exp\left(-2\gamma r_{ij}\right) \begin{cases} \exp\left(-\frac{\Delta E_{ij}}{k_B T}\right) & \Delta E_{ij} > 0 \\ 1 & \Delta E_{ij} < 0 \end{cases} \tag{3.7}$$

In the two equations, ν_0 is the attempt frequency and k_B Boltzmanns constant. ΔE_{ij} is the difference in site energy between sites i and j: $E_j - E_i$. This includes all energetic

influences such as the intrinsic energy and the coulombic interactions (cf. Chapter 3.4). In Equation 3.6, E_{reorg} is the reorganization energy (see below). In Equation 3.7, γ is an overlap factor accounting for the electronic interaction between the sites i and j. The exponential factor, related to γ, makes long distance hops less likely and is, thus, sometimes also introduced in Marcus Theory (cf. Chapter 3.5).

Compared to Miller - Abrahams, Marcus-type rates depend on the difference in site energies also for downward hops. The Marcus rate essentially describes the rate of electron transfer between two states. The basic idea of Marcus theory is sketched in Figure 3.4. Shown are the potential energies of the initial state i and the final state j as a function of the nuclear configuration coordinate Q; Q_i and Q_j denote the configurations at which the states adopt their minimum with the energy values E_i and E_j.
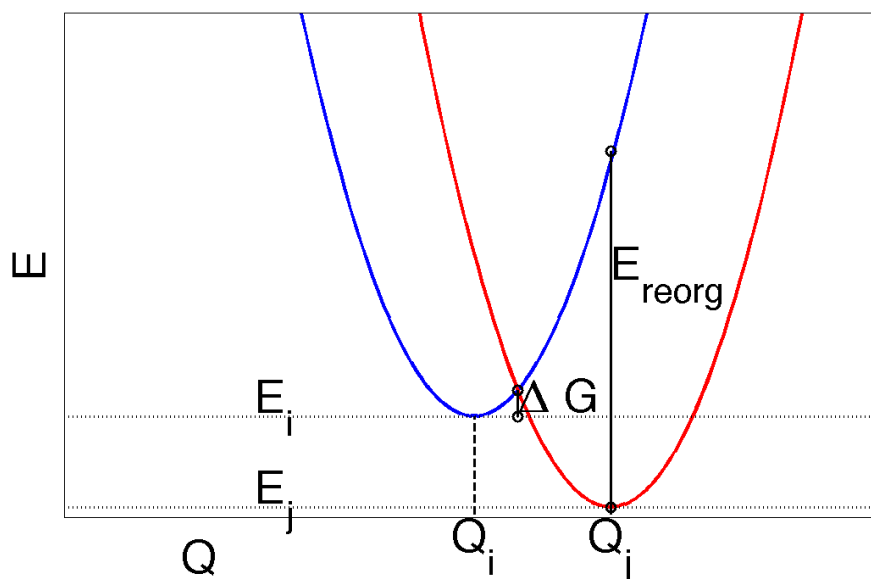

Figure 3.4: Schematic sketch of the energy levels before the electron transfer (blue) and after the electron transfer (red) as a function of a nuclear coordinate Q. In order to transfer the electron from state Q_i to Q_j of energies E_i and E_j a Gibbs free energy of activation ΔG is needed, which can be calculated according to the text, using the reorganization energy E_{reorg}

To transfer the electron from i to j, an activation energy ΔG has to be overcome. In the harmonic approximation, ΔG can be expressed using the difference in electronic energies $\Delta E_{ij} = E_j - E_i$ and the reorganisation energy E_{reorg}, i.e., the energy dissipated in going from Q_i to Q_j in the final state. Such a transition occurs activationless if $\Delta E_{ij} = E_{reorg}$. The larger the deviation between E_{reorg} and ΔE_{ij}, the less likely the electron transfer will be.[17]
Despite the fact that the Miller - Abrahams rate is derived for low temperatures and Marcus rate for high temperatures, they have both been used for simulations at around room temperature (cf. [1, 2, 15, 18]).

3.4 Energetic Landscape

The energetic difference between two sites with coordinates r_i and r_j, ΔE_{ij}, is given by Equation 3.8.

$$\Delta E_{ij} = \underbrace{\Delta \epsilon_{ij}(Eq.(3.9)) + \Delta E_{ext,ij}(Eq.(3.10)) + \Delta E_{coul,ij}^{bulk}(Eq.(3.11))}_{bulk}$$
$$+ \underbrace{\Delta E_{img,ij}(Eq.(3.13)) + \Delta E_{coul,ij}^{img}(Eq.(3.12))}_{metal} \tag{3.8}$$

Here, the energy following each Δ, represents the corresponding energetic difference between the two sites, followed its defining formula given in brackets. For example, $\Delta \epsilon_{ij}$ is the difference $\epsilon_j - \epsilon_i$, where $\epsilon_{i/j}$ is given by Equation 3.9. The first part of Equation 3.8 is the energy contribution of particles experiencing only bulk interactions, far away from any metal interface. The second part has to be considered, if a metal interface is present in order to satisfy a constant potential at the metal interface.

3.4.1 Bulk

In this work, the bulk simulation is restricted to one kind of particle being transported through one kind of material. Therefore, each voxel gets assigned one discrete transport level. In order to mimic the random disorder in organic materials, the density of states (DOS) is assumed to follow a Gaussian distribution. This is accomplished by drawing the intrinsic energy of each voxel, ϵ_i, from a Gaussian distribution of width σ, following Equation 3.9.[1, 2, 18] The center of the intrinsic energy level, $\bar{\epsilon}$, is set to zero, as only energy differences play a role in the rates.

$$g(\epsilon_i | \bar{\epsilon}, \sigma) = \frac{1}{\sigma \sqrt{2\pi} a_{latt}^3} \exp\left(-\frac{1}{2}\left(\frac{\epsilon_i - \bar{\epsilon}}{\sigma}\right)^2\right) \tag{3.9}$$

This procedure can be extended by adding additional transport levels for additional kinds of particles (e.g. HOMO and LUMO for holes and electrons). Additionally, the bulk might consist of a blend of different materials, each of which could have different properties such as σ and $\bar{\epsilon}$. Correspondignly, simulations with artificial blends (Ref. [2]) and blends derived from lower length scale predictions (Ref. [19]) or experiment (Ref. [20]), in particular aiming at organic bulk-heterojunction solar cells, have been reported.

External electric field An externally applied, homogeneous field F_{ext} results in an energy E_{ext} at a distance $r_{i\parallel}$ parallel to the field for an electron at site i of charge q_i,

$$E_{ext,i} = q_i F_{ext} r_{i\parallel}. \tag{3.10}$$

Coulomb Interactions Charges in the bulk experience Coulombic forces between each other. The related energy contribution to a particle i is given in Equation 3.11. Here, q_i and $q_{i'}$ are the charges of particles i and i' and ϵ is the permittivity of the bulk. The index i' runs over all N particles in the bulk.

$$E_{coul,i}^{bulk} = \sum_{i' \neq i}^{N} \frac{q_i q_{i'}}{4\pi \epsilon r_{ii'}} \tag{3.11}$$

3.4.2 Metal interface

In order to satisfy a constant potential at the metal surface at the metal bulk interface, image charges are introduced. These are mirrored along the metal interface and placed inside the metal with the same charge but opposite sign of their counterparts in the bulk.

Each particle i in the bulk experiences a coulombic energy, similar to Equation 3.11, of the images of all $N-1$ other particles i'. This contribution is given by Equation 3.12. The term $r_{ii'}^{img}$ is the distance between particle i and the image of particle i', which is mirrored along the metal interface.

The contribution of the image of particle i itself adds an energy $E_{img,i}$ (Equation 3.13), where $r_{i\parallel}$ is the distance between the particle and the metal contact[21]. The other variables are as previously defined.

$$E_{coul,i}^{img} = \sum_{i' \neq i}^{N} \frac{-q_i q_{i'}}{4\pi\epsilon r_{ii'}^{img}} \tag{3.12}$$

$$E_{img,i} = \frac{-q_i^2}{16\pi\epsilon r_{i\parallel}} \tag{3.13}$$

3.5 Update Algorithm

FRM vs. exact calculation   As mentioned in the introductory Chapter 3, the exact way of implementing KMC would require to recalculate all waiting times after an event (hop) had occured, which results in high computational effort. It can, however, be reduced dramatically by using the first reaction method (FRM), as introduced by Marsh *et al.* [2]. It is argued, that after a hop occurred, it will not change the energetic surrounding of the other particles too much for a low concentration of particles[2], which has also been tested by comparing the dynamic behaviour to that of an exact implementation[2]. Therefore, in FRM the *exact* calculation of *all* waiting times will only be done once as an initial step. After the particle with the lowest waiting time has hopped, time will be advanced by that waiting time, which is also done for all the previously calculated waiting times. Then, only for the hopped particle, a new waiting time is calculated from its new energy environment.

M. Krammer (personal communication, 2014) suggested to extend this method by recalculating also the waiting times of particles within a certain radius with little additional computational effort, but more exact results. It was therefore used for this work, as described in section 4.2.

Hopping range   Depending on whether long range, or only nearest neighbour hops are regarded in a simulation, Marcus rates (equation 3.6) may be adopted by a distance dependent factor $e^{-\alpha r_{ij}}$ which is referred as variable range hopping in [23], which is already part of the Miller-Abrahams rate (cf. Equation 3.7). Similarly to γ in Equation 3.7, α describes the spread of the wavefunction and r_{ij} the distance between sites i and j.

4 Methodology

The simulations were implemented in MATLAB. In order to be able to compare against the data of the reference papers (cf. Chapter 5), for each reference a tailored-made code was generated to accomodate specific details, i.e., the rate expression, voxel size, considerations of Coulomb-Coulomb-interactions, the use of boundary conditions, or determination of observables.

This chapter will first go into more detail explaining the update algorithm, which is the crucial part of the code. The waiting times in the update algorithm are calculated from a rate equation (cf. Equation 3.1) which furthermore depends on the energetic landscape (cf. Chapter 3.4).

Certain contributions to the site energy are not changing within a simulation run, such as the intrinsic energy levels ϵ_i. These will be referred to as static.

Furthermore, other parts change due to the Coulomb potential connected to the hopping particles, which will be referred to as dynamic. For comparing against non interacting cases, such as Ref. [2], the Coulomb-Coulomb-interaction is simply switched off, by setting the cut-off radius smaller than the voxel size a_{latt}.

In all cases, however, except for the comparison to the work of Wolf *et al.* [1], a site in the bulk may only be occupied by one carrier, known as the Pauli exclusion principle.

Furthermore, it can be chosen, whether a Miller - Abrahams or Marcus rate equation is used (cf. Chapter 3.3).

In order to be able to compare against Ref. [1], injection was initially implemented in a similar way as described in the corresponding paper (cf. Chapter 5.2), which made certain assumptions for hopping from the metal into the organic, in order to reduce the computational effort. However, due to today's computing power, it was decided to implement injection similar to the work of van der Holst *et al.* [3], which considers injection being a hopping event and, therefore, in a more consistent way.

4.1 Initialization

The initial condition depends on whether pure bulk or injection simulations are conducted.

4.1.1 Bulk

The particles are placed in the bulk at random positions and the position of each particle is saved in an array. In a second step, the Coulomb-Coulomb-interactions due to the particles are added to the dynamical array of energies (cf. Chapter 3.4). In a next step, all waiting times for all the particles are calculated. For each particle, only the shortest waiting time is saved in a list together with the particle index. Furthermore, the coordinates of the corresponding hopping event are stored in a list. The resulting list of waiting times is sorted by increasing waiting time and one event is processed after another according to its position in the queue.

4.1.2 Injection

The metal contact is implemented as an additional layer of lattice width a_{latt}, as suggested by Ref. [2] and [3]. In this model, injection can take place from the metal contact into bulk layers which lie within the hopping radius r_{hop}, usually the first two layers. In the course of the simulation, the particles hop into the initially unoccupied bulk. To do so, the waiting times for all perpendicular jumps from the metal into the organic are calculated. The smallest time is chosen for injection and the particle is injected to the corresponding site. Next, the Coulomb energy due to the injected particle and its image are added to the dynamical array of energies. Also, the waiting times within r_{hop} of the injected particle are calculated from which the shortest waiting time and the corresponding particle index and coordinates are saved, similar to the bulk case. Each voxel in the metal layer is assumed to be occupied for calculating injection and empty for a hop back into the metal (recombination).

A charge accumulation is expected close to the metal organic interface which is not negligible. Therefore, it is necessary to ensure that each injection event is chosen based on the current system-state at any time. To do so, the lowest waiting time of all injection sites is calculated every iteration as explained above and sorted into the list containing the waiting times of the particles in the bulk.

Restricting ourselves to perpendicular metal-organic jumps is reasonable, since the corresponding rates are higher than for non-perpendicular jumps due to the shorter distance and the large number of injecting sites and the high number of injection sites in the metal.

4.2 Update Algorithm

In order to be able to simulate sufficiently large systems, it was decided to use FRM as introduced in chapter 3.5. In order to increase the accuracy with few additional computational effort, a partial update of the waiting times was added to FRM, as explained by M. Krammer (personal communication, 2014) . Here, it was chosen to update the waiting times of all particles which are located within the hopping radius r_{hop} around the new position of the hopped particle.

A flow chart diagram of our FRM implementation for hopping in the bulk is shown in Figure 4.1. After each KMC step, marked with a box in Figure 4.1, the newly calculated events are sorted into the queue of waiting times.
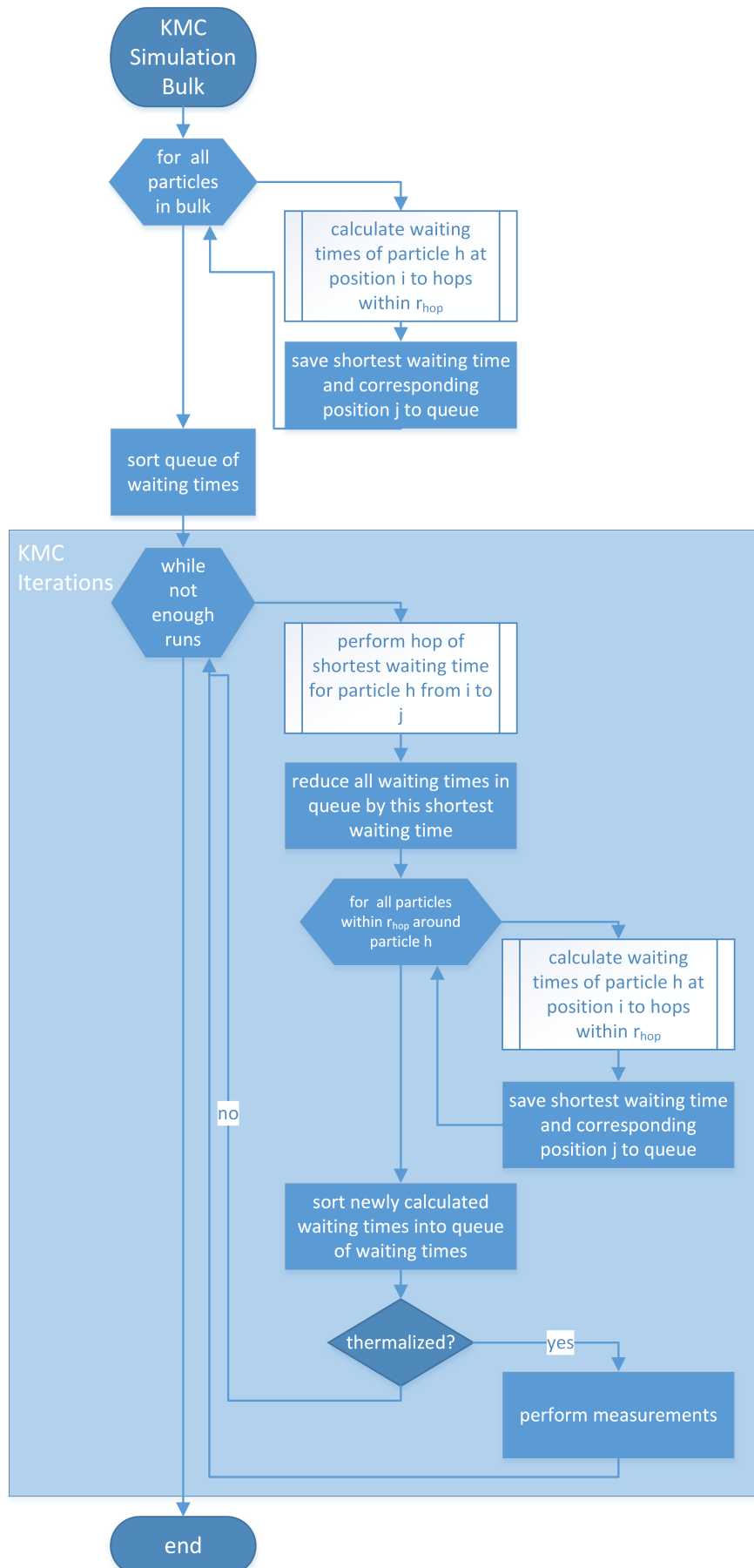
Figure 4.1: Flow Chart diagram of the implemented FRM algorithm for a bulk simulation

4.2.1 Selection of allowed hopping sites

Additionally, it can be chosen for the hopping range, to either allow hopping within a cube or a sphere of an adjustable size. Also, either simple bulk with periodic boundary conditions (PBC) or a metal-bulk interface can be simulated.

In the case of a pure bulk simulation, there are periodic boundary conditions in all directions. However, for the simulation of injection, those only apply in the y- and z-direction, but not perpendicular to the metal-surface. Also, for the case of a metalcontact, hops onto and from the metal surface are only allowed perpendicular to the position of the carrier (cf. Figure 4.2).
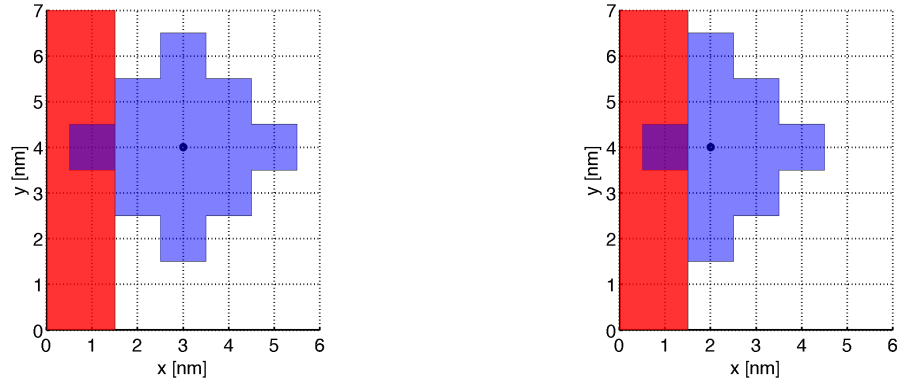
(a) allowed hopping sites for a particle located at $x = 3$ nm

(b) allowed hopping sites for a particle located at $x = 2$ nm

Figure 4.2: Allowed hopping sites for a charge (black circle) into the metal for different distances $\Delta x = x - x_{metal}$ from the metal (red) and $r_{hop} = 2$ nm. A site within the metal ($x_{metal} = 0$nm) can be target only if the associated hopping occurs perpendicular to the metal surface (in analogy to Ref. [1]).

To achieve an efficient selection of the allowed hopping sites, the following strategy was chosen:

1. Define the size of a cube, where the desired form (e.g. sphere) fits in (for example edge length 5, for a sphere of radius 2).

2. Use that size to create for each coordinate (x, y, z) a set of allowed nearest neighbours to hop onto, within that cube (e.g. for $x = 4$: $[2, 3, 4, 5, 6]$).

3. In order to have the desired form (e.g. sphere) for each x-position, an array of logical indices for the forms (cf. Figure 4.2) as well as a vector which includes the particular index of the logical array for the corresponding x-position is created. For example, the second element of that vector would link the logical array to the position indicated in Figure 4.2b.

4. When accessing the nearest neighbours of a particular site (x,y,z), the logical array with the index defined by the x-position is used to select the relevant energies from the cube.

4.2.2 Further update adjustments due to injection

For a simulation of injection, additions to the update method conceived for hopping in the bulk have to be made. The corresponding flow chart diagram is shown in Figure 4.3. In contrast to the bulk simulation, one has to discriminate between different types of sites and jumps in between them. Thus, four different cases for hops must be taken care of, especially for doing queueing correctly:

1. Particle injected: Add new entry to the queue and update waiting time for the entry;

2. Particle hops in bulk: Update waiting time for corresponding particle;

3. Particle recombined at the contact: Remove entry of corresponding particle from the queue;

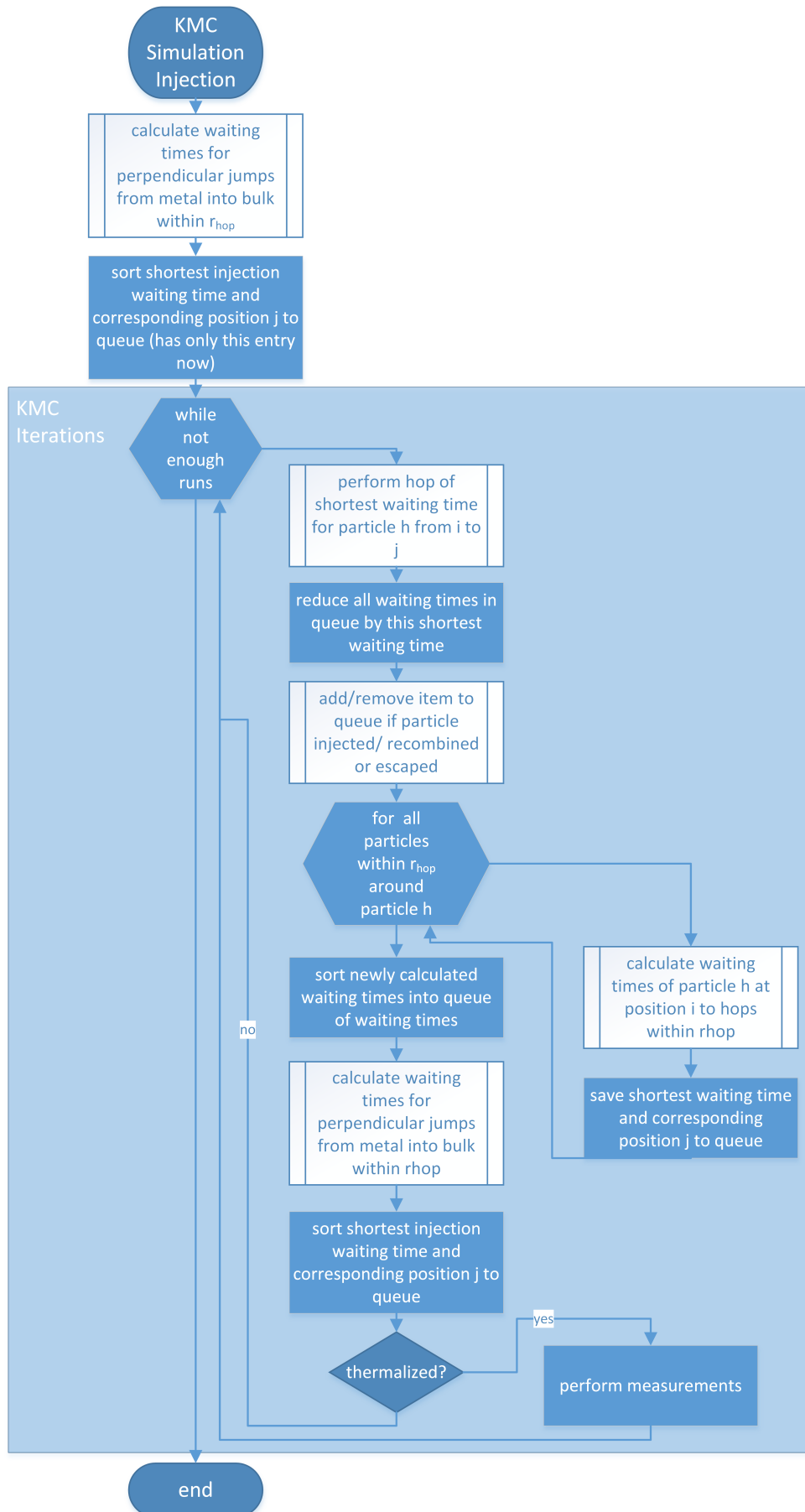4. Particle escaped: Remove entry of corresponding particle from the queue.

Figure 4.3: Flow Chart diagram of the implemented FRM algorithm for the simulation of injection.

4.3 Site energies

Contributions to the site energy are stored in two different arrays of equal size. The first array, E_{stat}, contains energy that is not changing within a simulation. The other array, E_{dyn}, contains the Coulomb part, which is changing due to the motion of the particles.

4.3.1 Static within a run

Each site of the bulk has an intrinsic energy assigned, which is drawn from a Gaussian distribution (cf. Chapter 3.4.1) with a mean energy of zero. The energy due to an external applied field is added to the sites as well, as it will not change during a run. A metal interface is considered by introducing one additional layer with the intrinsic energy ϵ_i set to Δ, which is the difference between the center of the Gaussian and the Fermi level. Additionally all sites in the bulk will have an energy due to their image charge added (cf. Chapter 3.4.2).

Figure 4.4 shows exemplarily how E_{stat} could look like, when a metal surface is present at $x = 0$.
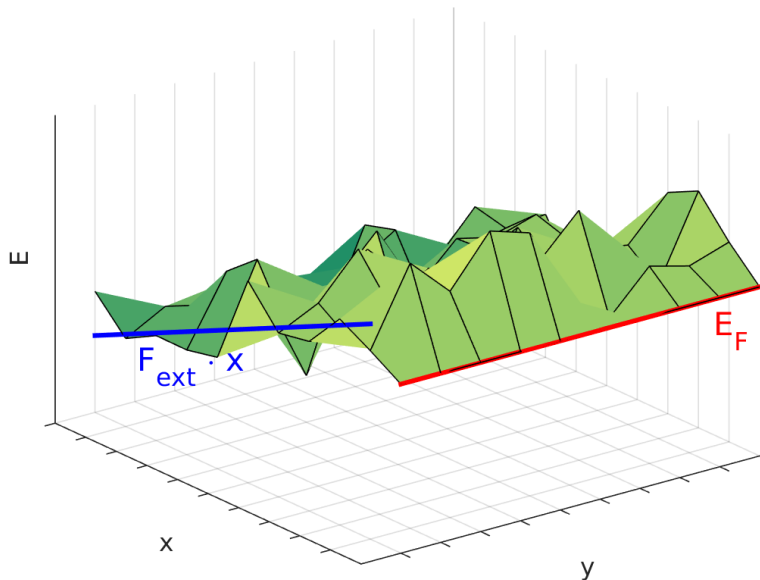

Figure 4.4: Example for the static energy part with a metal interface for one value of the z-coordinate. The position of the Fermi-level E_F is marked with a red line. The potential energy due to F_{ext} is marked with a blue line.

4.3.2 Dynamic within a run

This chapter explains how the energy contribution due to the Coulomb-Coulomb-interactions between moving particles is treated. It should be mentioned here, that each time a hopping rate is calculated for a particular particle, its own contribution (and that of its image) of the dynamical energy array to the energy difference ΔE_{ij} has to be subtracted for a correct calculation.

Due to the metal contact, the array containing the Coulomb energy of a specific particle and its image changes depends on the particles position in x-direction. The different

energy-arrays are calculated before the simulation starts. The selection of the corresponding arrays is accomplished in the same way as described in Chapter 4.2.1 for the allowed hopping sites.

Coulomb-Coulomb-interactions between particles in the bulk   One dynamical ingredient is the Coulomb-Coulomb-interaction between charges of the same polarity. Whenever a particle hops, its surrounding monopole potential (cf. Equation 3.11) is hopping as well, leading to the subtraction of its potential around the previously occupied site and the addition of it around the site it hopped onto. This results in an effective dipole potential (cf. Figure 4.6) whose contribution is truncated beyond a certain cut-off radius (see below) and saved to the array E_{dyn}. In order to avoid a sudden jump in energy due to the truncation at r_c, the energy at the cut-off radius is subtracted from the values of all affected sites in E_{dyn}.

The cut-off radius is by default chosen to be the thermal capture radius, defined by Equation 2.9. This choice of the cut-off radius was suggested by Marsh *et al.* [2]. However, when simulating injection at low fields and low barriers Δ, the device dimensions as well as the cut-off radius have to be adjusted carefully, as discussed in Chapter 4.5.2. As it will be discussed below, charge accumulation in the first layer can lead to a sudden jump in energy at the position $x = r_c$, which results in a spurious charge accumulation at that point. This is handled by increasing the cut-off diameter to the width of the device and decreasing the device length to the cut-off radius.
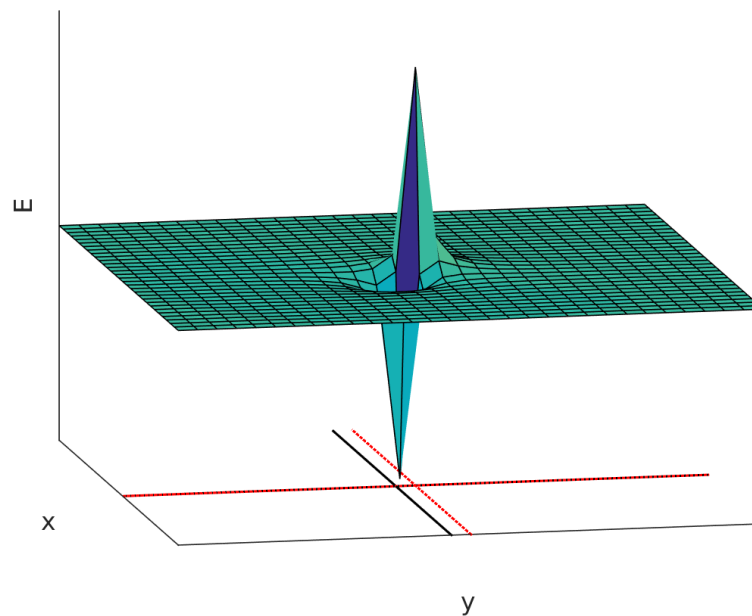

Figure 4.5: Update of the dynamical energy array due to a moving charge carrier that adopts the form of an effective dipole potential. In this example, the particle is hopping from the position marked with a black cross-hair to the one marked with a red dotted cross-hair.

Coulomb-Coulomb-interactions due to other images   For simulating injection, the Coulomb-Coulomb-interactions due to the images induced by the particles located in

the bulk (cf. Equation 3.12) have to be considered. To be consistent, their contributions are also considered up to r_c. For reducing the computational effort, these contributions are joined with the contributions from the Coulomb-Coulomb-interactions between particles in the bulk (see above) before the simulation starts (i.e., before the box "KMC Simulation Injection" in Figure 4.3).
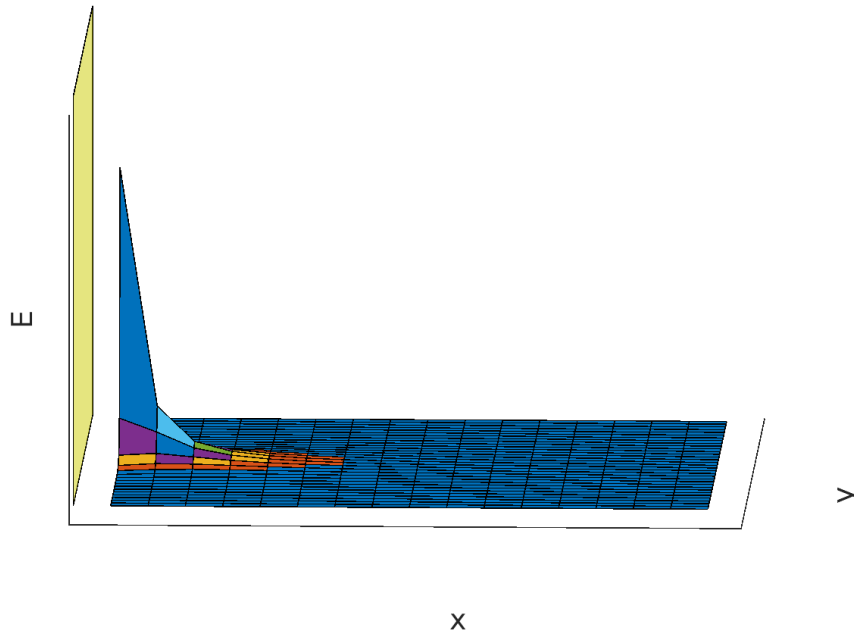

Figure 4.6: Example for the contribution of the image charge of an electron to the dynamical energy array for one value of z ($z = 0$). The position of the electrode is marked by a gold surface.

4.4 Observables

Mobility   In bulk simulations the mobility μ is usually an observable of interest. It is defined as the average drift velocity of the charges, v_d, at a given electric field F_{ext}: [**p.224**, 8]

$$
\begin{aligned}
\mu &= \frac{v_d}{F_{ext}} \\
&= \frac{\Delta l_{\parallel}}{N \cdot F_{ext} \cdot \tau_{sim}}.
\end{aligned}
\tag{4.1}
$$

It is measured by calculating the ensemble average according to the lower right-hand-side of Equation 4.1. Here, $\Delta l_{\parallel}$ is the total distance travelled by all particles, parallel to F_{ext}, N the number of particles, and τ_{sim} the simulation time. The latter is calculated by $\tau_{sim} = \sum_i \tau_i$, i.e., the sum of all waiting times τ_i of the hopping events that occurred.

Injection Efficiency   The injection efficiency ϕ_{inj}, introduced in Ref. [1] for injection experiments, is calculated as follows

$$
\phi_{inj} = \frac{n_{esc}}{n_{inj}},
\tag{4.2}
$$

where n_{esc} is the number of escaped particles and n_{inj} the number of injected particles. The number of escaped and recombined particles is handled according to section 4.2.2. In the absence of Coulomb-Coulomb-interactions, the injection efficiency is a well defined observable. In Ref. [1], a certain number of particles is initially placed in the bulk and then the experiment runs until all particles left the bulk. As the charges do not interact in this case, a charge will behave in the same way, whether there are ten or thousand particles in the bulk. However, upon including the Pauli exclusion principle, the environment is different in the beginning, where fewer voxels are available then later in the experiment, where a number of charges has already left the bulk. The situation is even more complicated upon including Coulomb-Coulomb-interactions, as the number of particles present in the bulk changes not only the number of available hopping sites but also the energetic landscape. Also, measuring ϕ_{inj} in steady state is problematic, since fast charges would be overrepresented, when trying to compare to a measurement of non-interacting charges with initially placed charges. Therefore, for injection simulations of interacting particles, it was decided to look into the current density j.

Current Density   In addition to the previous justification, the current density offers the possibility to easily compare results against reference papers (cf. Chapter 2.3), where the current density is usually given as a function of the external field or applied voltage. The current density j is defined as the current I per cross-sectional area.[**p.223**, 8] For the case of only one type of charge carrier of charge q present, this may by rewritten into Equation 4.3 to be used for KMC simulations:

$$
\begin{aligned}
j &= \frac{I}{A} \\
&= \frac{q \cdot n_{esc}}{A \cdot \tau_{sim}}.
\end{aligned}
\tag{4.3}
$$

Another formulation for the case of one carrier-type is

$$
j = n \cdot q \cdot v_d,
\tag{4.4}
$$

where n is the carrier density.[**p.224**, 8] The right hand side of Equation 4.4 can be rewritten in terms of the total displacement $\Delta l_{\parallel}$ and the simulation duration τ_{sim}:

$$j = \frac{q \cdot \Delta l_{\parallel}}{Vol \cdot \tau_{sim}}. \tag{4.5}$$

Here, Vol is the active volume of the bulk (i.e., the active length is $(r_{hop} - a_{latt})$ shorter).

We convinced ourselves that the two methods (Equation 4.3 and Equation 4.5) converge to the same result after sufficiently long simulation times. However, Equation 4.4 converges faster due to being an average with respect to the whole volume rather than the vicinity of the exiting plane. Therefore, we used that method for our calculations.

Electrostatic Potential   In the case of a metal-organic interface, the plane-averaged electrostatic potential $\Phi(x)$ offers the possibility to quantify the average contribution of accumulated charges to the energy landscape. In this way, also the voltage drop over the modelled system can be easily calculated as the difference in potential between the interface and the end of the device.

In order to determine the electrostatic potential $\Phi(x)$, the one-dimensional Poisson equation (Equation 4.6) needs to be solved:

$$\frac{\mathrm{d}^2\Phi(x)}{\mathrm{d}x^2} = -\frac{\rho(x)}{\epsilon_r \epsilon_0}. \tag{4.6}$$

Here, $\rho(x)$ is the charge-density, which is calculated from the charge-carrier density $n(x)$ as $\rho(x) = qn(x)$, where the charge $q = -e$ in the case of electrons being the charge-carriers.

In this work, we solve for a numerical value of $\Phi(x)$ in the following way: First, the plane-averaged charge-carrier density $n(x)$ is determined in a simulation (cf. Chapter 4.4.1). Second, from $n(x)$ and the above relation for $\rho(x)$, the right hand side of Equation 4.6 is approximated by a spline and integrated twice. The two boundary conditions are (1) a constant potential at the interface $\Phi(x = 0) = 0V$ and (2) the field at the bulk side being the applied field via $-\frac{\mathrm{d}\Phi(x)}{\mathrm{d}x}\big|_{x=L} = F_{ext}$, where L is the length of the device. The first boundary condition is simply met by setting $n(x = 0) = 0$. The second boundary condition is simply included in the first integration step as an integration constant at $x = L$.
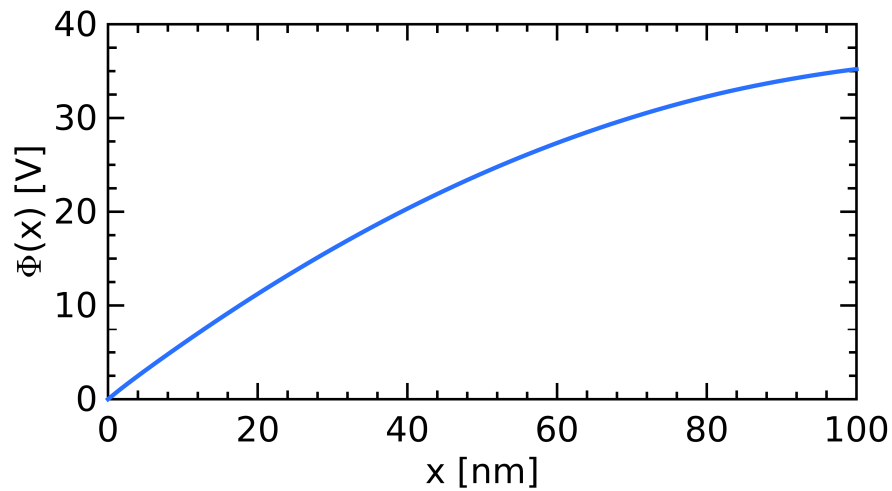
The process from calculating a spline from the charge carrier density $n(x)$ (Figure 4.7a) to the integration to calculate the field $F(x)$ (Figure 4.7b), and finally the electrostatic potential $\Phi(x)$ (Figure 4.7c) is illustrated in Figure 4.7. The corresponding simulation data was acquired for a benchmark calculation referring to Ref. [3] (see figure caption for details).
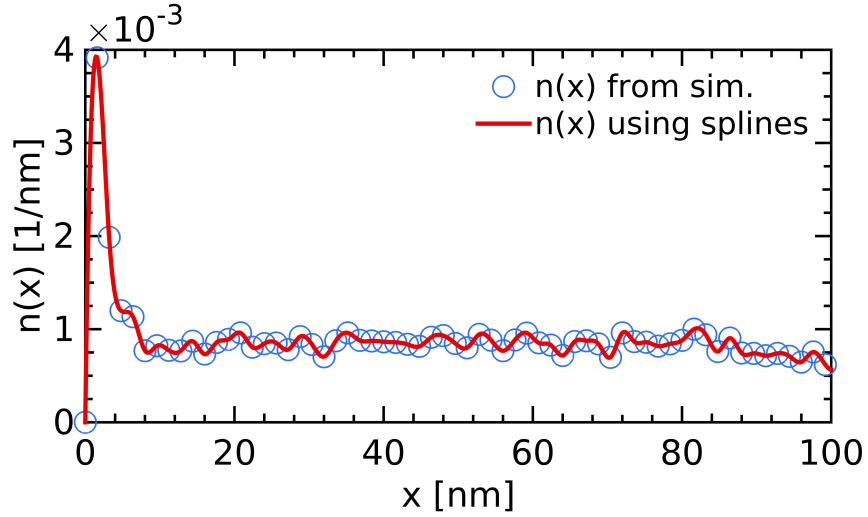
(a) The charge carrier density $n(x)$ from the simulation (blue circles) is approximated by splines (solid red line).
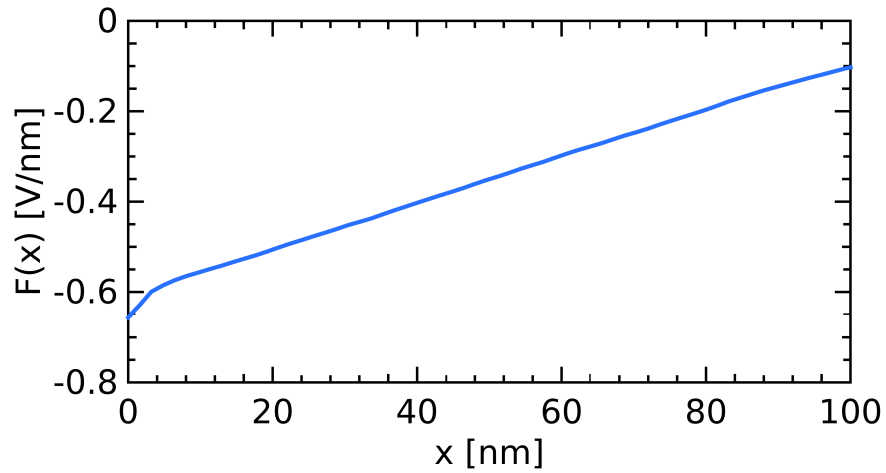
(b) The spline from Figure 4.7a) can be integrated to calculate the field $F(x)$ considering the boundary condition $F(x)\big|_{x=L} = F_{ext}$.

(c) Another integration step of the spline from Figure 4.7b yields the potential $\Phi(x)$.

Figure 4.7: Using splines, the charge carrier density $n(x)$ (Figure 4.7a) is integrated once to calculate the field $F(x)$ (Figure 4.7b) and by another integration step the electrostatic potential $\Phi(x)$ (Figure 4.7c). The data was taken from a benchmark experiment related to Ref. [3], where the length of the device is 102 nm, the disorder $\sigma = 75$ meV, $\Delta = 1$ eV and $F_{ext} = 1 \times 10^{-1}$ V nm^{-1}.

4.4.1 Convergence of observables

The following paragraph explains, how the code recognizes automatically that the system is in a state such that a measurement can be started. The time it takes the system to evolve from an initial state to a converged state is called the thermalization time. For all measurements the lower limit for a measurement is set to 1×10^6 iteration steps and the upper limit (including thermalization) to 12×10^6 steps.

Bulk   For bulk measurements, an ensemble is considered to have reached steady-state, if two subsequent mobility measurements (cf. Equation 4.1), averaged over a certain number of runs each, do not vary more than a threshold of 1%. The number of runs required determining the average is set to the number of particles present in the bulk. The criterion is indicated in Equation 4.7, where r_{th} is the threshold and $\overline{\mu}_i$ and $\overline{\mu}_{i-1}$ are the last and the next-to-last averages of the mobility:

$$\left| \frac{\overline{\mu}_i - \overline{\mu}_{i-1}}{\overline{\mu}_{i-1}} \right| \leqslant r_{th}. \tag{4.7}$$

Meeting the criterion three times, which is an empirical value for having a high certainty, indicates, that the Coulomb-Coulomb-interaction between the particles has averaged out and the ensemble is in a good initial position for measurements.

A rule of thumb, as given in Ref. [24], suggests a measurement duration of at least ten times the thermalization time (i.e., the time it takes to converge as described above) for reasonable measurements. Therefore, this value was chosen for the maximum number of runs after which the measurement is stopped. In Figure 4.8 this is illustrated for the simulations used to compare against [18] (cf. Chapter 5.3). The carrier density n is 5×10^{-2} in both figures. The disorder σ is 50 meV in Figure 4.8a and 150 meV in Figure 4.8b. It can be seen that for the high disorder it takes much longer to converge, but in both cases the algorithm detects the thermalized state reliably (red circles in Figure 4.8).
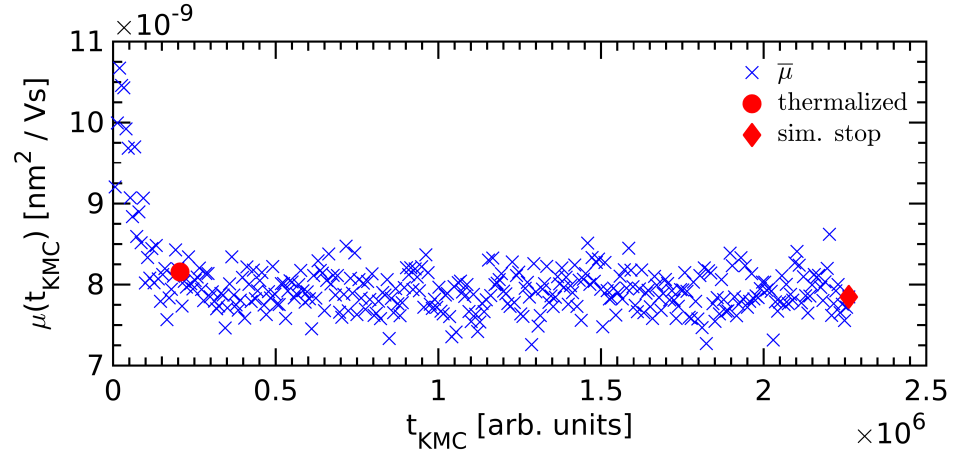
(a) Time evolution of the mobility averaged over the number of particles in the bulk $\overline{\mu}$ (blue) as a function of iterations (t_{KMC}) for a disorder of $\sigma = 50$ meV. The start of the measurement is marked with a red circle, the end with a red diamond.
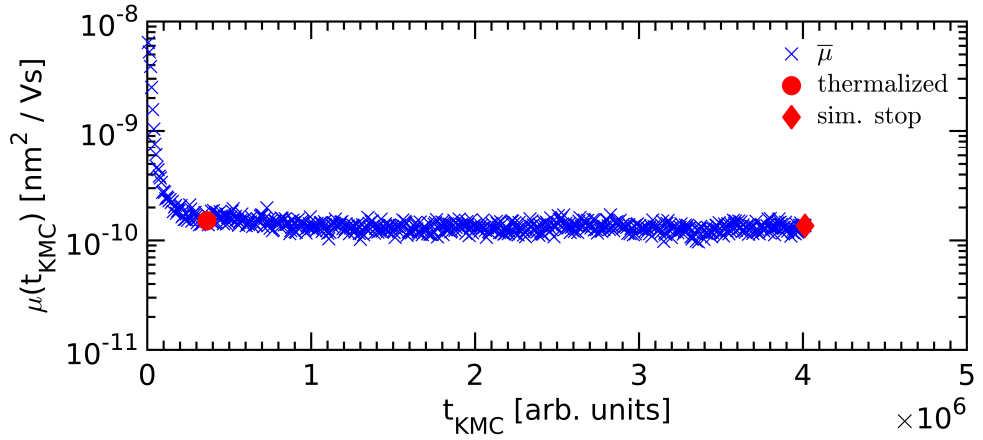
(b) Time evolution of the mobility averaged over the number of particles in the bulk $\overline{\mu}$ (blue) as a function of iterations (t_{KMC}) for a disorder of $\sigma = 150$ meV. The start of the measurement is marked with a red circle, the end with a red diamond.

Figure 4.8: Time evolution of the mobility averaged over the number of particles in the bulk $\overline{\mu}$ (blue) as a function of iterations (t_{KMC}) for different degrees of disorder σ. The carrier density is n is 5×10^{-2}. The simulation parameters are taken from Table 5.3.

Injection   An investigation of the benchmark measurements referring to Ref. [3] (to be described in Chapter 5.4) has shown that two different behaviours occur when looking at the time evolution of the number of particles inside the bulk. The first case is shown exemplary in Figure 4.9. Here, the number of particles is increasing exponentially until reaching a constant value. It can be simply explained by the bulk getting filled and equilibrium being a constant number of particles travelling from the metal into the bulk. The second case is shown in Figure 4.10. Here, the barrier is so high, that there is only a small number of particles present in the bulk. This number might be fluctuating, but never shows the behaviour seen in the former case. Due to the low number of particles (order of 10), already the first Kinetic Monte Carlo step is in equilibrium, as the particles are not supposed to interact at that low carrier densities.

In the first case, convergence is clearly an equilibrium between particles being injected from the metal and particles being absorbed in the bulk or recombined at the contact, where the total number of particles in the bulk remains constant. Therefore, the criterion for equilibrium is a fluctuation of the injected particles of less than 0.001%, averaged over 500 runs, which is calculated similarly to Equation 4.7. In contrast to the mobility criterion, this has to happen only once. The total simulation time is again set to ten times the thermalization time.

As mentioned before, the second case can be viewed as converged already from the first hop. This low density case is detected in the code, if the number of particles in the bulk, is lower than ten on average. The measurement will then start already at the beginning and will stop after the first particle has escaped at the end of the device.

The measurement of the charge-carrier density $n(x)$, which is needed to determine the electrostatic potential $\Phi(x)$, is started when the number of particles has converged as described above. Every 1000 runs the carrier distribution in the bulk is stored to an array. After the simulation has finished, that array is layer-averaged and also averaged over the number of carrier-measurements taken. This yields an effective charge-carrier density, $n(x)$, which can be used to determine the charge-density and by two integrations the electrostatic potential as described above.
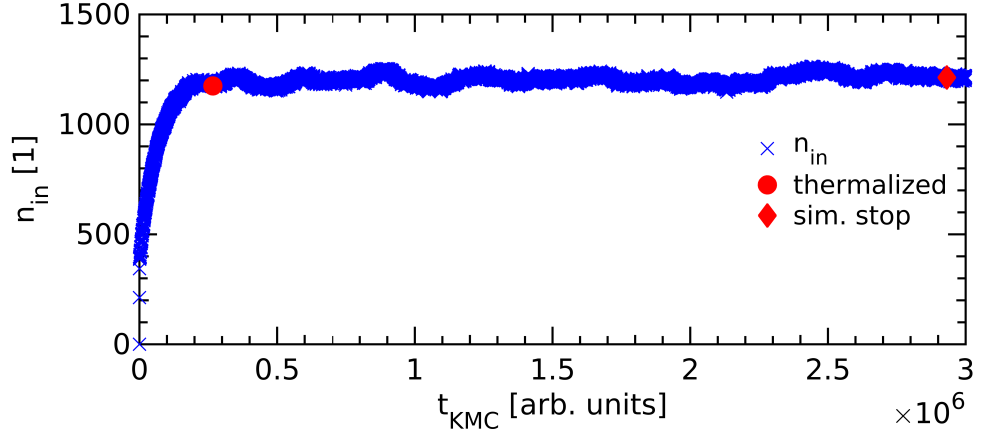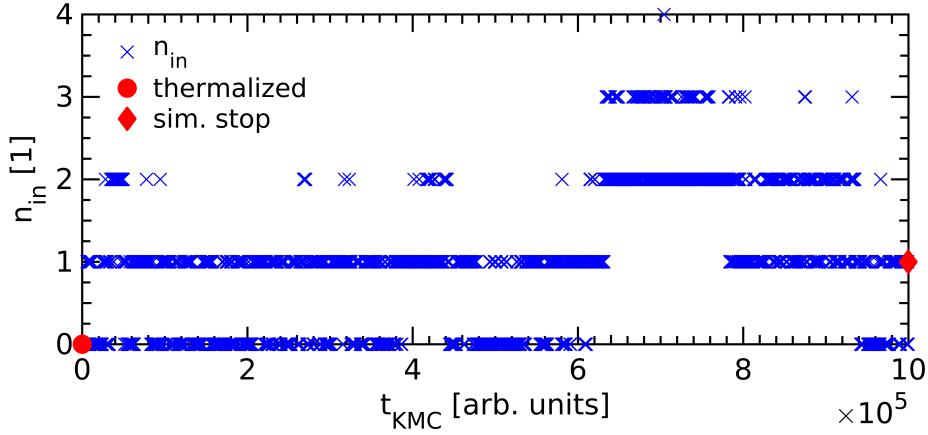
(a) Time evolution of the particle number n_{in} in the bulk (blue) as a function of iterations (t_{KMC}), the start of the measurement is marked with a red circle, the end with a red diamond
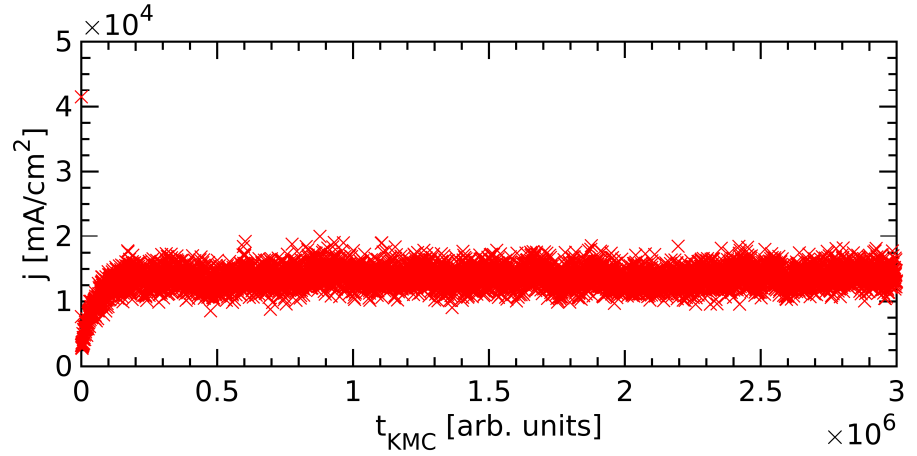
(b) Time evolution of the current density j (red) as a function of iterations (t_{KMC})

Figure 4.9: Time evolution of (a) the particle number n in the bulk and (b) the current density j for a length of 102 nm at $\sigma = 75$ meV, $\Delta = 0$ eV, $F_{ext} = 1 \times 10^6$ V cm^{-1}. Figure 4.9b shows, that the current remains constant in a certain range at the same point where the number of particle converges (cf. Figure 4.9a)

(a) Time evolution of the particle number n_{in} in the bulk (blue) as a function of iterations (t_{KMC}), the start of the measurement is marked with a red circle, the end with a red diamond
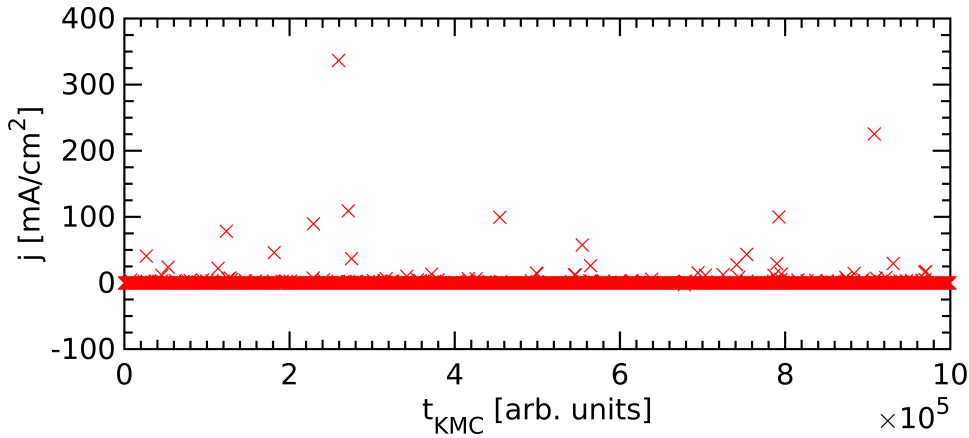

(b) Time evolution of the current density j (red) as a function of iterations (t_{KMC})

Figure 4.10: Time evolution of (a) the particle number n in the bulk and (b) the current density j for a length of 102 nm at $\sigma = 150$ meV, $\Delta = 1$ eV, $F_{ext} = 1 \times 10^6$ V cm^{-1}. Figure 4.10a shows, that the number of particles is so low, that the current remains constant in a certain band right from the beginning (cf. Figure 4.10b)

4.4.2 Error Analysis

When averaging over different morphologies (i.e. energetic landscapes), the sample variance s^2 associated with an observable y is calculated following Equation 4.8, where y_i is the i-th measurement of y and $\overline{y}$ the arithmetic mean, being determined by Equation 4.9.

$$s^2 = \frac{1}{n-1} \sum_{i=1}^{n} (y_i - \overline{y})^2 \tag{4.8}$$

$$\overline{y} = \frac{1}{n} \sum_{i=1}^{n} y_i \tag{4.9}$$

We calculate the sample variance for calculating the uncertainty of the current density j, the mobility μ, and the layer averaged Coulomb-Coulomb $n(x)$.

4.5 Experimental Design

In this chapter, the choice of parameters for the injection experiments of Chapter 6 is explained. First, an overview to the parameters is given, then a detailed discussion of the cut-off radius follows, which is crucial in order not to run into simulation artefacts. Figure 4.11 shows a sketch of the model system. Charges are injected from the metal surface (gold surface) and may hop into the bulk (positive x-direction). An external electric field (F_{ext}) in x-direction is applied.

4.5.1 Selection of reasonable parameters

In Table 4.1 an overview of the parameters used in this work is given.

Table 4.1: Parameters used for the investigations in Chapter 6

$rate$	$Miller - Abrahams$
$size$	$101 (or\, 25) \times 51 \times 51$
a_{latt}	1.0 nm
ϵ	3.5
T	$300K$
ν_0	$1\ s^{-1}$
γ	$10/a_{latt}$
σ	$varied$
Δ	$varied$
F_{ext}	$varied$

We use the Miller - Abrahams-rate for two reasons. Firstly, all reference papers that include injection, rely on Miller - Abrahams-rate except for Ref. [2], where Marcus-rates are employed. Secondly, according to Kimber *et al.* "Marcus rate is not applicable to the process of charge injection from electrode sites into the bulk" [25]. As discussed in Chapter 3.3, in Marcus-theory, the rate depends upon a reorganization energy E_{reorg}. In contrast to the organic material, no reorganization takes place in the metal and the
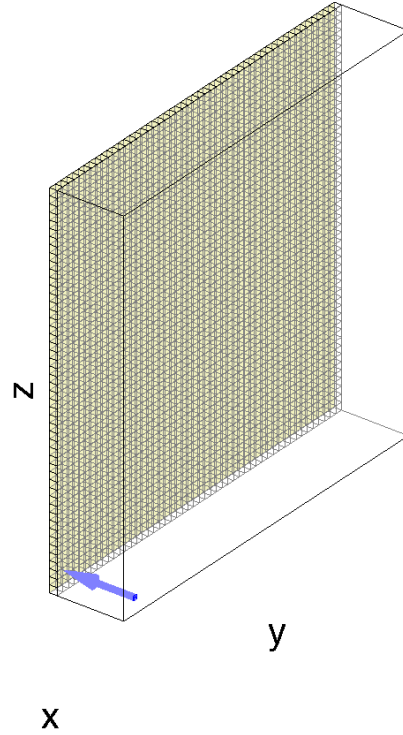
Figure 4.11: Sketch of the system simulated in this thesis. Charges are injected from the metal surface (at x = 0, gold surface). The first layer in the bulk with possible hopping sites is drawn after the metal surface. An external electric field (F_{ext}) in x-direction is applied, which is shown a blue arrow. The mesh within the semiconductor is suppressed for clarity.

meaning of E_{reorg} breaks down for the metal-organic contact.

The cross sectional area is chosen large enough to avoid finite size effects. According to Zhou *et al.* [18], an area of 51×51 nm is sufficient.

The length of the device in the direction parallel to the field must be chosen such, that it is longer than the point where a particle would have a non-vanishing probability of hopping back to the contact and recombine. By this, one is able to measure a representative net current. In Ref. [1], a length of 6 nm was chosen. We believe, however, that this is too short for the case of low fields and low barriers. A length of 101 nm, as we chose it, appears to be more than sufficient to achieve this. In order to justify that, the critical cases have to be identified.

These are, where (1) no charges accumulate in the layer after the contact (high barriers), such that particles in the bulk do not experience a repulsive force from accumulated charges or (2) the fields are too low to efficiently carry particles away from their images. In both cases, we can estimate an upper limit for the distance that is needed, to efficiently separate a charge from its image. This is done by applying the picture of a single, non-interacting charge, where no charge accumulation is present. For the case of a vanishing external field, according to Ref. [9], this distance is given by the Coulomb cut-off radius (cf. Equation 2.9), which is 15.9 nm for the given parameters and, therefore, much lower than the length of the bulk. As a second check, we might assume a particle as having escaped from its image, upon hopping further than the position of the maximum of the

barrier shape, as it is done in Ref. [9]. The position of the maximum is given by

$$x_{max} = \sqrt{\frac{e}{16 \cdot \pi \cdot \epsilon_r \cdot \epsilon_0 \cdot F_{ext}}}. \; [\textbf{p. } \textbf{250}, 8]$$

For the lowest field and the given parameters, it yields a distance of 10.14 nm, which is also lower than the length of the set-up. As described in Chapter 4.5.2, the bulk length is decreased to 25 nm for low barriers and low fields, which is still longer than the two upper limits above.

The choice of the edge length of 1 nm corresponds to the typical size of molecule and is supposed to be a value where Coulomb-Coulomb-interactions are neither under- nor overestimated.

The value of relative permittivity is also a common value for organic materials.

Similarly, an experiment at room temperature is a reasonable assumption. It is also used in Ref. [3] and [1].

The attempt frequency ν_0 was set to unity. As the current density j and the mobility μ scale linearly with ν_0, we can depict these observables in terms of ν_0, with the advantage of more generality. I.e., the current density j in Chapter 6 corresponds to j/ν_0.

A value of γ being $10/a_{latt}$ is commonly used in literature, where Miller - Abrahams rates are usede.g., in Ref. [3] and [1].

4.5.2 Investigation of the influence of the cut-off radius

An investigation of the layer-averaged charge carrier density $n(x)$ for the parameters of Table 4.1 has shown, that the choice of the cut-off radius for including Coulomb-Coulomb- interactions (cf. Chapter 4.3.2) can lead to artefacts. In Figure 4.12 the charge carrier density $n(x)$ is plotted for the case of no disorder for different barriers and fields.

As can be seen for the 0.4 eV barrier (Figure 4.12c) and low fields of 1×10^{-3} (blue) and 1×10^{-2} V nm^{-1} (red), the charge-carrier density is highest in the first few monolayers and slowly decays towards the extracting contact at 101 nm.

For the low barriers of 0.1 (Figure 4.12a) and 0.2 eV (Figure 4.12b) and low fields of 1×10^{-3} (blue) and 1×10^{-2} V nm^{-1} (red), however, a second accumulation zone, at around 16 nm away from the contact is formed that is preceded by a pronounced minimum. In the vicinity of the extracting contact, there is a steep, field-dependent decay.
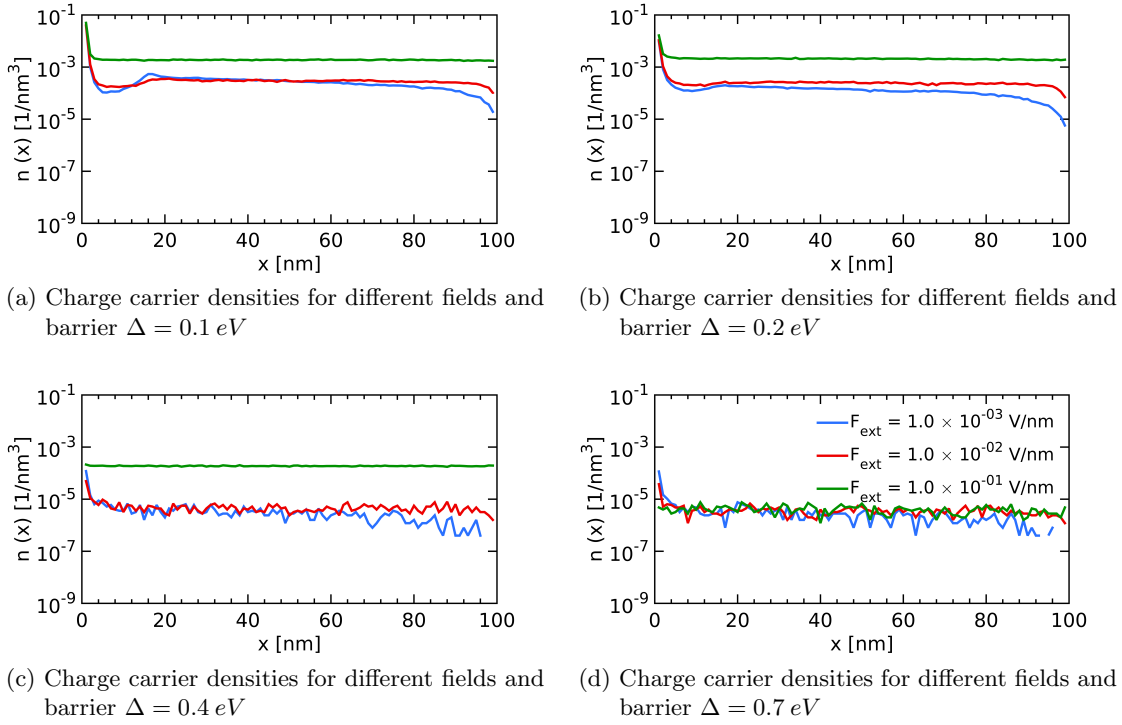
(a) Charge carrier densities for different fields and barrier $\Delta = 0.1\,eV$

(b) Charge carrier densities for different fields and barrier $\Delta = 0.2\,eV$

(c) Charge carrier densities for different fields and barrier $\Delta = 0.4\,eV$

(d) Charge carrier densities for different fields and barrier $\Delta = 0.7\,eV$

Figure 4.12: Charge carrier density $n(x)$ for the case of no disorder ($\sigma = 0k_BT$) and various fields F_{ext} and barriers Δ as a function of the distance from the electrode x, when using the Coulomb cut-off radius for the Coulomb-Coulomb-interactions.

The former behaviour cannot be due to disorder induced trapping, as the disorder was switched off. As the rise in charge carrier density is observed at approximately the same position for all the cases described above, we further investigated the role of that distance. Computing the Coulomb cut-off radius for the parameters given by Table 4.1 gives a value of 15.9 nm, i.e., a value that almost coincides with the local maximum of $n(x)$. Repeating the same experiments and measuring $n(x)$ for different cut-off radii and the extreme case of $\Delta = 0.1$ eV and $F_{ext} = 1 \times 10^{-3}$ V nm^{-1} (cf. Figure 4.13), reveals that the position of the local maximum of $n(x)$ is dependent on the chosen cut-off radius.
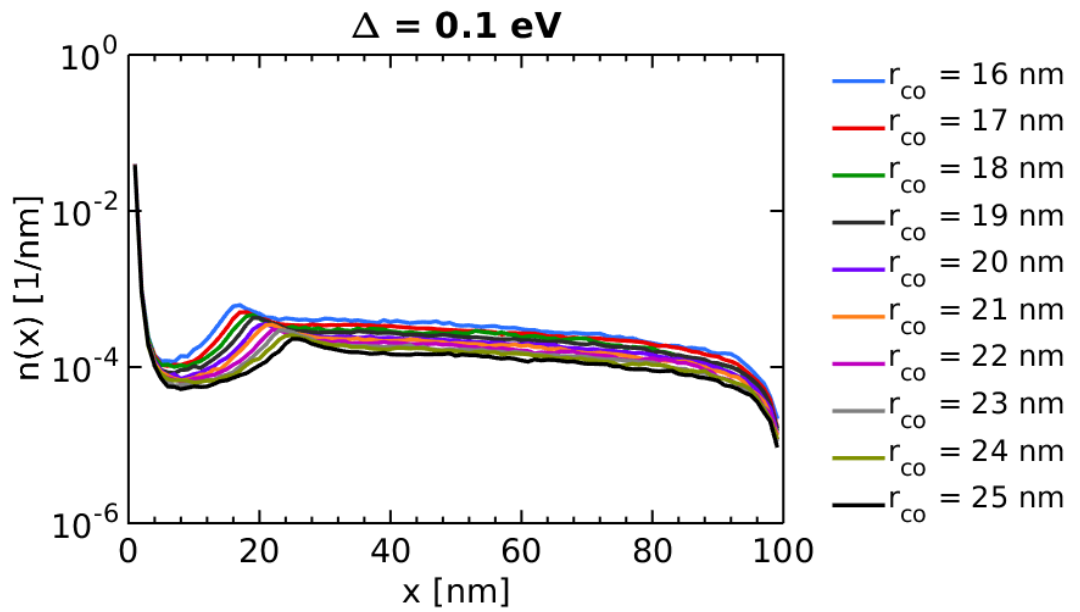
Figure 4.13: Layer averaged charge-carrier density $n(x)$ for the case of no disorder ($\sigma = 0k_BT$), field $F_{ext} = 1 \times 10^{-3}$ V nm^{-1} and the lowest barrier $\Delta = 0.1$ eV as a function of the distance from the electrode x, for different cut-off radii r_{co} for the Coulomb-Coulomb- interactions. The local maximum of $n(x)$ clearly moves to the right, for increasing cut-off radius.

The reason for this behaviour can be understood by investigating the layer averaged energy contribution due to the average charge carrier density $n(x)$. The latter is plotted for the borderline case of the 0.2 eV barrier and a field of $F_{ext} = 1 \times 10^{-2}$ V nm^{-1} in Figure 4.14. Here, the average energy contribution is calculated only due to the accumulation in the first and second layer after the electrode, which contain approximately 27 and three charges on average. The average contributions due to the remaining layers are neglected, as the third layer contains one and the remaining layers 0.6 charges on average.

Figure 4.14, reveals a higher energy and a larger slope due to the accumulation in the first two layers reaching to the approximate distance of the the cut-off radius, beyond which the slope of the curves correspond to the external field. As a result, charges in the area of the large slope will hop faster than charges after that area. This happens, even though Miller - Abrahams does not differentiate between hops down in energy. The reason is, that disorder is introduced, by the charges in the bulk, as noted by Ref. [18]. Hence, also in the disorder free case, a higher slope means a faster drift, as disorder can more easily be overcome. At the transition from the large to the small slope, charges will therefore accumulate, as those are not hopping to the right, as fast as charges are approaching that transition. Hence, charges at the transition will block other charges from the left, which increases the accumulation there, leading to a lower charge carrier density to the left.
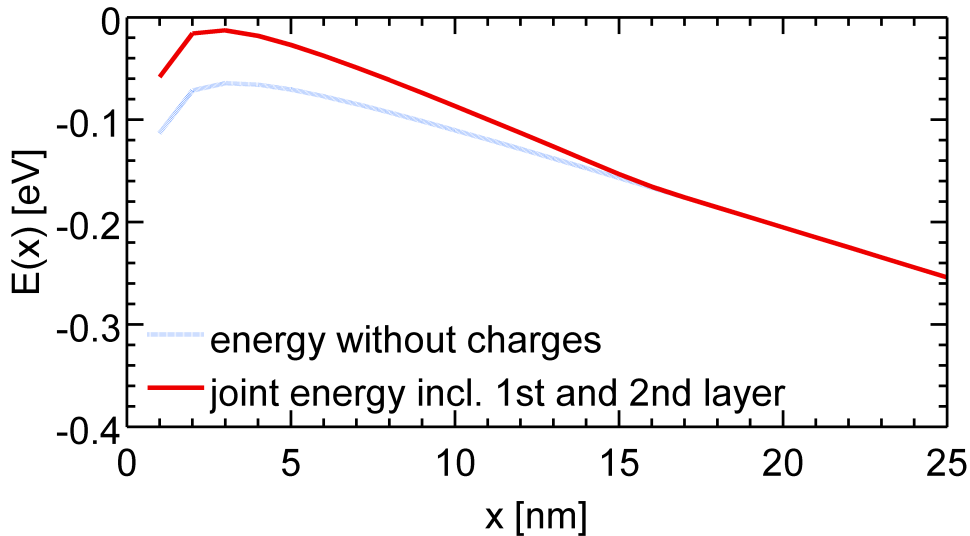

Figure 4.14: Layer averaged energy landscape due to own image charge, external field with (red) and without (blue) contribution due to charge accumulation in the first and second layer in the bulk as a function of the distance x from the electrode for a barrier Δ of 0.2 eV barrier and a field of $F_{ext} = 1 \times 10^{-2}$ V nm^{-1}. The transport level in the zero field case is at 0 eV, the Fermi energy at -0.2 eV.

From this discussion two conclusions can be drawn: (1) For the cases of the low barriers and low fields the simulations show artefacts for a bulk length of 100 nm, which condense as an accumulation of charges in the bulk at the distance r_{co}. These artefacts are due to space charges, which accumulate in the first two layers. (2) These leads to an effectively higher energy slope, which makes it, however, unnecessary to demand particles to travel 100 nm after considering them as escaped, as the high slope will make a hopping back

to the electrode very unlikely.

For the discussed cases, the cut-off radius is therefore set to 25 nm - the maximum possible for the device dimensions. The length of device is set to the same value, as 25 nm are more than enough to consider a particle having escaped. This is justified by conclusion (2) and also a far lower Coulomb cut-off radius, which would be the capture distance for the particles and their own images at zero field.

5 Literature Benchmarks for KMC

The KMC code to be used for the simulations, was developed from scratch. To be able to spot implementation errors as early as possible, the code was advanced from a basic stage to levels with increasing complexity. For each stage, simulations published in literature incorporating the appropriate level were selected to test the functionality of the code. An overview over the different literature set-ups is given in Figure 5.1.

(a) Set-up of Ref. [2].

(b) Set-up of Ref. [1].

(c) Set-up of Ref. [18].
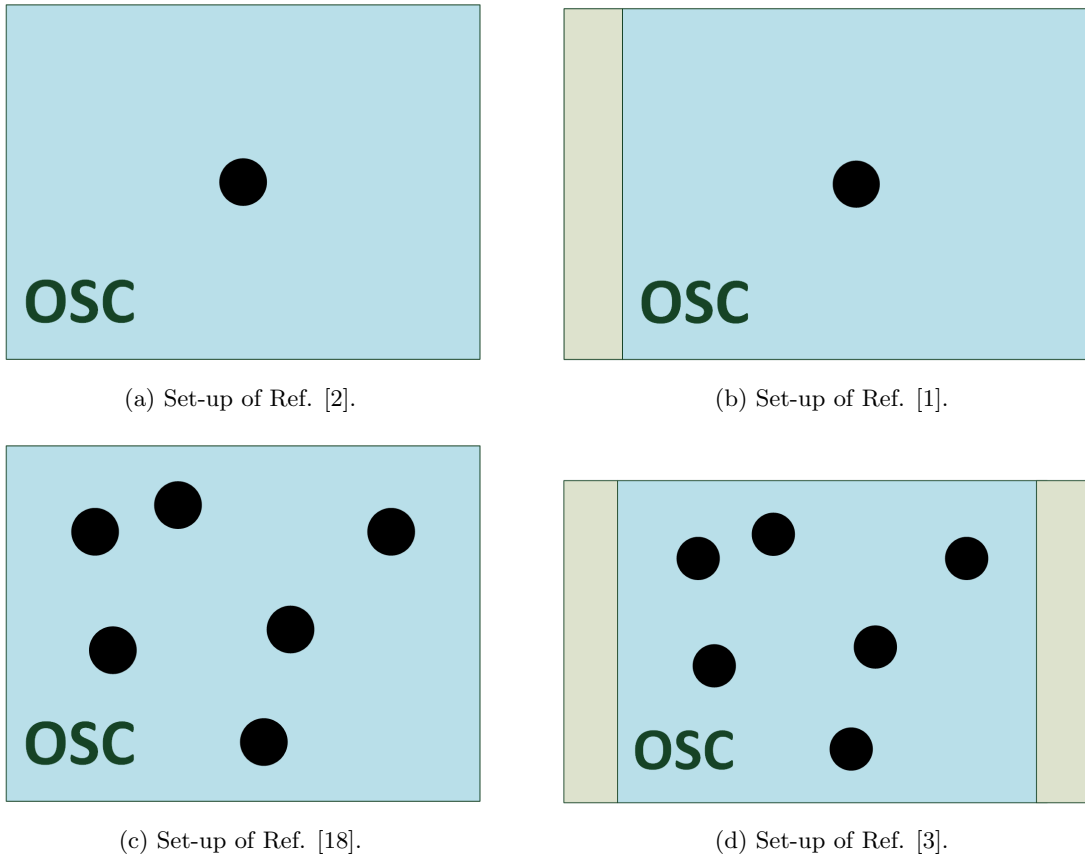
(d) Set-up of Ref. [3].

Figure 5.1: Set-ups of the simulations published in literature.

We started with an easy toy-system for single charges in bulk to replicate the results of Ref. [2] (Figure 5.1a). After this was accomplished, injection of electrons from a metal interface was implemented, without considering electron interactions (Figure 5.1b).[1] The next step was to introduce multiple charge interactions to the pure bulk-system (Figure 5.1c), as described in Chapter 4, and compare the results to Ref. [18]. Finally, the code as described in Chapter 4 was used to compare against the simulation of Ref. [3], in which charges were injected into a bulk material being sandwiched between two electrodes and in which their mutual interactions accounted for (Figure 5.1d).

For each of the benchmarks, the parameters for the simulations were taken from the respective publications or, if not fully specified or otherwise available, estimated. Thus, for each of the benchmarks, first the purpose of the reference simulation and the employed

simulation parameters are summarized. Then, the results of our KMC code are compared to the reference data and critically assessed.

5.1 Single charges in bulk

The reference publication   The paper of Marsh *et al.* [2], which presents a KMC model for organic photovoltaic devices, starts with a simple measurement of the mobility for single charges in the bulk. In that work, the DOS is Gaussian type with a standard deviation σ whose value is shown in Table 5.1. The model uses a Marcus type rate equation (cf. Equation 3.6 in Chapter 3.3), and allows only nearest neighbour hops. The size of the system is $70 \times 35 \times 35$ sites with an edge length a_{latt} of $1\,nm$. The external electric field F_{ext} is applied parallel to the longest extension of the active volume and varied between values of 3×10^6 $V\,m^{-1}$ and 1×10^8 $V\,m^{-1}$. The model incorporates periodic boundary conditions in all three dimensions. Table 5.1 gives a short overview over the simulation parameters, where ϵ, T, ν_0 and E_{reorg} as defined in Chapter 3.

Table 5.1: Parameters used in Ref. [2]

$rate$	$Marcus-type\,(Equation 3.6)$
$size$	$70 \times 35 \times 35$
a_{latt}	$1nm$
ϵ	4
T	$298K$
ν_0	$6.76 \cdot 10^{11}\,s^{-1}$
E_{reorg}[1]	$1.2 \cdot 10^{-19}\,J$
σ	$1 \cdot 10^{-20}\,J\,(= 61\,meV)$
F_{ext}	$varied$

The authors find a typical Poole-Frenkel-type behaviour of the mobility, i.e., μ depends on the applied electric field F_{ext} as:

$$\mu(F_{ext}) = \mu_0 e^{\gamma \sqrt{F_{ext}}}, \tag{5.1}$$

with μ_0 being the mobility without external field applied and γ a scaling pre-factor.

Tests   The results of this paper (red squares) have been reproduced with the single carrier version of the KMC code as depicted in Figure 5.2. Each measurement point of our simulations (black with errorbars) is averaged over eight different morphologies where each ran for a number of 10^6 hops.

It can be seen that our results match that of Ref. [2] very well, where the difference between the two curves is believed to be mainly due to the digitalization of the reference publication graph to make it usable here.
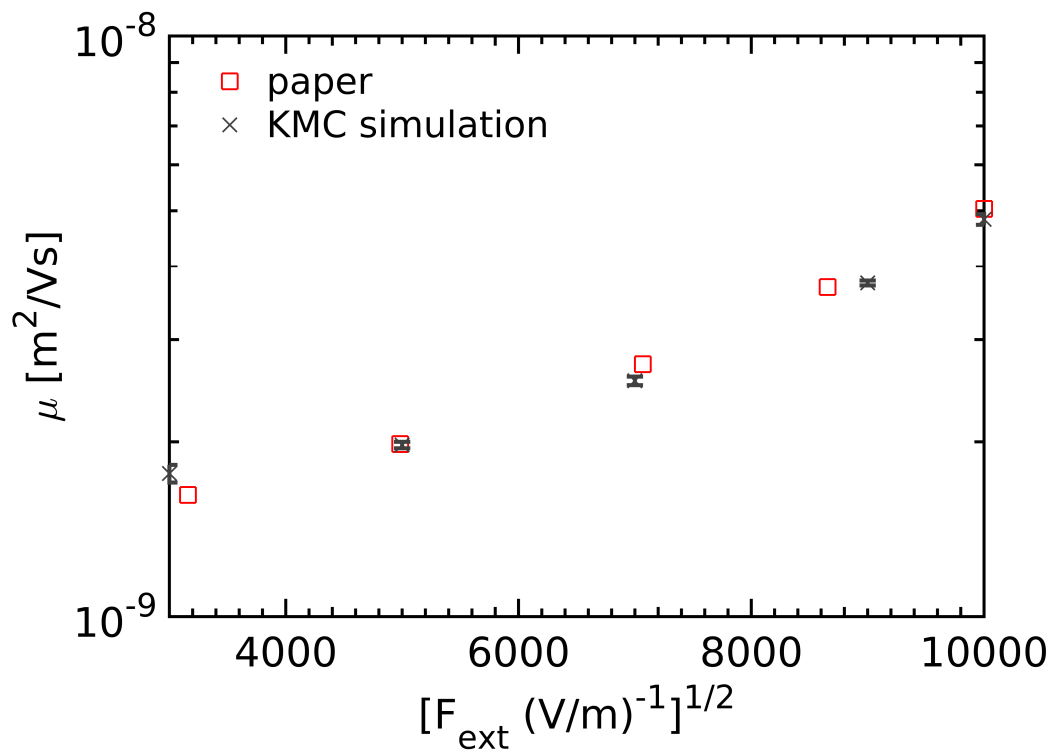
Figure 5.2: Mobility μ as a function of the applied electric field F_{ext}. Results of the presented code (black with error bars) compared to the values from [2] (red squares).

5.2 Metal Interface, single charge

The reference publication   In the work of Wolf *et al.* [1], the injection efficiency from a metal surface into the bulk is studied.

The bulk is discretized into $170 \times 170 \times 20$ sites. The DOS is Gaussian type with a standard deviation σ whose value is shown in Table 5.2. The way, injection was implemented in that work is equivalent to having single charges being injected along the z-direction from the metal surface into the bulk material. Additionally, there is a constant external electric field applied in the z-direction. Charges are regarded as having escaped after reaching the ninth layer after the metal surface, leading to an effective bulk size of $170 \times 170 \times 10$.

The metal contact has a Fermi energy E_F, however as only energy differences play a role in the assessment of Miller-Abraham rates, the mean of the DOS is taken to be zero and its difference from the Fermi level can be expressed by an energy barrier Δ. In order to incorporate a constant potential at the metal surface, the potential of image charges is considered.

The probability that one site of the bulk is chosen for injection is determined by the formula $P_{ij} = \frac{\nu_{ij}}{\sum\limits_{j \neq i} \nu_{ij}}$, where ν_{ij} is the hopping rate of jumps from a site i in the metal into a possible site j in the bulk. Injection into the bulk is only allowed perpendicular to the metal surface into the first two layers of the bulk. Considering only P_{ij} corresponds to an injection probability of unity where the value of P_{ij} determines the site into which injection takes place. However, to incorporate the possibility of a relaxation process within the metal, i.e., the particle will not arrive in the semiconductor, an additional factor f is introduced:

$$f = \frac{\sum\limits_{i \neq j} \nu_{ij}}{\nu_0 + \sum\limits_{i \neq j} \nu_{ij}}. \tag{5.2}$$

The factor normalizes the resulting injection efficiency $\phi_{inj} = \frac{n_{esc}}{n_{inj}} \cdot f$ by regarding the relaxation process happening at rate ν_0 as can be seen in Equation 5.2.

Within the bulk, hopping is allowed beyond nearest neighbours to all sites within a $5 \times 5 \times 5$ cube. The bulk incorporates periodic boundary conditions in x- and y- direction, where the edge length of one site was assumed to be $0.6\,nm$.

Table 5.2 gives a short overview over the simulation parameters. The parameter ν_0 is arbitrary, because the injection efficiency ϕ_{inj} is independent of time, and was, therefore, set to 1 s^{-1} in this table.

The results of the paper suggest an increasing injection efficiency for higher applied electric fields and lower barriers.

Tests   The parameters were taken from Table 5.2 with 1000 particles injected. For a better result, each simulation was done eight times such that an average efficiency could be calculated. It was watched carefully, that all particles either recombined or escaped before the maximum number of runs was reached.

Figure 5.3 shows a comparison between the simulation results of the injection efficiency (black with errorbars) and data from Ref. [1] (solid red line with circles). For high barriers $\Delta \geq 0.5$ eV, the test simulations are in accordance with the paper. However, for lower barriers, specifically for $\Delta = 0.2$ eV, the injection efficiency in our simulation shows an injection efficiency, which is an order of magnitude higher than in the paper.

Table 5.2: Parameters used in [1]

rate	$Miller - Abrahams$
$size$	$170 \times 170 \times 20$ (10)
a_{latt}	$0.6nm$
ϵ	3.5
T	$250K$
ν_0	$1\ s^{-1}$
γ	$5/a_{latt}$
σ	$80\ meV$
F_{ext}	$varied$

When looking at Figure 5.3a, there is a rapid increase in the injection efficiency prior reaching a saturation. However, the field value associated to the transition into saturation differs between the two curves. The value identified in the reference is with approximately 4×10^6 V cm^{-1} considerably higher than our prediction consistent with the field independent motion described below. The reason for the saturation with respect to the field is as follows: When the external field compensates or overcompensates the injection barrier due to Δ, the hops become independent of the field. Then, we observe a drift motion without the need to perform (field-assisted) hops upward in energy. This transition occurs, according to Figure 5.4 at a field strength of $F_{ext} = 15 \times 10^5$ V cm^{-1}, consistent with the onset of saturation in our simulation (black crosses with errorbars) in Figure 5.3a. We suppose, that the different behaviour in Ref. [1] results from a technical simulation detail: Most likely, the simulation is stopped before all carriers have left the bulk. If that is the case, the uncertainty of the injection efficiency greatly increases, as it is unclear which fraction of these left over particles would have escaped or recombined with the contact.
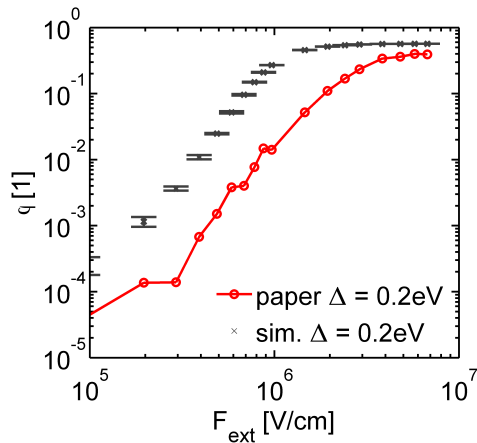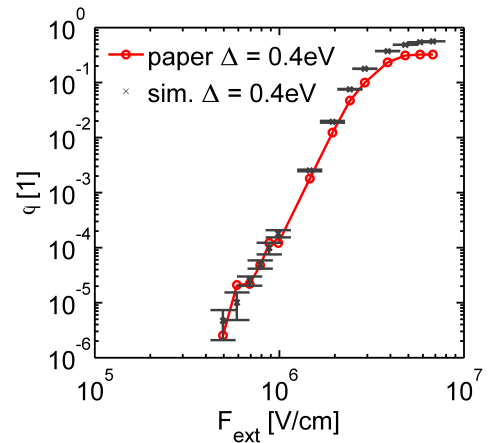
(a) Injection efficiency for $\Delta = 0.2\,eV$

(b) Injection efficiency for $\Delta = 0.4\,eV$

(c) Injection efficiency for $\Delta = 0.5\,eV$
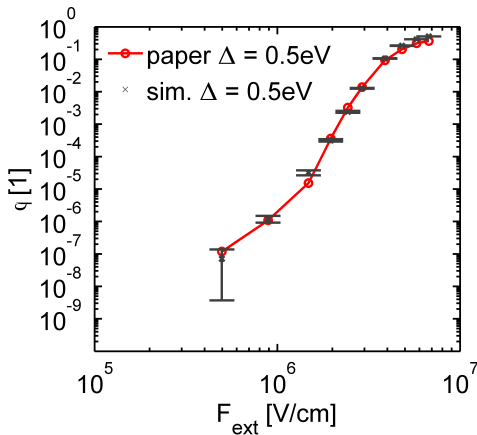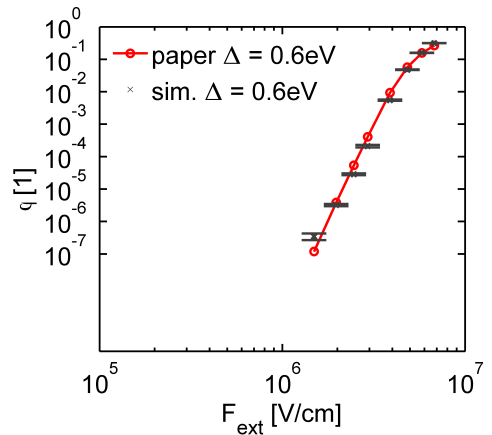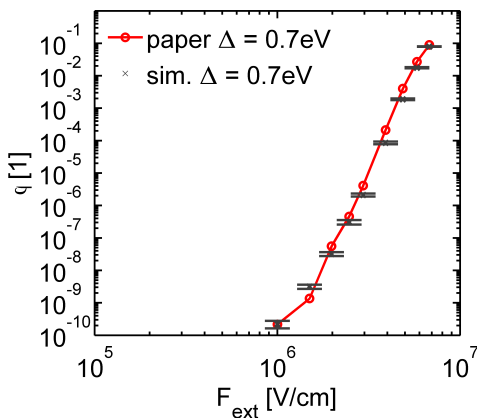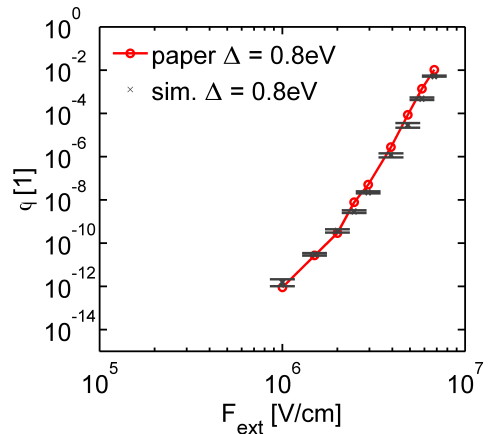
(d) Injection efficiency for $\Delta = 0.6\,eV$

(e) Injection efficiency for $\Delta = 0.7\,eV$

(f) Injection efficiency for $\Delta = 0.8\,eV$

Figure 5.3: KMC Simulation of injection efficiency ϕ_{inj} as a function of the electric field F_{ext} (black with errorbars) compared to data from [1] (solid red line)
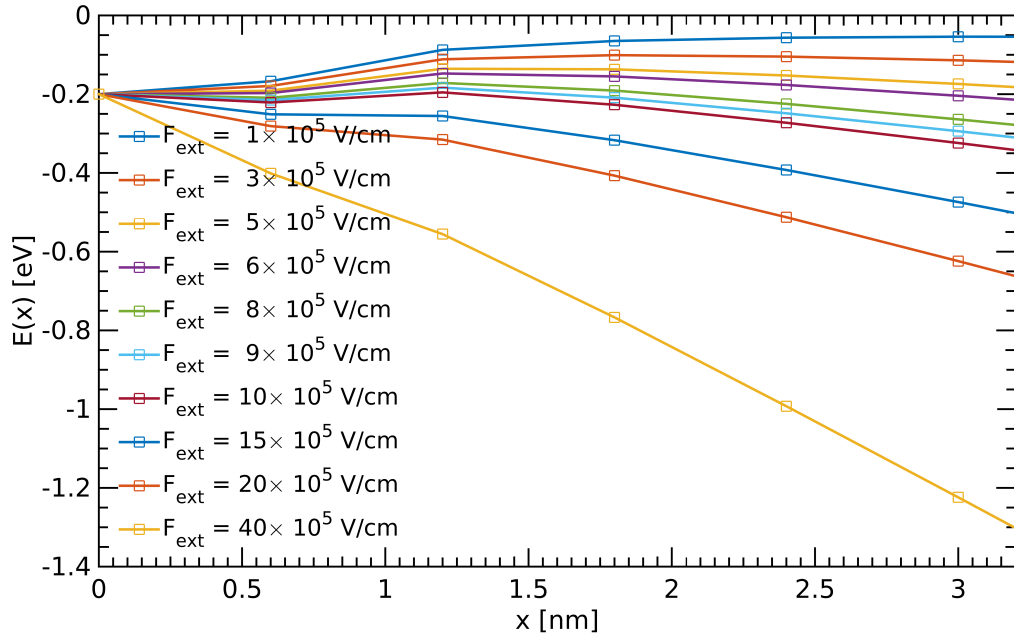
Figure 5.4: Potential energy $E(x)$ for different fields F_{ext} as a function of the distance x from the electrode for an injection barrier $\Delta = 0.2$ eV. The center of the DOS is located at $E = 0$. The potential energy is calculated at multiples of a_{latt} using Equations 3.10 and 3.13. For fields larger than $F_{ext} = 15 \times 10^5$ $\mathrm{V\,cm^{-1}}$, the field fully compensates the barrier Δ.

Figure 5.5 summarizes the simulation results. It can be seen clearly, that lower barrier heights Δ, lead to higher injection efficiencies. Also, the point, where the external electric field fully compensates the barrier Δ (e.g., for $F_{ext} = 15 \times 10^5$ $\mathrm{V\,cm^{-1}}$ for the 0.2 eV barrier as explained in Figure 5.4), can be observed for low barriers and high fields.

Figure 5.5: Simulation results for the injection efficiency ϕ of different barrier heights Δ. The lines are a guide for the eye.

5.3 Multiple charges in bulk

The reference publication   In the work of Zhou *et al.* [18], the mobility as a function of the carrier density is calculated for a disordered bulk of a single material with multiple c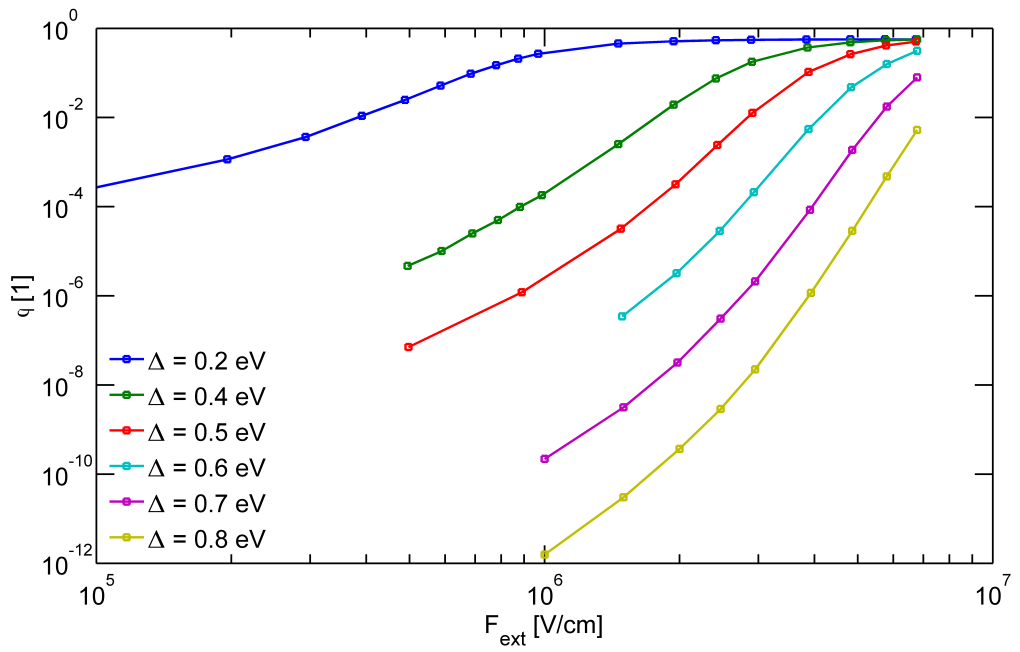harges, which experience each others Coulomb potential. A constant external field F_{ext} is applied. The bulk is discretized into $51 \times 51 \times 51$ sites of edge length $a_{latt} = 1$ nm. The simulation incorporates periodic boundary conditions.

Also, periodic replica of the charges outside the sites bulk are considered until converged (i.e. the $51 \times 51 \times 51$ cube is periodically replicated outside until adding these replicas does not change the result any more). These Coulomb interactions are calculated directly. Hopping is allowed only to nearest neighbours with a Miller-Abrahams rate. Table 5.3 shows the parameters used for the simulation. The value for γ was taken from Ref. [26], as the simulation in Ref. [18] was compared to that work. For the edge length a_{latt}, hopping rate ν_0 and temperature T no values were given in the paper and were chosen to be $1nm$, $1s^{-1}$ and 298 K for a comparison simulation.

Table 5.3: Parameters used in Ref. [18]

rate	$Miller-Abrahams$
size	$51 \times 51 \times 51$
a_{latt}	$1nm$
ϵ	4
T	$298K$
ν_0	$1\ s^{-1}$
γ	$10/a_{latt}$
σ	*varied*
$q \cdot F_{ext} \cdot a_{latt}/k_B \cdot T$	4

In the simulation, the standard deviation was varied betweend $\sigma = 0k_B \cdot T$ and $\sigma = 6k_B \cdot T$. It is argued that for high intrinsic disorders, the introduced disorder due to the Coulomb interaction is lifting the site energy of close-by particles, leading to a rapid increase in the mobility for high carrier densities. On the other hand, for low intrinsic disorder, Coulomb-Coulomb-interactions introduce additional disorder, which results in a decreasing mobility for high carrier densities.

Tests   Due to the fact, that energy is given in relative values of $k_B \cdot T$ in the reference publication, but no absolute value of the temperature T, the temperature had to be guessed to be $T = 298K$ in the simulation.

An absolute value of T is, however, necessary, as Coulomb-Coulomb-interactions have an absolute energy scale and can therefore only be given in terms of $k_B \cdot T$ if T is known. Also, it is rather unclear, if the values for γ and a_{latt} match. Therefore, the mobility can only be compared in a qualitative way.

The results of the simulation are plotted against the reference publication, which was normalized to the mobility of lowest disorder and lowest carrier density for better comparability in Figure 5.6. The simulation yields the same trends as the reference publication, namely an increase of the mobility for high disorders and high carrier densities and a decrease of the mobility for low disorders and high carrier densities. The deviation within the simulation for high disorders, $\sigma \geq 2\,k_B \cdot T$, is assumed to be due to the fact, that our

simulations were only done for one morphology, leading to larger morphology differences especially for that high disorders.
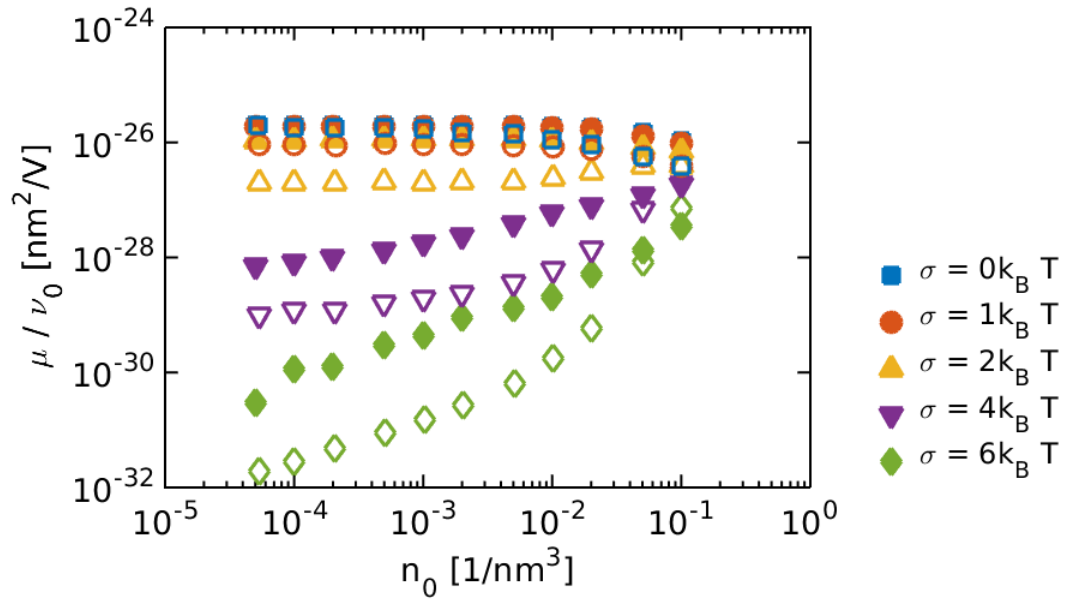

Figure 5.6: Mobility μ in units of the attempt frequency ν_0 as a function of the carrier density n_0 for different disorders in the energetic landscape σ given in terms of $k_B T$. Closed symbols: simulated with the code of this thesis (one run each). Open symbols: results of the reference publication (averaged over 10-50 runs)

5.4 Injection of multiple charges

The reference publication In the work of van der Holst *et al.* [3] simulations with Kinetic Monte Carlo, drift-diffusion and a Master-equation approach have been carried out. The current voltage characteristics that are used for comparison here, have been obtained with Kinetic Monte Carlo using the parameters given in Table 5.4. In Ref. [3], the organic semiconductor of one material is sandwiched between two electrodes of the same kind. This is a major difference to the code that was developed for this work, which only incorporates one electrode, and in which a particle escapes after it has reached the end of the bulk material. The presence of the second electrode increases the computational effort enormously, as they produce, in principle, an infinite number of images of the image charges, where up to 100 images are considered in Ref. [3].

Another difference in the calculation of the site energies is that in Ref. [3] Coulomb-Coulomb interactions are separated into short- and long range contributions. The former are included exactly up to a cut-off radius r_c of $10 \cdot a_{latt}$. The latter are included in a layer-averaged way, including a correction against double counting in the volume within the cut-off radius.

Similar to the work presented here, periodic boundary conditions are incorporated in the $y-$ and $z-$ direction, with a field F_{ext} applied in the $x-$ direction.

Hopping is allowed up to a distance of $\sqrt{3} \cdot a_{latt}$ (i.e., within a cube of size $3 \times 3 \times 3$).

Injection is handled in the same way as in this work (cf. Chapter 4), where a hop from and onto an electrode is handled similar to hopping in bulk. It is not mentioned, however, whether carriers may perform these hops other than perpendicular to the interface, as it is done in this work.

For the current-voltage characteristics, the barrier Δ was varied between 0 and 1 eV. The characteristics have been simulated for two different device lengths of 22.4 nm and 102.4 nm and Gaussian disorders $\sigma =$ of $3\,k_B \cdot T$ and $6\,k_B \cdot T$ (75 meV and 150 meV). Note here, indicated in Table 5.4, two different attempt frequencies ν_0 were used for the simulations. An attempt frequency of 3.5×10^{13} s^{-1} is used for the $3\,k_B \cdot T$ disorder simulations, whereas $\nu_0 = 1.4 \times 10^{16}$ s^{-1} is used for the $6\,k_B \cdot T$ disorder simulations.

Table 5.4: Parameters used in Ref. [3]

$rate$	$Miller - Abrahams$
$size$	$50 \times 50 \times 14$ / 64
a_{latt}	$1.6nm$
ϵ	3
T	$300K$
ν_0	3.5×10^{13} / $1.4 \times 10^{16}\ s^{-1}$
γ	$10/a_{latt}$
σ	3 / $6\,k_B \cdot T$
F_{ext}	$varied$

Tests The simulations run to compare against Ref. [3] used the parameters as explained above and in Table 5.4. The cut-off radius, following Equation 2.9, is 18.6 nm and therefore slightly higher than in the reference publication with a value of 16 nm.

To reproduce the $j - V$ curves given in Ref. [3], the field strengths F_{ext} corresponding to selected voltage values were estimated with $F_{ext} \approx V/d_x$, with d_x being the device

length. These yielded values for F_{ext} of 1×10^4, 1×10^5 and 1×10^6 $V\,cm^{-1}$, for which the corresponding current densities j were calculated.

The actual, total potential drop across the semiconductor was determined from integrating the layer-averaged charge-carrier density $n(x)$ obtained from the simulation twice using splines as explained in Chapter 4.4.

Figure 5.7 compares the $j - V$ curves obtained in Ref. [3], with the corresponding KMC simulations obtained in this work.
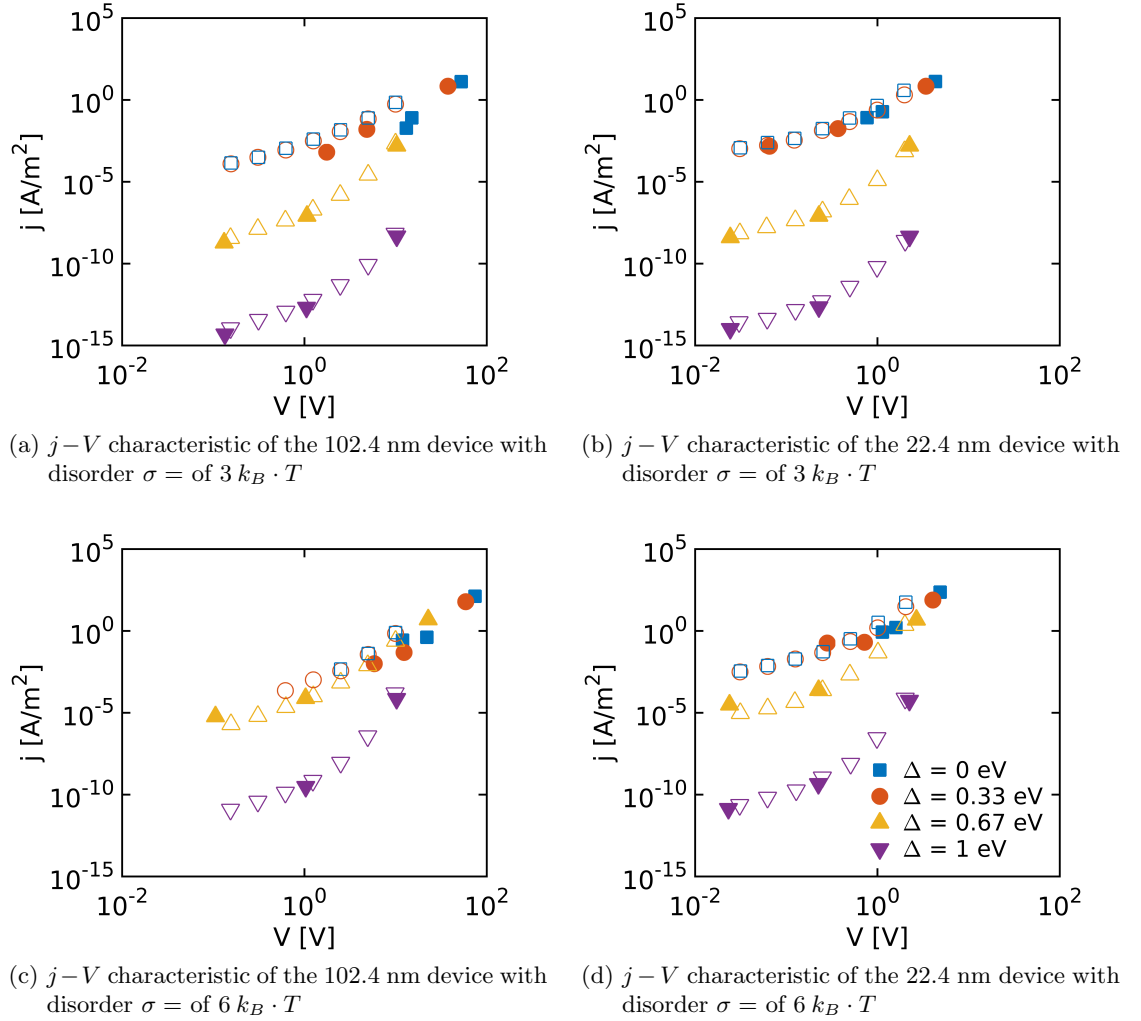

(a) $j - V$ characteristic of the 102.4 nm device with disorder $\sigma =$ of $3\,k_B \cdot T$

(b) $j - V$ characteristic of the 22.4 nm device with disorder $\sigma =$ of $3\,k_B \cdot T$

(c) $j - V$ characteristic of the 102.4 nm device with disorder $\sigma =$ of $6\,k_B \cdot T$

(d) $j - V$ characteristic of the 22.4 nm device with disorder $\sigma =$ of $6\,k_B \cdot T$

Figure 5.7: Current density j as a function of the applied voltage V for different disorders σ (upper and lower figures) and device lengths (left and right). Closed symbols refer to simulations based on the code of this thesis (one run each), while open symbols refer to results of the reference publication (averaged over 10-20 runs).

As can be seen in Figure 5.7, the lower disorder plots (closed symbols in Figure 5.7a and 5.7b)) match the results of the reference publication (open symbols) very well for all barriers. The high disorder plots (closed symbols in Figure 5.7c and 5.7d)) show a good match with the reference publication (open symbols) only for the high barriers $\Delta \geq 0.4\,eV$. The lack of correspondence between our calculations and the reference is more pronounced for $\Delta = 0.1\,eV$ than for $\Delta = 0.2\,eV$. Also, the results for the

long device appear to deviate more strongly from the reference publication. We believe that the different behaviour of our simulations originates from two reasons: (1) the high uncertainty of the calculated voltage V and, (2), the different test set-up of Ref. [3], where charges can accumulate in the interface layer at the counter-electrode.

The former will be investigated in detail in Chapter 6.2.2. There, it will be shown, that the uncertainty for fields higher than 1×10^5 V cm^{-1} exhibits 10% for $6 \, k_B \cdot T$ disorder and a barrier value of $\Delta = 0.2$ eV. The uncertainty increases with decreasing barrier value and increasing field, as it is observed in our comparison to Ref. [3].

The latter origin is more closely investigated by plotting the potential energy $E_{pot}(x)$ of a single, non-interacting charge inside the set-up of the reference publication. This potential, illustrated in Figure 5.8, accounts for the electric field F_{ext} and the repetitive image charges as elaborated in Ref. [3]. The black horizontal line on the right edge marks the position of the second electrode. The positions of the four barrier values Δ are marked with different symbols along this line. The energy of the two last sites before entering the second electrode are illustrated in red with an errorbar equal to the $6 \, k_B \cdot T$ disorder.

It can be seen, that the energy at the second electrode is for all fields, except for the lowest barrier lower than in the sheet before. This is recovered also in our simulation, i.e., as a slope down in energy is always treated in the same way by the Miller - Abrahams rate-equation.

In the case of low disorder, of $\sigma = 3 \, k_B \cdot T$, which is half the errorbar width as indicated in Figure 5.8, traps are not deep enough to accumulate charges in the layer forming the interface to the second electrode. Also, charges that approach a charge, located in this last layer, might lift the site energies of those charges and assist hops into the electrode. In this way, the apparent barrier for extraction formed for small offsets between E_F and the transport layer can be readily supposed.

In the case of high disorder, however, deep traps in the last layer cannot be neglected. This is especially the case for the lowest barrier $\Delta = 0.1$ eV in combination with the two lower fields (cf. Figure 5.8c - 5.8f). Owing to the low barrier a large number of charges is injected into the bulk and are, thus available for trapping. Once trapped, these charges form a repulsive potential near the second electrode. Consequently, charges arriving near the second electrode are prevented from escaping.

When comparing the potential energy $E_{pot}(x)$ of the long and the short device for different fields, depicted in Figure 5.8, no significant difference can be found. The higher discrepancy in the long device simulation for low fields is, therefore, assumed to be a result of the above-described formation of a repulsive potential at the second electrode. The traps in front of the second electrode are, however, lower in energy in the long device, as they are less affected by the lifting due to the accumulated charges in the layer next to the injecting electrode. This might lead to a higher accumulation right next to the counter electrode and, hence, a higher repulsive potential in the simulation of Ref. [3].

Finally, it has to be considered, that the reference publication averaged the results over ten to twenty runs, whereas here only one run is presented.

Our KMC code has proven to deliver the same trends as Ref. [3], with a good agreement for the low barrier values, within the error bounds due to the potential calculation and the fact, that the simulation were only done for one morphology. The deviations for the high disorder are a result of the two uncertainties above and the different set-up of our simulation, where charges will not accumulate at the end of the device.
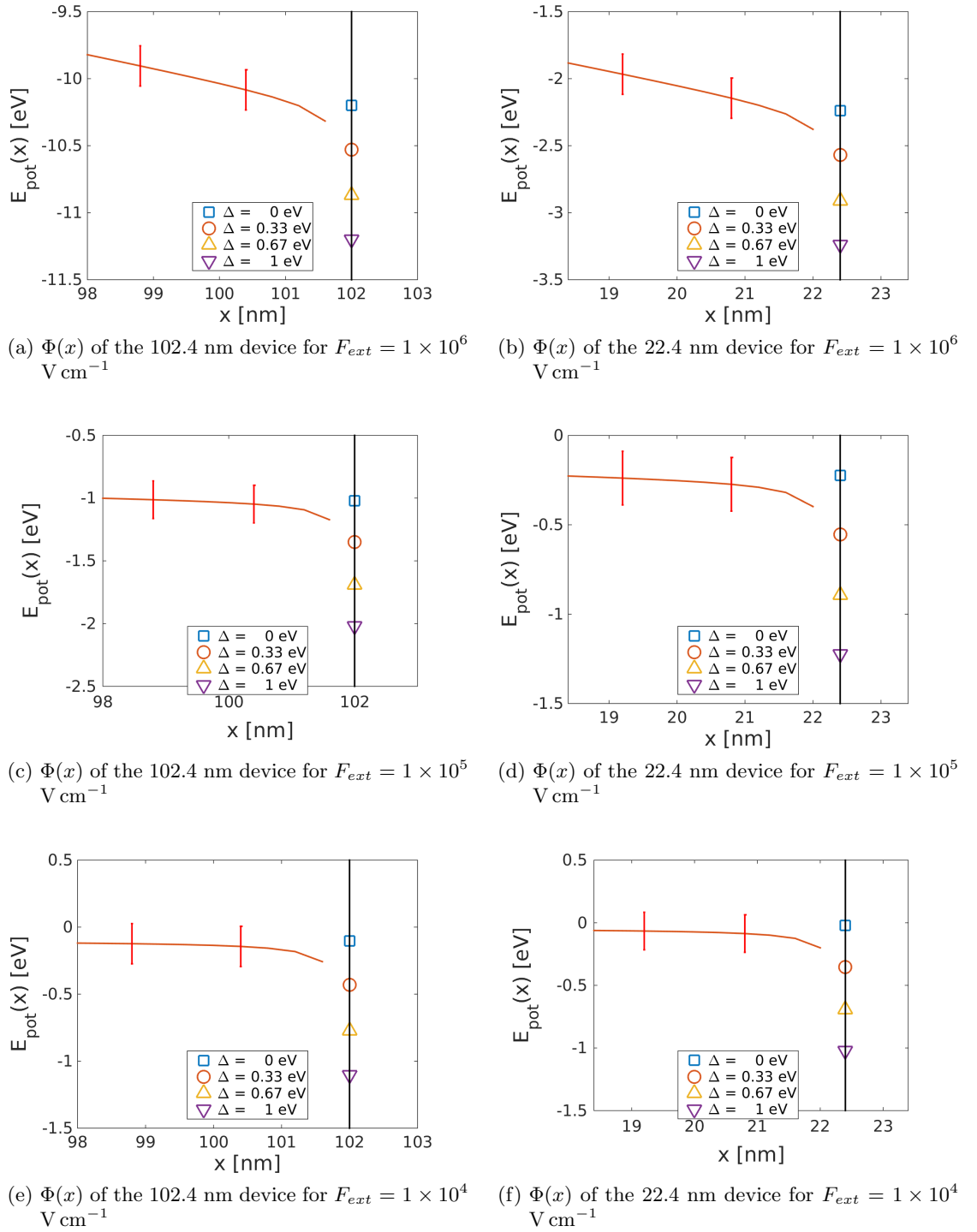
(a) $\Phi(x)$ of the 102.4 nm device for $F_{ext} = 1 \times 10^6$ V cm^{-1}

(b) $\Phi(x)$ of the 22.4 nm device for $F_{ext} = 1 \times 10^6$ V cm^{-1}

(c) $\Phi(x)$ of the 102.4 nm device for $F_{ext} = 1 \times 10^5$ V cm^{-1}

(d) $\Phi(x)$ of the 22.4 nm device for $F_{ext} = 1 \times 10^5$ V cm^{-1}

(e) $\Phi(x)$ of the 102.4 nm device for $F_{ext} = 1 \times 10^4$ V cm^{-1}

(f) $\Phi(x)$ of the 22.4 nm device for $F_{ext} = 1 \times 10^4$ V cm^{-1}

Figure 5.8: Potential $E_{pot}(x)$ of a single, non-interacting charge inside the set-up of the reference publication, due to the electric field F_{ext} and the repetitive image charges. The black horizontal line on the right edge, marks the position of the second electrode. The positions of the four barrier values Δ are plotted with different symbols. The energy of the two last sites before entering the second electrode are marked in red with an errorbar equal to the disorder $6\,k_B \cdot T$.

6 Simulation Results and Discussion

The goal of this chapter is to investigate, how injection is affected by the injection barrier, external field strength, and degree of disorder. The impact of these parameters is explored by considering an organic semiconductor with one interface towards a metal contact as introduced in Chapter 4.5.1. In this way, the large range of values, the aforementioned parameters can adopt, can be consistently considered.

The disorder σ is varied between $0\,k_B \cdot T$ and $1\,k_B \cdot T$ to see the influence of low disorder. For investigating the intermediate and high disorder cases, $3\,k_B \cdot T$ and $6\,k_B \cdot T$ were chosen, similar to the work of Ref. [3]. In our work, $1\,k_B \cdot T$ is equal to 25 meV at room temperature.

In the simulations, the external field F_{ext} takes values of 1×10^{-3}, 1×10^{-2} and 1×10^{-1} $V\,nm^{-1}$, in order to cover a wide and reasonable range (cf. Chapter 5.4).

The measurements are taken for values of the barrier Δ of 0.1, 0.2, 0.4 and 0.7 eV. The choice of the range was influenced by Ref. [1]. Though neither reference publication carried out simulations for a barrier of 0.1 eV, we expect to see a huge carrier accumulation and thus a significant influence on the current, we also look at that case.

All measurements, except for the $0\,k_B \cdot T$ disorder case, were taken eight times, in order to make the results independent of the random intrinsic energy landscape (being not present in the ordered $0\,k_B \cdot T$ case).

We start by discussing the current-field characteristics in terms of disorder and barrier height in Chapter 6.1. We then discuss the charge-carrier density we measured for the different cases and determine the resulting potential in Chapter 6.2. We conclude with Chapter 6.3 by comparing the current-field and current-voltage characteristics to selected analytical models introduced in Chapter 2.2.

6.1 Investigation of the Current Density

In Figure 6.1, the current density - field characteristics of the model system are shown. Each sub-figure shows the $j - F$ characteristics for different barrier values Δ. The disorder σ is increasing from left to right and top to bottom (i.e. increasing from Figure 6.1a to Figure 6.1d). Closed symbols represent the value obtained from the simulations, while the lines serve as a guide to the eye. In the following chapter, the corresponding errorbars are plotted. In should be stated here, that at high disorder $(6\,k_B \cdot T)$ and low fields, the current density results are less reliable.

The characteristics exhibit a rise in the current as a function of the field in all cases. This behaviour is also seen in Ref. [9], [11], [12], and [3].
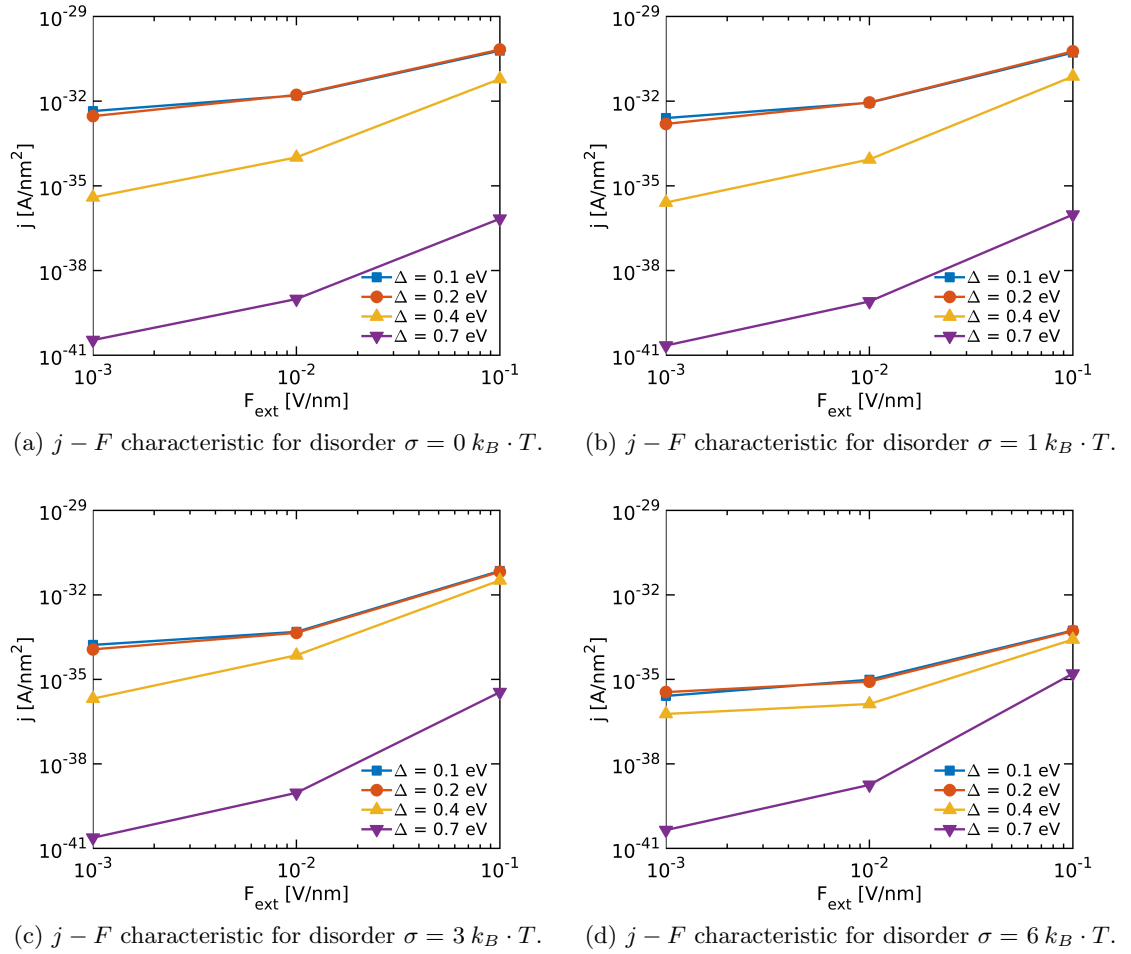

(a) $j - F$ characteristic for disorder $\sigma = 0\,k_B \cdot T$.   (b) $j - F$ characteristic for disorder $\sigma = 1\,k_B \cdot T$.

(c) $j - F$ characteristic for disorder $\sigma = 3\,k_B \cdot T$.   (d) $j - F$ characteristic for disorder $\sigma = 6\,k_B \cdot T$.

Figure 6.1: Current density j as a function of the externally applied field F_{ext} for different barriers Δ and disorders σ (increasing from left to right and top to bottom). Closed symbols represent the points for which simulations were done. The lines serve as guide to the eye. The current densities are averaged for eight different energy landscapes in Figures 6.1b to 6.1d.

However, we note two different regimes of the disorder dependent current density $j(\sigma)$. The regimes can be observed best when plotting the current density j as a function of the barrier value Δ at the highest field of $F_{ext} = 1 \times 10^{-1}$ V nm^{-1} (Figure 6.2). In the first regime, at $\Delta = 0.1$ eV and $\Delta = 0.2$ eV, j is decreasing with the disorder. In the second regime, however, at $\Delta = 0.7$ eV, j is increasing with increasing disorder. A

cross-over is observed at a barrier value of $\Delta = 0.4$ eV, where j increases from $0\,k_B \cdot T$ to $1\,k_B \cdot T$ disorder, but decreases for higher disorder.
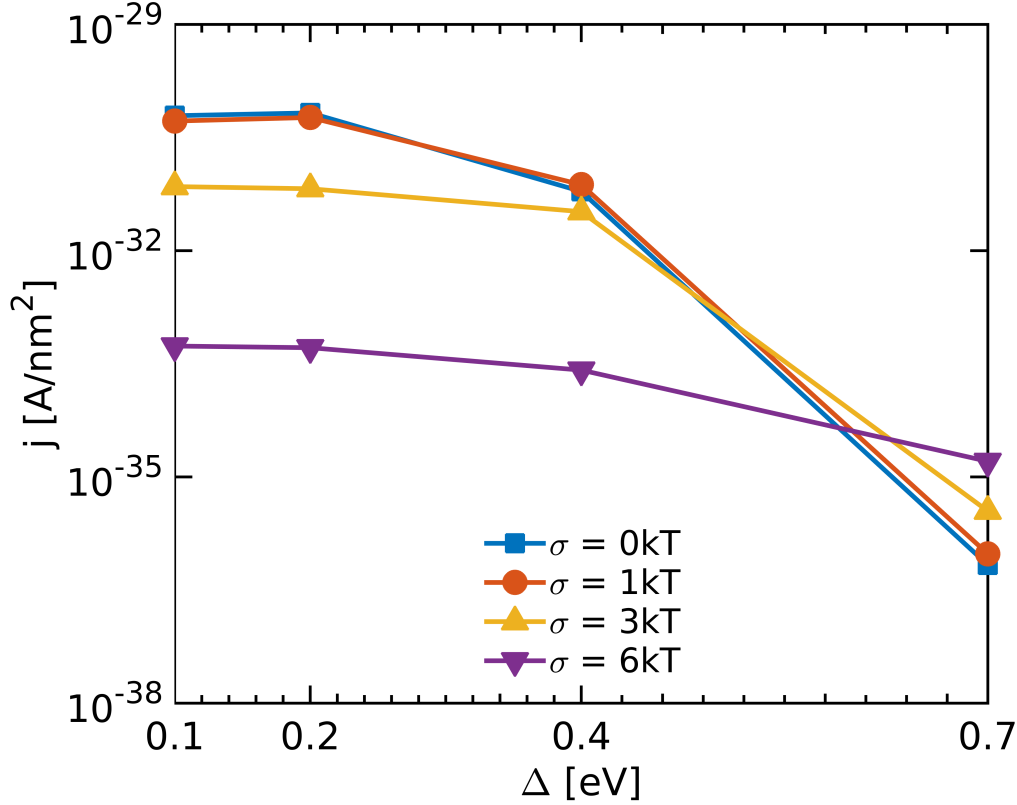

Figure 6.2: Current density j as a function of the barrier value Δ for the external field $F_{ext} = 1 \times 10^{-1}$ V nm^{-1} for different disorders σ. In the first regime ($\Delta = 0.1eV$ and $\Delta = 0.2eV$) j is decreasing with the disorder. In the second regime ($\Delta = 0.7\,eV$), j is increasing with increasing disorder. Between $\Delta = 0.2\,eV$ and $\Delta = 0.7\,eV$ (cf. values at $\Delta = 0.4\,eV$) we observe a cross-over of the two regimes.

Ref. [15] investigated the $j - \Delta$ dependence with a 3-D Master-Equation model of a sandwiched device. This reference utilizes the same model introduced in Ref. [3] (cf. Chapter 5.4). It has to be considered, that in that reference publication the attempt frequency ν_0 is different for $3\,k_B \cdot T$ disorder (3.5×10^{13}s^{-1}) and the $6\,k_B \cdot T$ disorder case (1.4×10^{16}s^{-1}). As the current density scales linearly with the attempt frequency ν_0, a comparison can easily be carried out.

In accordance with our results, the current density for $3\,k_B \cdot T$ disorder is higher than that for $6\,k_B \cdot T$ disorder for low barrier values when the same ν_0 is assumed. Moreover, the current density for low barrier values is decreasing with disorder. This behaviour is consistent with a simple rationale inspired by the model of Scott and Malliaras. We can estimate the dependence of the current density on the disorder by using the simple thermionic picture $j_{RS} = A^* T^2 \exp\left(-\frac{\Delta'}{k_B T}\right)$ (Equation 2.3), together with the effective Richardson constant as given by Scott and Malliaras by $A^* = \frac{16\pi\epsilon\epsilon_0 k_B^2 N_0 \mu}{e^2}$. In that picture, the current would depend linearly on the mobility. From the results of Chapter 5.3 we saw, that the mobility decreases for increasing disorder. Hence, we expect the

current density to decrease as well. A more detailed analysis will be given in Chapter 6.1.1.

However, there is no cross-over observed in Ref. [15] with the Master-Equation model at higher barrier values. As will be explained below, the cross-over is due to hopping processes confined between the electrode and the first layer. Such hopping processes can not be covered by a model that makes use of spatially averaged transition rates such as the Master-Equation model. In this approach, also the electrostatic potential due to space charges is only taken into account in a layer-averaged way, whereas our KMC simulations make use of the exact Coulomb-Coulomb-interactions and the microscopic hopping processes.

Further, Ref. [15] carried out KMC simulations for the sandwiched device. As discussed in Chapter 5.4, our system is difficult to compare against that of Ref. [15], in particular, since no explicit $j - \Delta$ relation is shown for the KMC simulation in that publication. Nevertheless, the trends observed from the $j-V$ curves given in Ref. [15] corroborate our findings: (1) The $j - V$ characteristic of the 100 nm device of the reference publication exhibits a higher current density for the 0.67 eV barrier at $6\, k_B \cdot T$ disorder than at $3\, k_B \cdot T$ disorder, when a voltage of 10 V is applied; this bias approximately corresponds to a field $F_{ext} =1 \times 10^{-1}$ V nm^{-1} in our system. In contrast to that, (2), at a barrier of 0.00 and 0.33 eV, the current density is lower at high disorder than at low disorder. This supports our idea, that present macroscopic models are not able to fully account for all effects present in an organic device.

In the following chapter we will investigate the dependence of the current on the disorder. Afterwards, the reason for the equivalence of the $j - F$ characteristics of the two lowest barriers will be investigated.

6.1.1 Current density as a function of disorder

In order to investigate the influence of the current density on the disorder, we plot j against the disorder parameter σ for constant barrier values (increasing from Figure 6.3a to 6.3d) and different fields F_{ext}.

Three different behaviours with respect to disorder can be identified. When investigating the two lowest barriers of 0.1 and 0.2 eV (Figures 6.3a and 6.3b), we see, (1), that the current density is decreasing for all field values with increasing disorder. For the intermediate and high barrier we additionally observe, (2), a rising current as a function of the disorder (e.g. at $\Delta = 0.7\, eV$ and $F_{ext} =1 \times 10^{-1}$ V nm^{-1} in Figure 6.3d), and (3) an apparent increase followed by a decrease in the current (e.g., at $\Delta = 0.4\, eV$ and $F_{ext} =1 \times 10^{-1}$ V nm^{-1}).

We interpret the three distinct trends observed in terms of the disorder-dependent bulk mobility as well as the influence of charge-carriers in the first layer after the interface. However, prior discussing the consequences of disorder, it is useful to turn first to the case of vanishing disorder. The positions of the transport levels are, given that there is only one particle present, determined by the external field and the potential of a particles own image charge. Figure 6.4 shows these discrete transport levels (triangles) for the three external fields used for the simulations and the four different Fermi levels (i.e., barrier values) marked with black squares in Figure 6.4.

We note that, on average, hops other than from the metal interface into the first two layers will only be favoured, when all sites in these layers have energies higher than the Fermi energy. We can, however, restrict our discussion here to the first layer, as the large value of γ that we have used here, is strongly suppressing large distance hops. Only when the energy of the sites in the first layer is lifted above the Fermi energy, the
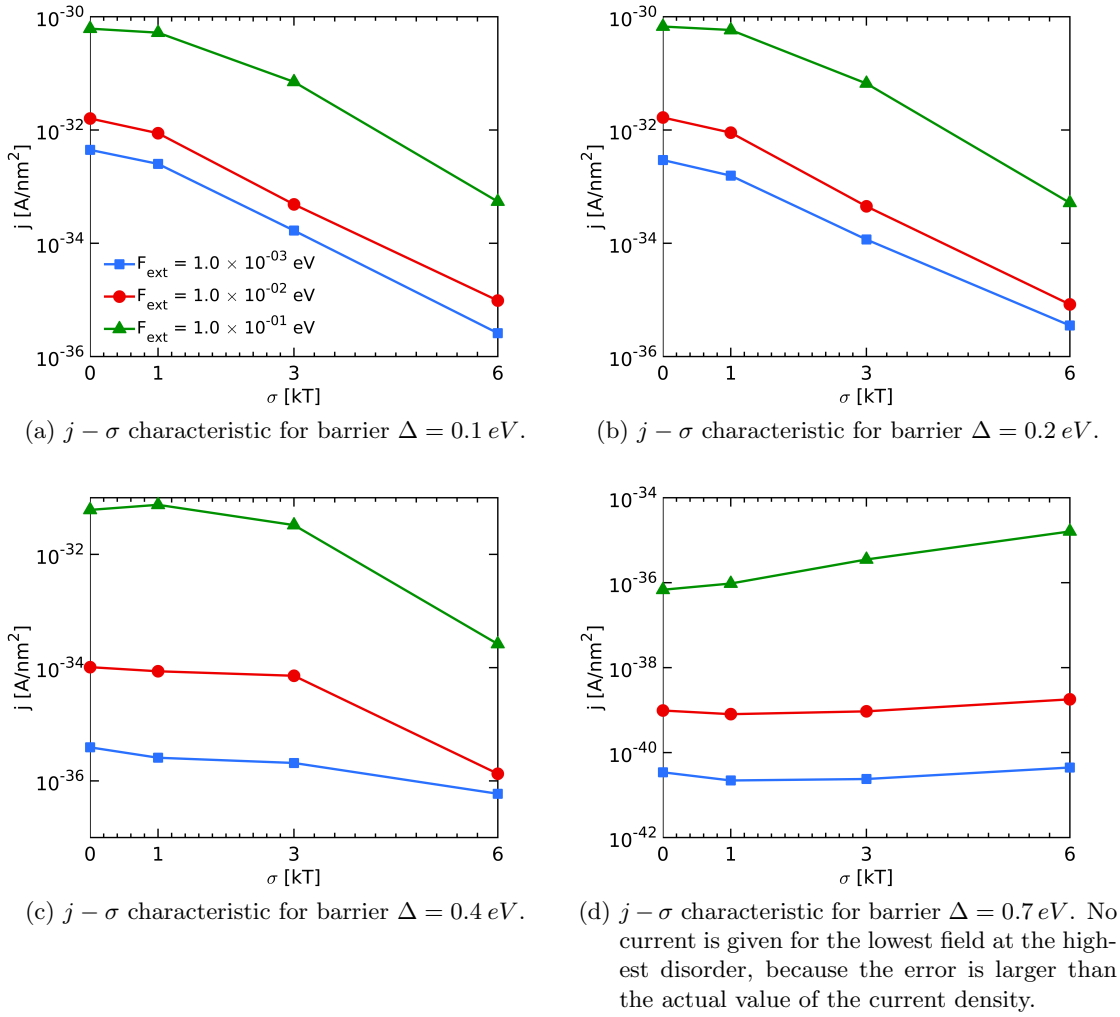
(a) $j - \sigma$ characteristic for barrier $\Delta = 0.1\,eV$.

(b) $j - \sigma$ characteristic for barrier $\Delta = 0.2\,eV$.

(c) $j - \sigma$ characteristic for barrier $\Delta = 0.4\,eV$.

(d) $j - \sigma$ characteristic for barrier $\Delta = 0.7\,eV$. No current is given for the lowest field at the highest disorder, because the error is larger than the actual value of the current density.

Figure 6.3: Current density j as a function of the disorder σ for different externally applied field F_{ext} and different barriers Δ (increasing from left to right and top to bottom). Closed symbols represent the points where simulations were done. The lines serve as guide to the eye. The current densities are averaged for eight different energy landscapes for $\sigma \neq 0$.

Boltzmann factor in the Miller - Abrahams equation will yield values larger than 1 and therefore hops from the electrode will have longer waiting times than particles in the bulk. Such a shift in site energies is achieved by charge accumulation in the first layer. We can therefore identify two scenarios, which are shown schematically in Figure 6.5.

If the Fermi energy is below the energy of the first layer ($\langle \epsilon_i \rangle < E_{Fermi}$, E_{Fermi1} in the figure), a hop from a first layer site back to the Fermi level (b) will occur with the same likelihood as to the next site in the bulk (c). If the Fermi energy is above the energy of the first layer ($\langle \epsilon_i \rangle > E_{Fermi}$, E_{Fermi2} in the figure), a hop from a first layer site will most likely be into the bulk (c). In the latter case, hops from the electrode into the bulk are preferred (a). Those might either be trapped due to their own and other particles image charges or hop between the electrode and the first layer. They are able to release charges into the bulk by lifting the energies of particles that are trapped nearby and enabling them to escape from deep traps, similar as reported by Zhou *et al.* [18]. Depending on the barrier Δ, a critical charge carrier density in the first layer may
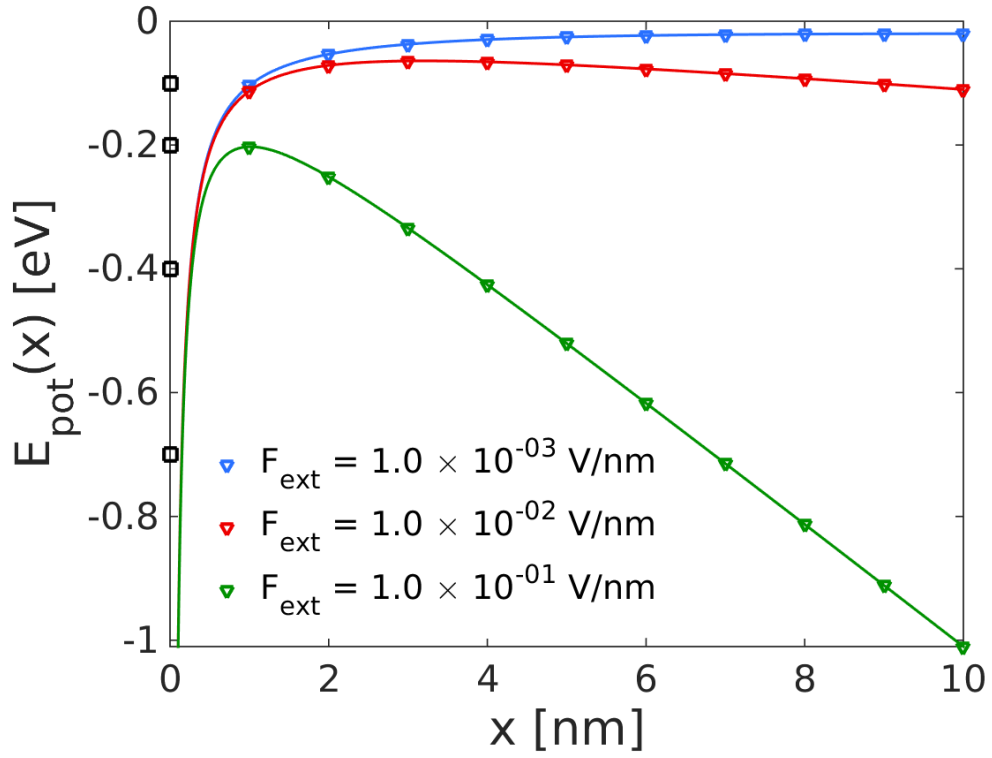
Figure 6.4: Potential energy E_{pot} of the transport levels, assuming vanishing disorder ($0\ k_B \cdot T$), for the three different external fields used for the simulations as a function of the distance from the electrode. Triangles mark the discrete levels of the hopping sites. The four different barriers Δ of 0.1, 0.2, 0.4 and 0.7 eV are marked with black squares at the position of the electrode ($x = 0$).

be reached. Moreover, the accumulation of charges in the first layer raises the energy of the first layer. Then, all sites in that layer have energies equal to the Fermi level at a critical charge-carrier density whose value depends on the barrier Δ. Hence, injection of more charges is impeded and the current is determined by the bulk properties. That case will be investigated in Chapter 6.1.2.

As can be seen, this is the case for the 0.1 and 0.2 eV barrier for the field $F_{ext} = 1 \times 10^{-1}$ V nm^{-1}. For all barriers, charge accumulation will be more relevant, if disorder is introduced and more charges are supposed to accumulate if the disorder and therefore the number of deep traps is increased in the first layer.
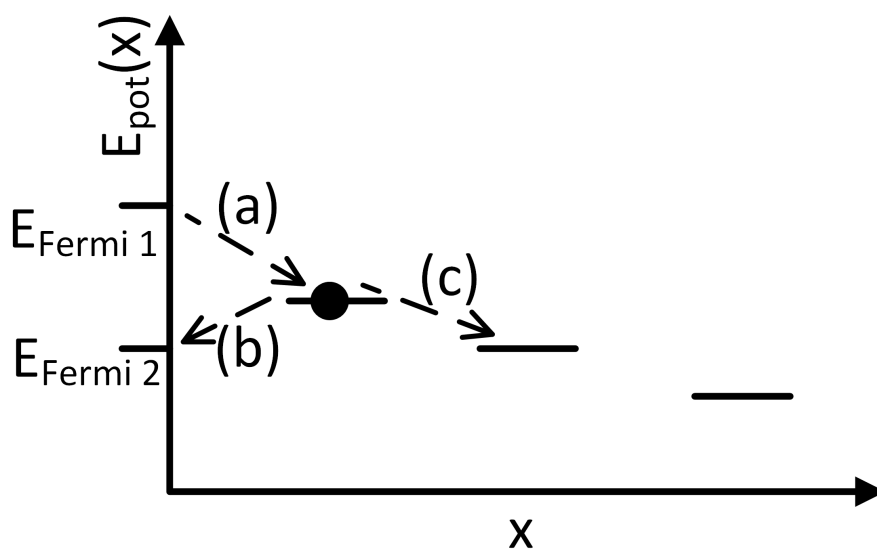
Figure 6.5: Schematic picture of the site energies as a function of the distance from
the electrode x. Downward hops are most likely and therefore the most
important hops. Due to the Miller - Abrahams rate equation, their rates are
independent of the energy difference. If the Fermi energy is below the energy
of the first layer (E_{Fermi1}), a hop from a first layer site will with the same
likelihood be either back to the Fermi level (b) or to the next site in the bulk
(b). If the Fermi energy is above the energy of the first layer (E_{Fermi2}), a
hop from a first layer site will most likely be into the bulk (c). In latter, hops
from the electrode into the bulk are preferred (a).

Decreasing current density   The first case is investigated exemplary by looking at the $\Delta = 0.2\,eV$ barrier. Figure 6.6a shows the evolution of the charge-carrier density in the first layer as a function of the disorder. Figure 6.6b shows the evolution of the average charge-carrier density in the bulk being determined between layers eight and 20 (cf. Chapter 6.2.1). We must note here, that the average bulk values for the lowest field and high disorder in Figure 6.6b has a huge uncertainty, as enhanced trapping in the bulk inhibits a representative average (cf. Chapter 6.2.1).
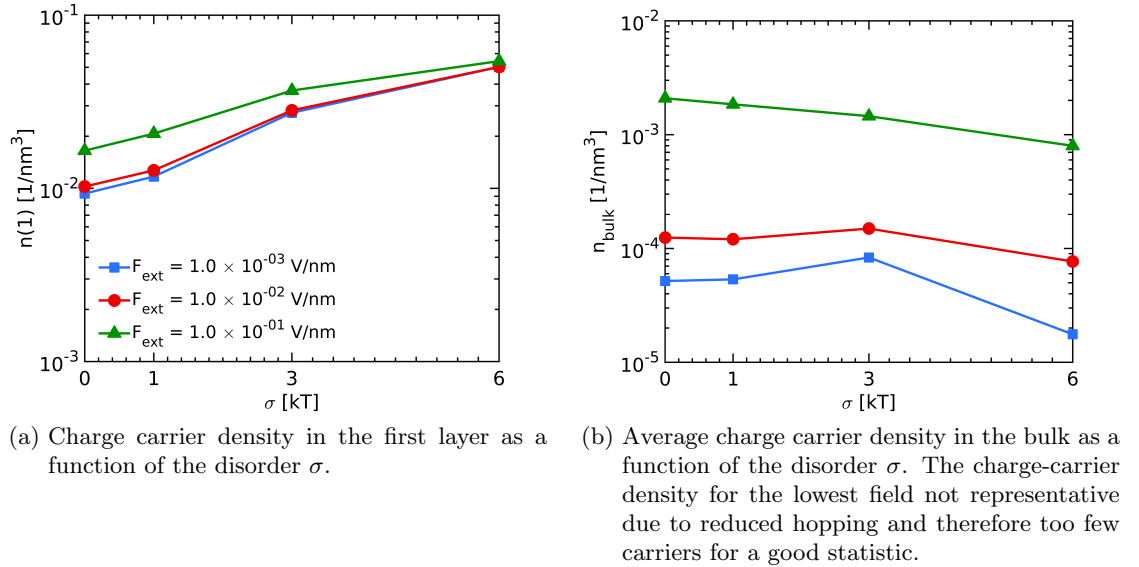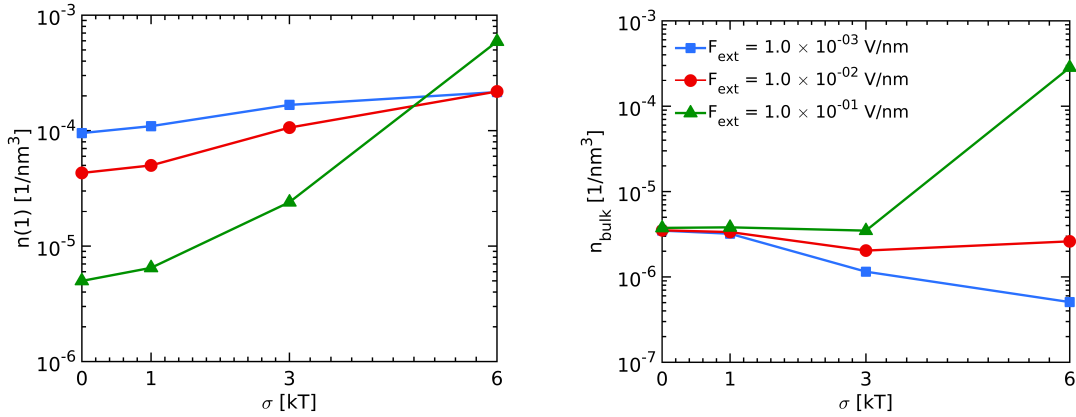

(a) Charge carrier density in the first layer as a function of the disorder σ.

(b) Average charge carrier density in the bulk as a function of the disorder σ. The charge-carrier density for the lowest field not representative due to reduced hopping and therefore too few carriers for a good statistic.

Figure 6.6: Charge carrier density in the first layer and average charge-carrier density in the bulk as a function of the disorder σ for different externally applied field F_{ext} and a barrier of $\Delta = 0.2\,eV$. Closed symbols represent the points where simulations were done. The lines serve as guide to the eye. Note that the ordinates in (a) and (b) have a different scale.

Figure 6.6a shows that more charges accumulate in the first layer as the disorder is increased. This is the result of more and deeper traps introduced with enlarging disorder. The charge-carrier density in excess of the critical charge-carrier density, i.e., the charges trapped in the first layer, is transferred to the bulk and only weakly dependent on σ (cf. Figure 6.6b). Hence, the current leaving the device, which is calculated by $j = n \cdot q \cdot \mu \cdot F_{ext}$, is determined by the mobility μ for a spatially constant charge-carrier density $\langle n \rangle(x)$ (cf. Figure 6.6b), and a constant field F_{ext} for different disorders. This is known as space-charge-limited current (SCLCL) in literature.[12] Corroborated by the results of Chapter 5.3, at constant charge-carrier density, a higher disorder must lead to a lower mobility and hence a lower current as observed. Another indicator is that the $j - F$ curves from Figure 6.1b are parallel in the logarithmic plot. Assuming that the mobility μ only dependent of the disorder σ, which is corroborated by Ref. [18] (cf. Chapter 5.3), one would expect the $j - F$ curves separated by a rigid offset. This is indeed observed.

Increasing current density   The effect of an increasing current density as a function of the disorder is strongest for the barrier of $\Delta = 0.7\,eV$ and the field $F_{ext} = 1 \times 10^{-1}$ $V\,nm^{-1}$ (cf. Figure 6.3d). At the same barrier, the current density is almost unchanged by the disorder for the lower fields. We will therefore study the effect on the $F_{ext} = 1 \times 10^{-1}$ $V\,nm^{-1}$ case. We start again by plotting the evolution of the charge-

carrier density in the first layer (Figure 6.7a) and the average in the bulk (Figure 6.6b) as a function of the disorder.

(a) Charge carrier density in the first layer as a function of the disorder σ.

(b) Average charge carrier density in the bulk as a function of the disorder σ.

Figure 6.7: Charge carrier density in the first layer and average charge-carrier density in the bulk as a function of the disorder σ for different externally applied field F_{ext} and a barrier of $\Delta = 0.7\,eV$. Closed symbols represent the points where simulations were done. The lines serve as guide to the eye. Note that the ordinates in (a) and (b) have a different scale.

Here, we can see that the charge-carrier density of the highest field evolves different than that of the lower fields. In contrast to the lower fields, the charge-carrier density in the first layer increases tremendously with increasing disorder. The charge-carrier density in the bulk is of the same order of magnitude for the three low disorders, where for the highest disorder it increases dramatically.

For the $6\,k_B \cdot T$ disorder, we assume the increased current to be driven by the high charge-carrier density in the bulk. In particular, as we saw in Chapter 5.3, that μ is dropping for an increasing disorder. We ascribe the increased current to a proximity effect present at the metal-organic interface, which is stronger than the effect of a decreasing bulk mobility. If we calculate the current leaving the device by $j = n \cdot q \cdot \mu \cdot F_{ext}$ and assume a slightly decreased mobility μ and a constant field F_{ext} we see that the current must be driven by the two order of magnitude increased charge-carrier density n, which outweighs the slightly decreased mobility.

Before we continue the discussion of the increased charge-carrier density in the bulk, we explain the increase in the first layer charge-carrier density. This can be easily explained by drawing the energy position of the transport levels (Figure 6.11). The discrete hopping sites have errorbars of the $6\,k_B \cdot T$ disorder attached. Obviously, for the case of no disorder, there is only one site with a barrier at $x = 1\,nm$ (i.e., upward hop from the metal). If a particle is placed there it may either hop away from the electrode or back to the electrode with approximately the same likelihood, as both hops are downward hops. As we only allow perpendicular hops back to the electrode, it will more likely hop into the bulk. From any point $x > 2\,nm$ the energy decreases to the right. Therefore, almost all particles which entered $x = 2\,nm$ leave the device. This explains, why the charge-carrier density in the first layer is slightly lower than that in the rest of the bulk for $0\,k_B \cdot T$ disorder. Compared to the $0\,k_B \cdot T$ case, more sites with lower energy are available at $x = 1\,nm$ with increasing the disorder; indicated by the errorbars in Figure 6.11. As all metal sites are occupied, also an increasing number of particles will hop into

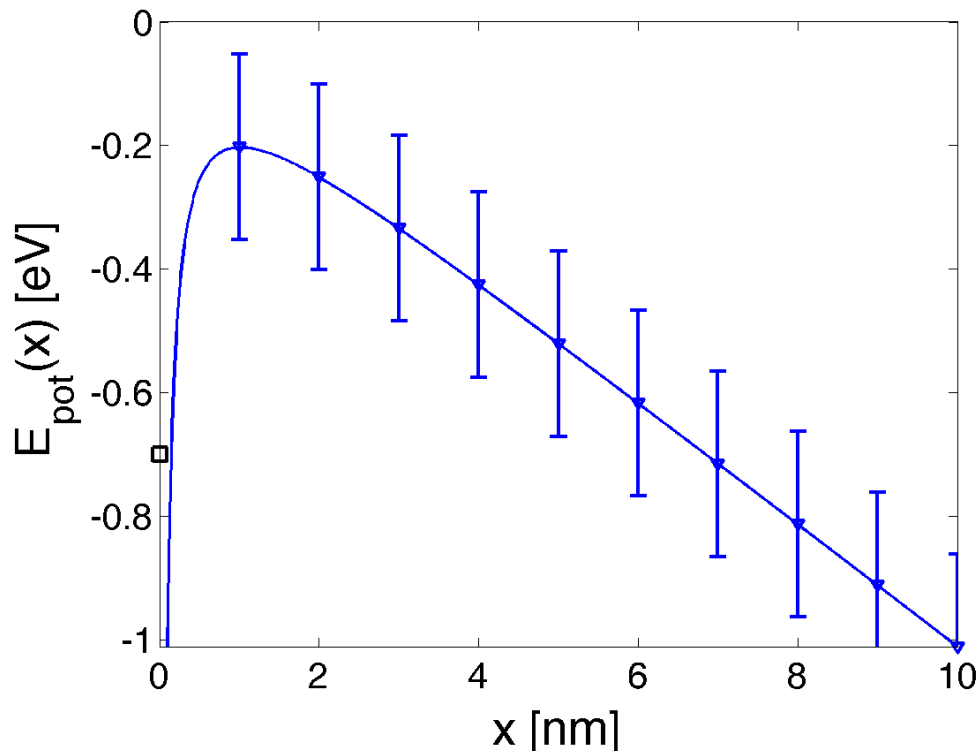the first layer at higher disorder.

Figure 6.8: Potential energy E_{pot} of the transport levels for the external field $F_{ext} = 1 \times 10^{-1}$ V nm^{-1} as a function of the distance from the electrode. Triangles mark the discrete levels of the hopping sites, the disorder σ is indicated by errorbars of $\pm 6 k_B T$. The barrier Δ of 0.7 eV is marked with a black square at the position of the electrode ($x = 0$)

It is still necessary, to explain, why the current increases, as the disorder increases from $0\, k_B \cdot T$ to $3\, k_B \cdot T$, although the charge-carrier density in the bulk is not increasing. We note, that the highest charge-carrier density in the first layer of 6×10^{-4} nm^{-3} is equal to one and a half particle per time and layer. This is not a number where we would expect a dramatic accelerating effect on the other bulk particles. However, we have to take into account that the charge-carrier density is averaged over a large number of runs and therefore a static picture. Here, we have to consider which processes is happening most often. From simulations, where we watched the actual hopping processes in the bulk, we saw, that for high barriers, the leading events are hopping processes from the electrode into the first layer and back. This ping-pong - like behaviour leads to an average charge-carrier density in the first layer which is very low. However, within a small number of runs, particles have visited a large fraction of the sites in the first layer. By that, it is very likely that a particle in the first layer approaches a particle in the second layer closely, which promotes the hop of the second layer particle into the bulk due to the Coulomb-Coulomb-repulsion, similar to the effect described by Zhou *et al.*. We denote this effect the proximity effect. Increasing the disorder leads to more favourable sites in the first layer, which in turn leads to an increased occupation of sites.

In order to justify this hypothesis, we recorded which sites were occupied at least once within 3×10^3 runs, which is of the same order of magnitude as the number of available
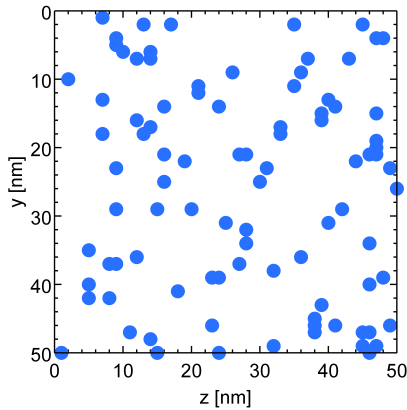
sites in the first layer. In Figure 6.9a, the visited sites in the first layer for $\sigma = 1\,k_B \cdot T$ are plotted. We can see that the coverage is much higher than in the second layer in Figure 6.9b. Moreover, by comparing the sites visited in the second layer with those in the first layer we see that for each site visited in the second layer, there is at least one next-nearest site being visited in the first layer. This is the prerequisite to enable the proximity effect described above. For an increased disorder of $\sigma = 3\,k_B \cdot T$, the coverage in the first layer increases alongside with a large number of "clusters" of nearest neighbour sites. This is consistent with a higher current density prediction in the simulation.
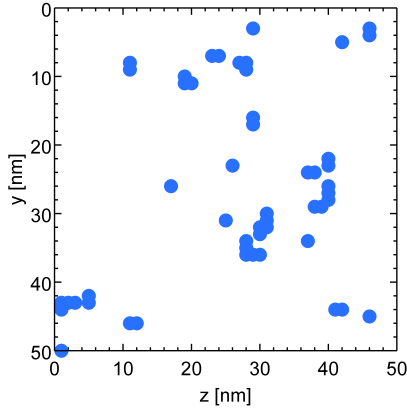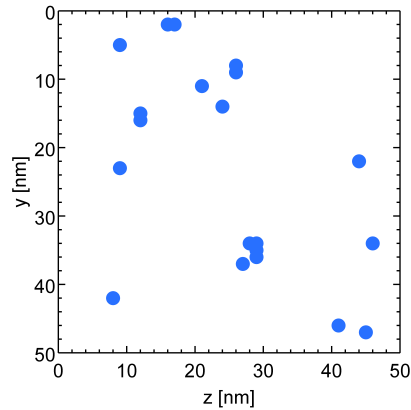

(a) Occupied sites in the first layer after 3×10^3 runs for $\sigma = 1\,k_B \cdot T$.
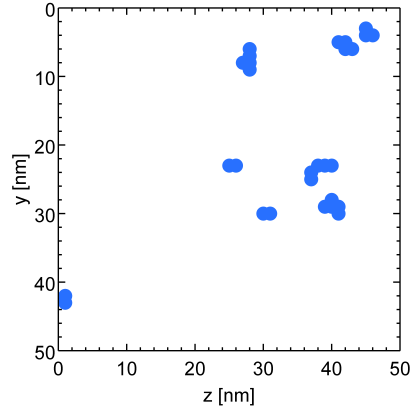
(b) Occupied sites in the second layer after 3×10^3 runs for $\sigma = 1\,k_B \cdot T$.

(c) Occupied sites in the first layer after 3×10^3 runs for $\sigma = 3\,k_B \cdot T$.

(d) Occupied sites in the second layer after 3×10^3 runs for $\sigma = 3\,k_B \cdot T$.

Figure 6.9: Sites in the first and second layer (left and right) that have been occupied at least once after 3×10^3 runs for disorders σ of $1\,k_B \cdot T$ and $3\,k_B \cdot T$ (top and bottom) for an injection barrier $\Delta = 0.7$ eV and $F_{ext} = 1 \times 10^{-1}$ V nm^{-1}.

Increase followed by decrease   For the $\Delta = 0.4\,eV$ barrier and the $F_{ext} = 1 \times 10^{-1}$ V nm^{-1} field, we observe an increased current density when increasing the disorder from $0\,k_B \cdot T$ to $1\,k_B \cdot T$. This is followed by a decreased current density for higher disorder. Similar to the $\Delta = 0.7eV$ barrier, the charge-carrier density in the first layer is increasing with higher disorder (Figure 6.10a). The slightly increased current from $0\,k_B \cdot T$ to $1\,k_B \cdot T$ can again be explained by the proximity effect explained above.

Already for the $3\,k_B \cdot T$ disorder, the charge-carrier density in the first layer reaches

comparable size as for the $\Delta = 0.2$ eV barrier, which enhances the SCLC, described earlier, giving rise to a decreased current.

From $3\,k_B \cdot T$ to $6\,k_B \cdot T$ the charge-carrier density in the bulk only weakly increases. Hence, the decreased current density is due to the increased disorder in the bulk, as for the $\Delta = 0.2$ eV barrier.
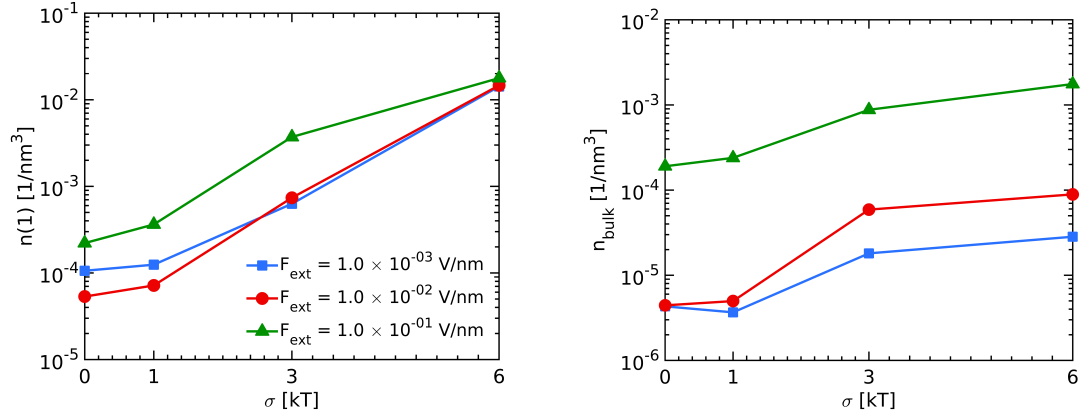
(a) Charge carrier density in the first layer as a function of the disorder σ.

(b) Average charge carrier density in the bulk as a function of the disorder σ.

Figure 6.10: Charge carrier density in the first layer and average charge-carrier density in the bulk as a function of the disorder σ for different externally applied field F_{ext} and a barrier of $\Delta = 0.4\,eV$. Closed symbols represent the points where simulations were done. The lines serve as guide to the eye. Note that the ordinates in (a) and (b) have a different scale.

6.1.2 Similar characteristics at the lowest barriers

If we look at the $j - F$ characteristics in Figure 6.1, we can see that there is, independent of the disorder σ, only a minor difference in the current-density of the lowest barriers of 0.1 and 0.2 eV. The same is observed by Ref. [3] for low barriers.

We will investigate this by plotting the transport level for both barrier values and the highest field of $F_{ext} = 1 \times 10^{-1}$ V nm^{-1} in Figure 6.11.
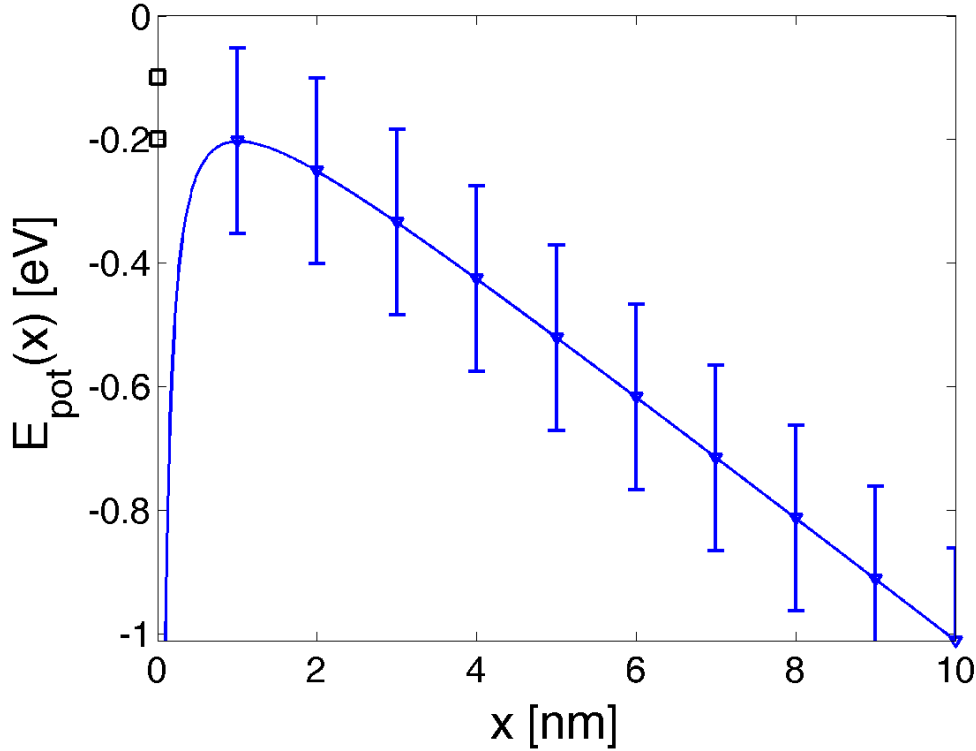

Figure 6.11: Potential energy E_{pot} of the transport levels for the external field $F_{ext} = 1 \times 10^{-1}$ V nm^{-1} as a function of the distance from the electrode. Triangles mark the discrete levels of the hopping sites, the disorder σ is indicated by errorbars of $\pm 6 k_B T$. The barriers Δ of 0.1 and 0.2 eV are marked with black squares at the position of the electrode ($x = 0$)

When the injection experiment is started, charges will hop from the electrode onto the sites in the first layer until the energy of a large fraction of sites in that layer has an energy above the Fermi level. This is because all sites in the metal may be injecting sites and hence a hop from the electrode is more likely (due to the large number of carriers in the metal) than a hop in the bulk, unless it is energetically more favourable to hop in the bulk. This is shown schematically and explained in Figure 6.12.
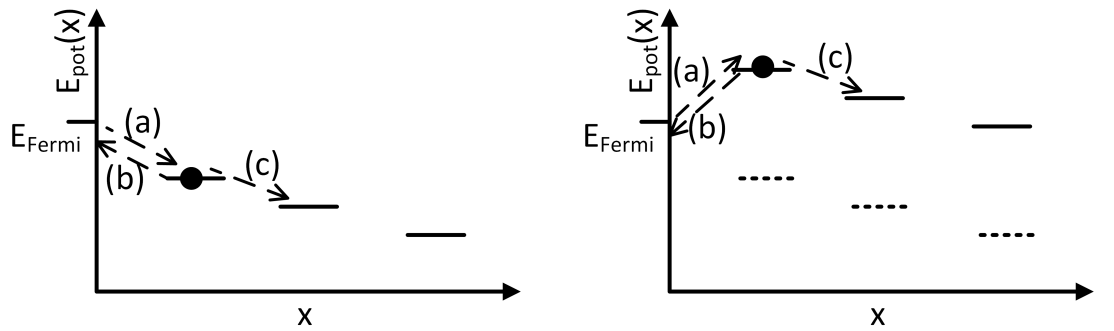
(a) When the injection is started, the energy levels in the bulk are below the Fermi energy E_F.

(b) After the system has thermalized, the average energy levels in the bulk are lifted above the Fermi energy E_F, due to charge accumulation in the first layer (evolution from dashed to solid lines).

Figure 6.12: Schematic picture of the site energies as a function of the distance from the electrode x for low barrier values Δ. When the injection starts (Figure 6.12a), the energy levels in the first layer of the bulk are below the Fermi energy E_F. As a result hops from the electrode into the bulk are favoured ((a) in Figure 6.12a) amongst hops from the bulk to the electrode (b). Jumps into the next layer are less likely, though a favourable energy (c), because all sites of the electrode are filled. As the system evolves in time, the charge accumulation in the first layer leads to an increase of the average energy in the bulk (Figure 6.12b). Then, we find an equilibrium of downward hops to the electrode (a), upward hops from the electrode (b) and hops into the bulk (c). Note that also downward hops from the electrode into the bulk are possible, as not all sites in the first layer are below the Fermi energy. This can, however, not be drawn in this simplified picture.

In order to corroborate this, we have investigated the distribution of the site energies in the first layer for an external field $F_{ext} = 1 \times 10^{-1}$ V nm^{-1} for the 0.1 (Figure 6.13a) and 0.2 eV (Figure 6.13b) barrier. We can see, that sites above the Fermi energy (E_F) are occupied (red) in both cases; however, there is still a small number of unoccupied sites (blue) below that energy.

(a) Energy distribution of occupied (red) and un-occupied (blue) sites in the first layer for the 0.1 eV barrier.

(b) Energy distribution of occupied (red) and un-occupied (blue) sites in the first layer for the 0.2 eV barrier.
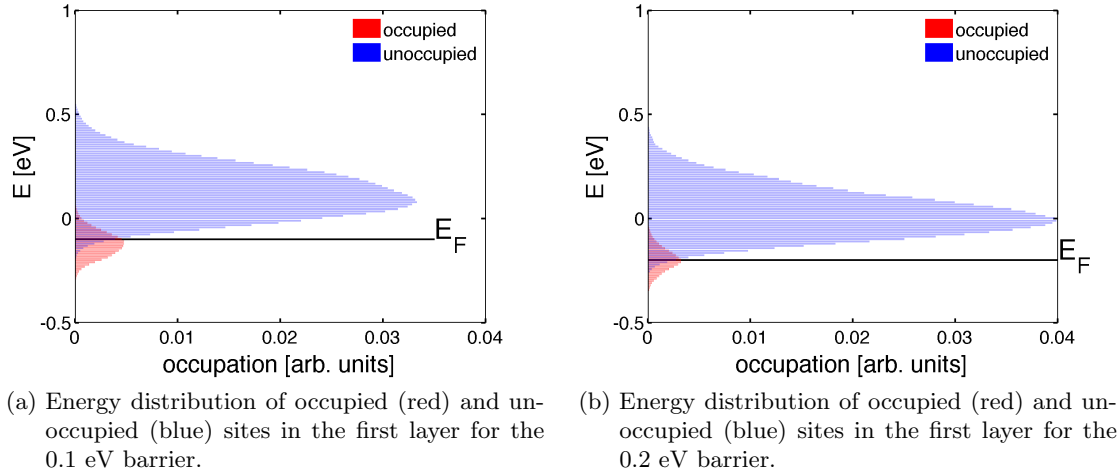
Figure 6.13: Number of sites (abscissa) of particular energy E in the first layer of the 0.1 (Figure 6.13a) and 0.2 eV (Figure 6.13b) barrier. The disorder is $3\,k_B \cdot T$ and the external field $F_{ext} = 1 \times 10^{-1}$ V nm^{-1}. Occupied sites are marked in red, unoccupied sites are marked in blue. The zero point of the energy is the transport level. Both experiments were only done for a single morphology until converged.

As the site energies associated to the 0.1 eV barrier are higher than in the 0.2 eV barrier case, more charges will accumulate in the first layer for the lower of the two barriers, i.e., $\Delta = 0.1$ eV. When comparing the number of occupied sites from Figure 6.13a and Figure 6.13b (area of the red histogram), clearly more sites are occupied for the $\Delta = 0.1$ eV barrier. With increasing disorder, this charge-carrier density will increase as well, as more traps are available. Both can be seen in Figure 6.14a.

In Figure 6.14b we can see that the charge-carrier density in the bulk is independent of the barrier and only weakly dependent on σ. We presume that the reason for this behaviour is that in both cases the Fermi energy is close to or above the potential energy in the first layer. If that is the case, sites in the first layer get occupied until a certain fraction of unoccupied sites below the Fermi energy remains. Then, consequently, the number of unoccupied sites below the Fermi energy is mostly independent of the disorder and the barrier. For the $\Delta = 0.1$ eV barrier, we determined this number to be 0.8%, where for the $\Delta = 0.2$ eV it is 0.45%. As these numbers were determined from the single morphology experiment depicted in Figure 6.14, i.e., associated with a certain uncertainty, we note that the values are in the same order of magnitude. In a first approximation, this number determines how many particles can enter the bulk per time, which leads to a charge-carrier density in the bulk only weakly dependent of the disorder, as will be discussed in the following section. As argued for the 0.2 eV barrier in Chapter 6.1.1, the current leaving the device is determined by the mobility at a constant charge-carrier density known as SCLC. Hence the $j - F$ characteristics of the low barriers coincide.
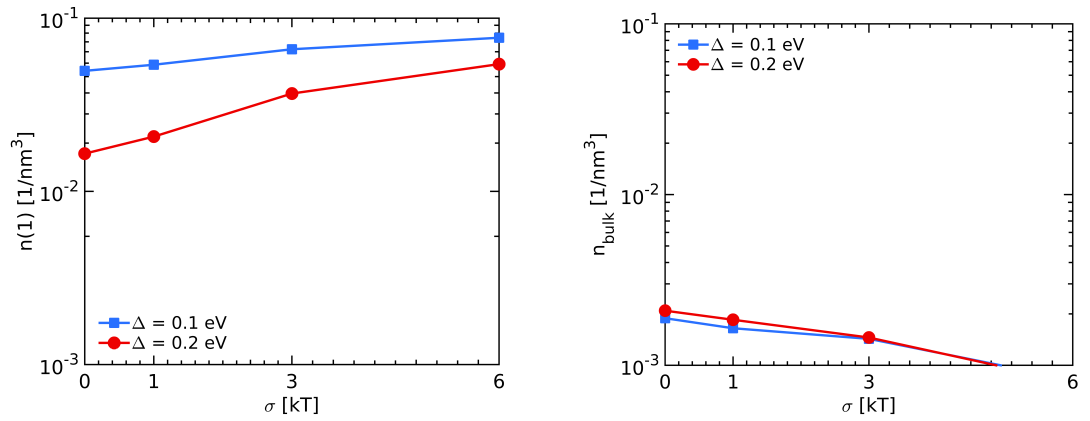
(a) Charge carrier density in the first layer as a function of the disorder σ.

(b) Average charge carrier density in the bulk as a function of the disorder σ.

Figure 6.14: Charge carrier density in the first layer and average charge-carrier density in the bulk as a function of the disorder σ for the applied field $F_{ext} = 1 \times 10^{-1}$ V nm^{-1} for the two lowest barriers. Closed symbols represent the points where simulations were done. The lines serve as guide to the eye.

Net current in SCLC   In Figure 6.15 we show the preferred hops (i.e. $\Delta E_{ij} < 0$) in steady-state when the Fermi level is above or close to the intrinsic energy level in the first bulk layer as it is the case for the 0.1 and 0.2 eV barrier. Particles will hop from the electrode into the bulk (b), from sites above the Fermi energy either back to the electrode (a) or (c) into the bulk, and (d) from sites below the Fermi level into the bulk.
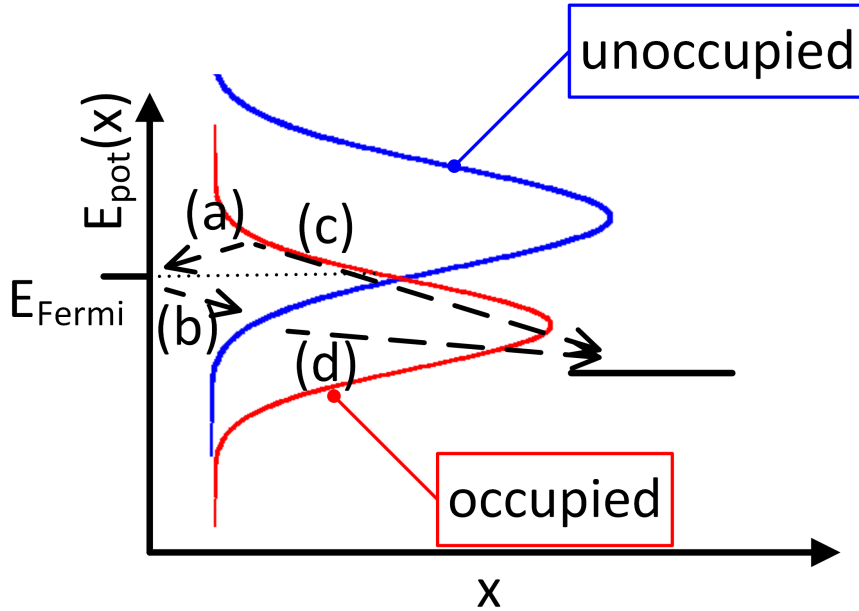

Figure 6.15: Schematic picture of the preferred hops (i.e. $\Delta E_{ij} < 0$) in steady state when the Fermi level is above or close to the intrinsic energy level in the first bulk layer. The hops are: (a) hops from occupied sites to the electrode, (b) hops from the electrode into unoccupied sites below the Fermi energy, (c) hops from above and (d) below the Fermi level into the bulk.

By making the following simplifications, we try to rationalize the steady-state behaviour for the 0.1 eV barrier at $F_{ext} = 1 \times 10^{-1}\ \mathrm{V\,nm^{-1}}$ for a disorder parameter $\sigma = 3\,k_B \cdot T$ which we believe to be resonant transport:

1. We look at our system in a one-dimensional picture, i.e., we only consider hops in x-direction.

2. We only consider nearest neighbour hops.

3. We only consider hops down in energy (i.e. $\Delta E_{ij} < 0$).

4. As these hops occur at equal likelihood, occupation is only determined by the filling of each layer and its mean energy.

In the case of the $\Delta = 0.1$ eV barrier, the filling of the first layer is 0.07 particles per site, i.e., 7% of the metal layer in steady-state (cf. Figure 6.14a). At that degree of filling only a small fraction of unoccupied sites below the Fermi energy is left (cf. blue bars with energy smaller than E_F in Figure 6.16). Following our previous simplifications, this number must be equal to the number of particles in the first layer above the mean energy of the second layer plus all remaining particles in the bulk, that have a neighbouring site accessible by a downward hop, i.e., $\Delta E_{ij} < 0$.

Let us assume, that an electron from the electrode hops into a first-layer site below the Fermi energy ((b) in Figure 6.15). Now, one of the following events will happen (if we disregard hopping events in the bulk): (1) an electron was lifted in energy due to that event (b), such that that electron, or any other electron above the Fermi energy will, with equal likelihood, (a), hop back to the electrode or, (c), into the bulk. Due to our assumptions events (a) and (c) will compensate each other and, therefore, do not contribute to the net current. However, (2) the electron from event (b) or any other electron below the Fermi energy will, (d), hop into the bulk, contributing to the net current.

Hence, with the simplifications above, we see that in steady-state conditions only events (b) and (d) contribute to the net current.
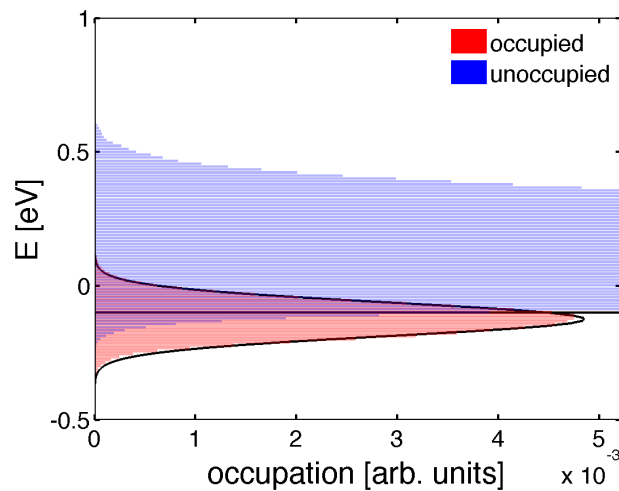
Figure 6.16: Energy distribution of occupied (red) and unoccupied (blue) sites in the first layer for the 0.1 eV barrier. The disorder is $3\,k_B \cdot T$ and the external field $F_{ext} = 1 \times 10^{-1}$ V nm^{-1}. Occupied sites are marked in red, unoccupied sites are marked in blue. The zero point of the energy is the transport level. The axes limits ware adopted, such that the energy distribution of the occupied sites can be seen. The experiment was only done for a single morphology until converged.

6.2 Investigation of the carrier densities and resulting potential

We start by plotting the charge-carrier density of the different simulations. We will pay particular attention, whether the spatially averaged charge-carrier density in through the bulk deviates strongly. This deviation will also be discussed in terms of the related current density and the electrostatic potential we calculate from the charge-carrier density. It will be shown, that latter can only be determined within large error bounds in Chapter 6.2.2.

6.2.1 Charge-Carrier Densities

Figure 6.17 and 6.18 show the layer averaged charge-carrier densities $n(x)$ of all simulations as a function of the distance from the electrode x. All charge-carrier densities are additionally averaged over the same eight different morphologies used for the simulations (except for the $0\,k_B \cdot T$ disorder case). Each sub-figure shows the charge-carrier densities for the three fields used in the simulations, one disorder and one barrier. Figure 6.17a to Figure 6.17d show the charge-carrier density for the $\Delta = 0.1\,eV$ barrier. The disorder is increasing from left to right and top to bottom. The remaining figures are sorted following the same scheme.

We note, that the cut-off radius artefact described in Chapter 4.5.2, was present also for the highest fields at the two lowest barriers of $\Delta = 0.1\,eV$ and $\Delta = 0.2\,eV$ and highest disorder. We therefore had to repeat these experiments with a higher cut-off radius and a shorter device as described in Chapter 4.5.2 (cf. Figure 6.17d and Figure 6.17h).
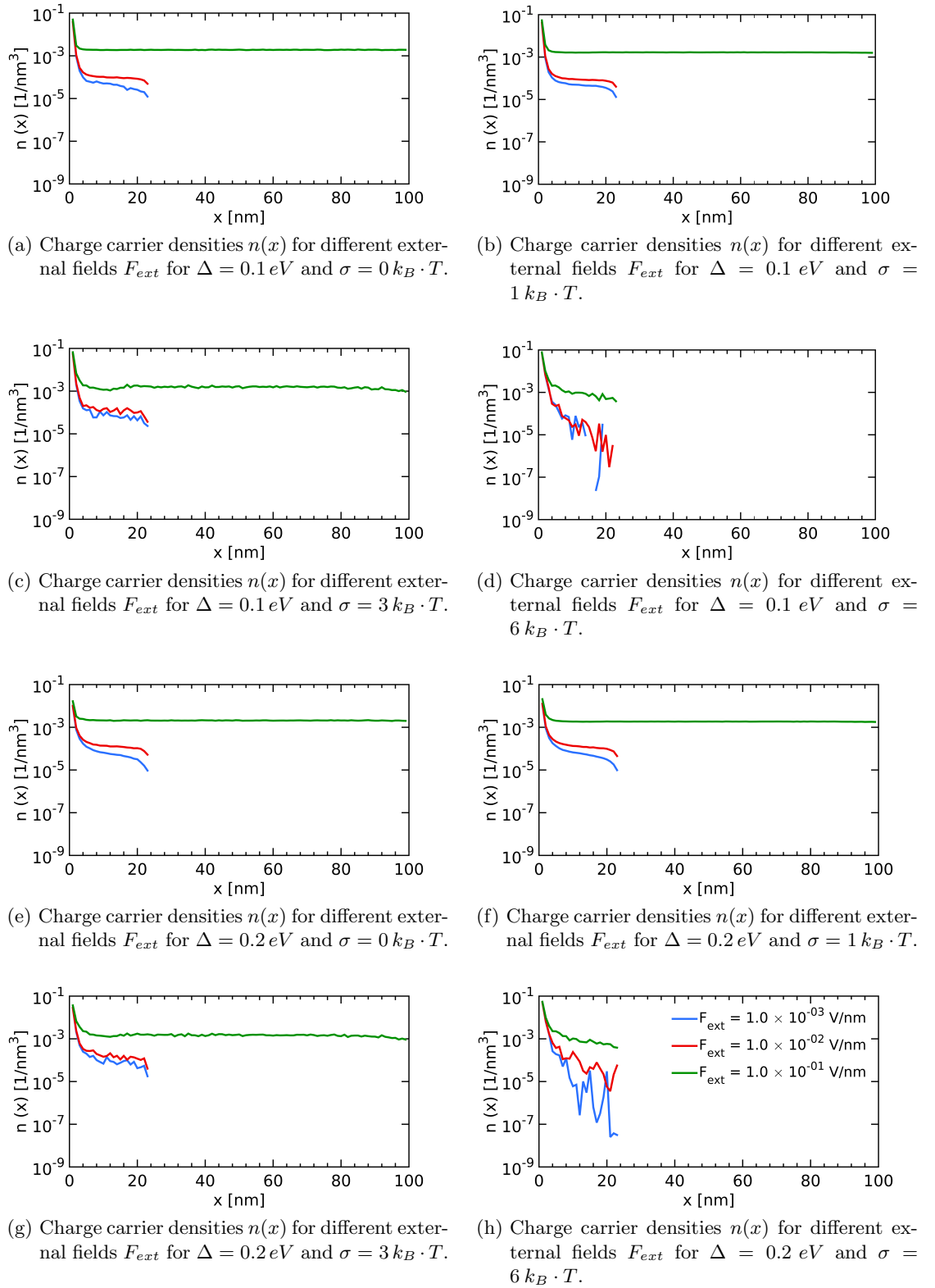
(a) Charge carrier densities $n(x)$ for different external fields F_{ext} for $\Delta = 0.1\,eV$ and $\sigma = 0\,k_B \cdot T$.

(b) Charge carrier densities $n(x)$ for different external fields F_{ext} for $\Delta = 0.1\,eV$ and $\sigma = 1\,k_B \cdot T$.

(c) Charge carrier densities $n(x)$ for different external fields F_{ext} for $\Delta = 0.1\,eV$ and $\sigma = 3\,k_B \cdot T$.

(d) Charge carrier densities $n(x)$ for different external fields F_{ext} for $\Delta = 0.1\,eV$ and $\sigma = 6\,k_B \cdot T$.

(e) Charge carrier densities $n(x)$ for different external fields F_{ext} for $\Delta = 0.2\,eV$ and $\sigma = 0\,k_B \cdot T$.

(f) Charge carrier densities $n(x)$ for different external fields F_{ext} for $\Delta = 0.2\,eV$ and $\sigma = 1\,k_B \cdot T$.

(g) Charge carrier densities $n(x)$ for different external fields F_{ext} for $\Delta = 0.2\,eV$ and $\sigma = 3\,k_B \cdot T$.

(h) Charge carrier densities $n(x)$ for different external fields F_{ext} for $\Delta = 0.2\,eV$ and $\sigma = 6\,k_B \cdot T$.

Figure 6.17: Charge carrier densities $n(x)$ as a function of the distance from the electrode x, where the electrode is placed at $x = 0$ for different external fields F_{ext} and different device lengths (25 and 101 nm). Figures 6.17a to 6.17d show $n(x)$ for the $\Delta = 0.1\,eV$ barrier and Figures 6.17e to 6.17h show $n(x)$ for the $\Delta = 0.2\,eV$ barrier

We observe three properties. (1) There is always a good convergence of the charge-carrier density (i.e. only small variations of $n(x)$ between different x) at all disorders for the highest field of $F_{ext} = 1 \times 10^{-1}$ V nm^{-1}. (2) There is a continuous decrease of $n(x)$ at the end of the device for the two lower fields and a disorder below $3\,k_B \cdot T$. (3) With increasing disorder the variations of the charge-carrier density increase tremendously and reach two decades for $6\,k_B \cdot T$ disorder.

The good convergence at the highest field is due to the high field, where (a) the highest potential energy lies in the first layer (cf. Figure 6.4). Then, all remaining sites have a decreasing energy with increasing distance from the interface, a condition that promotes the transport of the charge-carriers. Secondly, (b) at an external field of $F_{ext} = 1 \times 10^{-1}$ V nm^{-1} the energy drops by 100 meV from site to site soon after the first layer. This lifts the energy of deep traps, e.g., at a high disorder of 150 meV ($6\,k_B \cdot T$) the traps are approximately lowered by $150 - 100 = 50 meV$. Both leads to faster particles, which also leads to a homogeneous distribution in the x-direction.

There is a continuous decrease in the charge-carrier density $n(x)$ at the end of the bulk, which can be seen e.g. in Figure 6.17a starting at a position of approximately 20 nm for the field of $F_{ext} = 1 \times 10^{-2}$ V nm^{-1} and earlier for the field of $F_{ext} = 1 \times 10^{-3}$ V nm^{-1}. The reason for this observation is as follows: If we imagine the bulk to be extended, the charge-carrier density far away from the metal contact would be homogeneous, due to the Coulomb-Coulomb-repulsion of the particles in the bulk. However, if we now remove a charge from a system of finite size also its repulsive potential would vanish. Then, an effectively attractive Coulomb potential, centered at the original position of the particle is formed.
This results in an attractive force at the end of the device ($x = L$), such that particles get extracted faster. This translates into a reduced charge-carrier density close to where charges are extracted. However, the decrease in the charge-carrier density is rather small. The highest fluctuation due to that effect is observed for $0\,k_B \cdot T$ disorder (we neglect the $6\,k_B \cdot T$ disorder case for this discussion, as the deviation in that case is mainly due to the disorder), a barrier of 0.1 eV and the field $F_{ext} = 1 \times 10^{-2}$ in Figure 6.17a. There, the charge-carrier density drops from approximately 1×10^{-4} nm^{-3} to 5×10^{-5} nm^{-3}. This is equal to a drop from 0.26 to 0.16 particles, which we consider negligible for the current density j. For the calculation of the potential we bypass this reduction by calculating the average charge-carrier density between the eight and the 20th layer and extrapolate to 100 nm if the simulation was done with a 25 nm set-up.

We already saw in Chapter 6.1.1, that the current density at high disorder has a huge uncertainty. The reason for this can be seen in Figures 6.17 and 6.18, where the charge-carrier density fluctuates enormously for the $6\,k_B \cdot T$ disorder, although having been averaged over eight morphologies. We should, therefore, discuss results generated with high disorder and low fields with great care. This is especially critical when calculating the electrostatic potential, and from that the voltage drop over the device, as described in the following chapter.
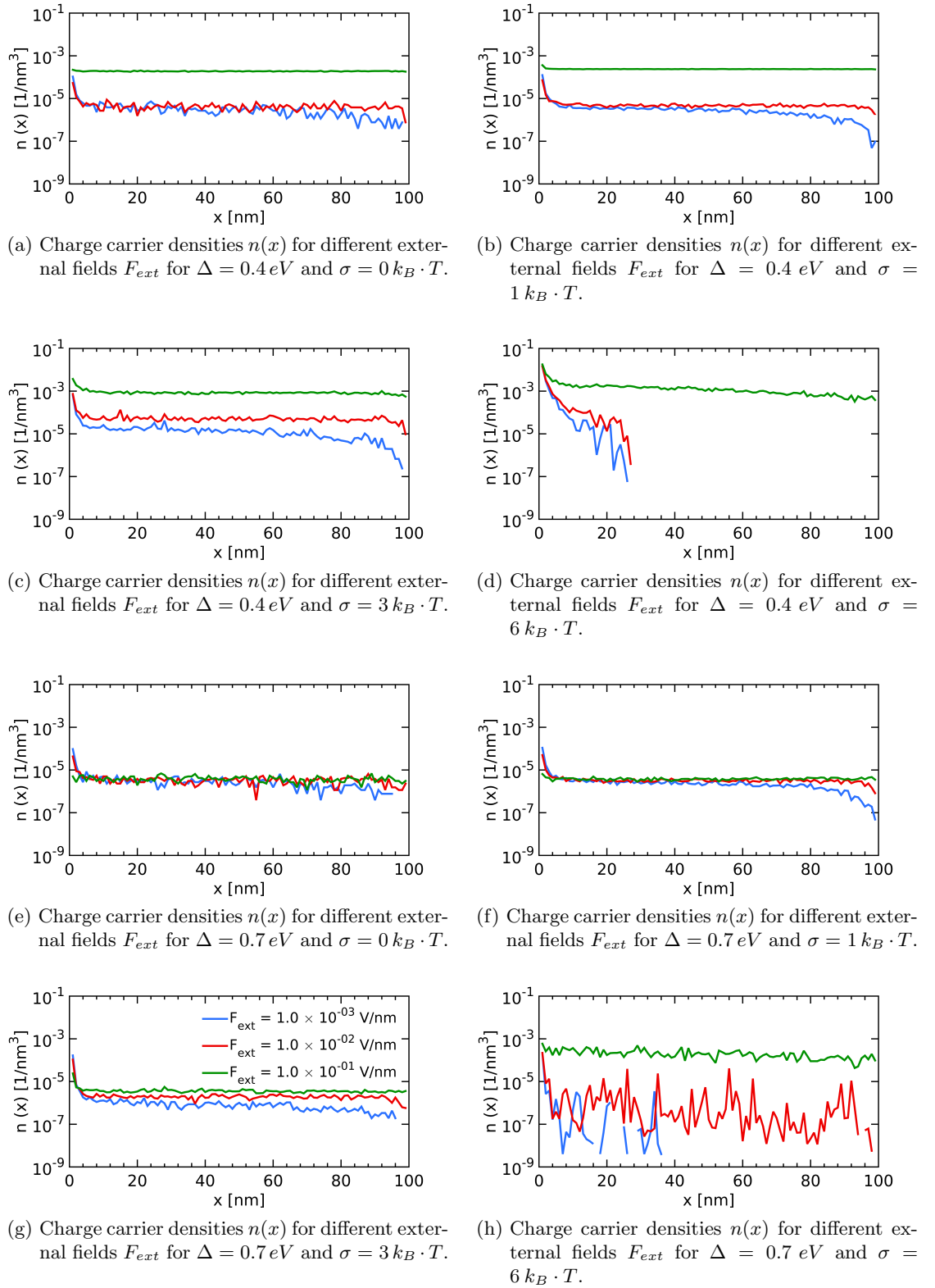
(a) Charge carrier densities $n(x)$ for different external fields F_{ext} for $\Delta = 0.4\,eV$ and $\sigma = 0\,k_B \cdot T$.

(b) Charge carrier densities $n(x)$ for different external fields F_{ext} for $\Delta = 0.4\,eV$ and $\sigma = 1\,k_B \cdot T$.

(c) Charge carrier densities $n(x)$ for different external fields F_{ext} for $\Delta = 0.4\,eV$ and $\sigma = 3\,k_B \cdot T$.

(d) Charge carrier densities $n(x)$ for different external fields F_{ext} for $\Delta = 0.4\,eV$ and $\sigma = 6\,k_B \cdot T$.

(e) Charge carrier densities $n(x)$ for different external fields F_{ext} for $\Delta = 0.7\,eV$ and $\sigma = 0\,k_B \cdot T$.

(f) Charge carrier densities $n(x)$ for different external fields F_{ext} for $\Delta = 0.7\,eV$ and $\sigma = 1\,k_B \cdot T$.

(g) Charge carrier densities $n(x)$ for different external fields F_{ext} for $\Delta = 0.7\,eV$ and $\sigma = 3\,k_B \cdot T$.

(h) Charge carrier densities $n(x)$ for different external fields F_{ext} for $\Delta = 0.7\,eV$ and $\sigma = 6\,k_B \cdot T$.

Figure 6.18: Charge carrier densities $n(x)$ as a function of the distance from the electrode x, where the electrode is placed at $x = 0$ for different external fields F_{ext} and different device lengths (25 and 101 nm). Figures 6.18a to 6.18d show $n(x)$ for the $\Delta = 0.4\,eV$ barrier and Figures 6.18e to 6.18h show $n(x)$ for the $\Delta = 0.7\,eV$ barrier
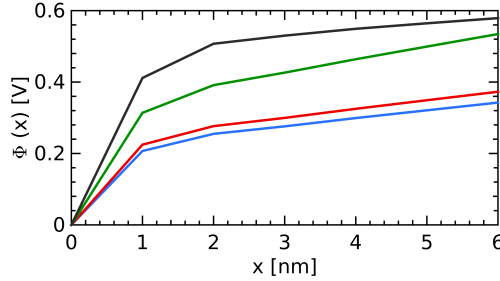
6.2.2 Electrostatic Potential

The electrostatic potential $\Phi(x)$ is determined as described in Chapter 4.4. We solve the one-dimensional Poisson-equation $\dfrac{\mathrm{d}^2\Phi(x)}{\mathrm{d}x^2} = -\dfrac{\rho(x)}{\epsilon}$ by integrating the layer and morphology averaged charge-carrier density (except for the $0\,k_B \cdot T$ disorder case, otherwise from eight different morphologies) twice by using splines.

Figure 6.19 and 6.20 show the electrostatic potential $\Phi(x)$ of all simulations as a function of the distance from the electrode x. As the charge-carrier density varies most in the first layers of the device, we have drawn $\Phi(x)$ only up to a distance of 6 nm. Each sub-figure shows $\Phi(x)$ for the four disorder values σ used in the simulations, one field value and one barrier. The value of the field is increasing from top to bottom, and the barrier value from left to right. I.e., Figure 6.19a, Figure 6.19c, and Figure 6.19e show $\Phi(x)$ for the $\Delta = 0.1\,eV$ barrier with increasing value of the field. The remaining figures are sorted according to the same scheme.

In the sub-figures of Figure 6.19, where we depict $\Phi(x)$ for the low barrier values Δ of 0.1 and 0.2 eV, we observe a parabolic curve, which is characteristic for space-charge limited current (SCLC), in accordance with our findings.

In the sub-figures of Figure 6.20, we depict $\Phi(x)$ for the barrier values Δ of 0.4 and 0.7 eV. For the highest barrier value of 0.7 eV, we see, except for the highest disorder value, a constant slope, which indicates a vanishing carrier density. This is again in accordance with our simulations, as these few carriers are mostly provided by thermionic emission, i.e., a very inefficient process at $\Delta = 0.7$ eV. As discussed in Chapter 6.1.1, at the barrier value Δ of 0.4 eV, we observe a cross-over between the thermionic emission, supported by the proximity effect, and SCLC as a function of the disorder. For all fields, depicted in Figure 6.20a, Figure 6.20c, and Figure 6.20e, it can be clearly observed, that $\Phi(x)$ turns from a constant slope into a parabolic behaviour with increasing disorder parameter σ, indicating a transition into a SCLC behaviour.

For all cases, where we switched to a shorter device, the average charge-carrier density between the eighth and 10th layer was calculated and then extrapolated to 100nm in order to estimate $\Phi(x)$ for the same device length.
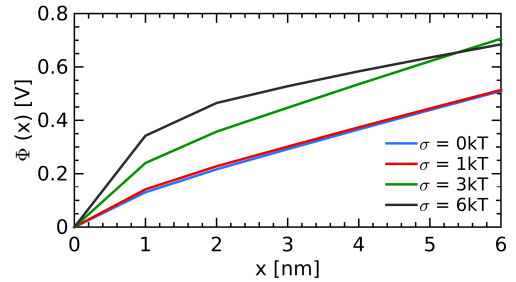
(a) Electrostatic potential $\Phi(x)$ for different disorder values σ for $\Delta = 0.1\,eV$ and $F_{ext} = 1 \times 10^{-3}$ V nm^{-1}.
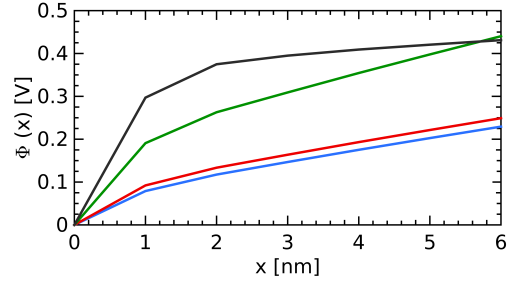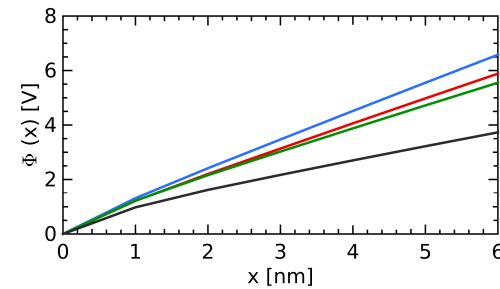
(b) Electrostatic potential $\Phi(x)$ for different disorder values σ for $\Delta = 0.2\,eV$ and $F_{ext} = 1 \times 10^{-3}$ V nm^{-1}.
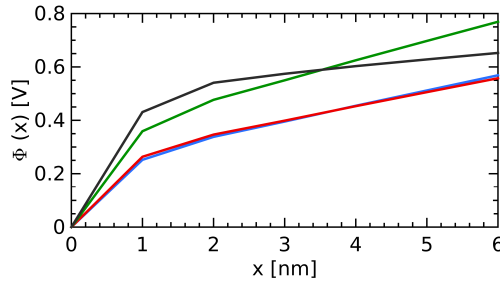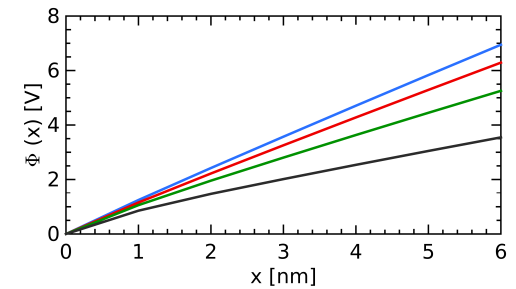
(c) Electrostatic potential $\Phi(x)$ for different disorder values σ for $\Delta = 0.1eV$ and $F_{ext} = 1 \times 10^{-2}$ V nm^{-1}.

(d) Electrostatic potential $\Phi(x)$ for different disorder values σ for $\Delta = 0.2\,eV$ and $F_{ext} = 1 \times 10^{-2}$ V nm^{-1}.

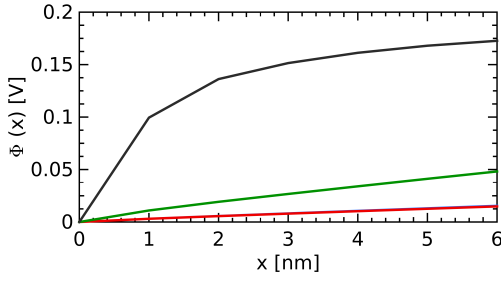(e) Electrostatic potential $\Phi(x)$ for different disorder values σ for $\Delta = 0.1eV$ and $F_{ext} = 1 \times 10^{-1}$ V nm^{-1}.

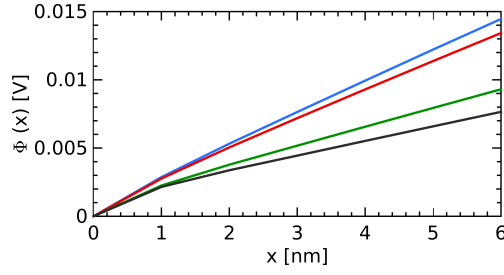(f) Electrostatic potential $\Phi(x)$ for different disorder values σ for $\Delta = 0.2eV$ and $F_{ext} = 1 \times 10^{-1}$ V nm^{-1}.

Figure 6.19: Electrostatic potential $\Phi(x)$ as a function of the distance from the electrode x, where the electrode is placed at $x = 0$ for different disorder values σ. Figure 6.19a, Figure 6.19c, and Figure 6.19e show $\Phi(x)$ for the $\Delta = 0.1\,eV$ barrier and Figure 6.19b, Figure 6.19d, and Figure 6.19f show $\Phi(x)$ for the $\Delta = 0.2\,eV$ barrier.

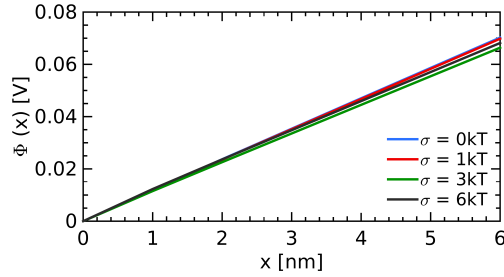(a) Electrostatic potential $\Phi(x)$ for different disorder values σ for $\Delta = 0.4\ eV$ and $F_{ext} = 1 \times 10^{-3}$ V nm^{-1}.

(b) Electrostatic potential $\Phi(x)$ for different disorder values σ for $\Delta = 0.7\ eV$ and $F_{ext} = 1 \times 10^{-3}$ V nm^{-1}.
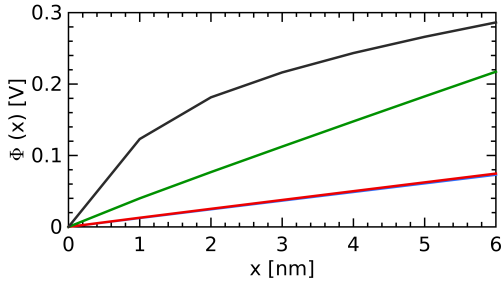
(c) Electrostatic potential $\Phi(x)$ for different disorder values σ for $\Delta = 0.4eV$ and $F_{ext} = 1 \times 10^{-2}$ V nm^{-1}.
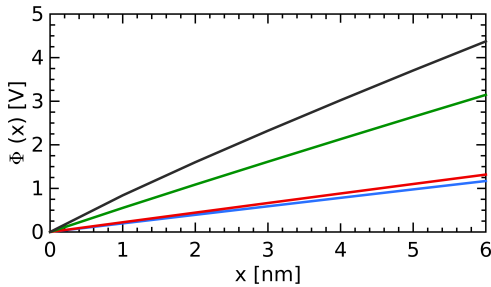
(d) Electrostatic potential $\Phi(x)$ for different disorder values σ for $\Delta = 0.7\ eV$ and $F_{ext} = 1 \times 10^{-2}$ V nm^{-1}.

(e) Electrostatic potential $\Phi(x)$ for different disorder values σ for $\Delta = 0.4eV$ and $F_{ext} = 1 \times 10^{-1}$ V nm^{-1}.

(f) Electrostatic potential $\Phi(x)$ for different disorder values σ for $\Delta = 0.7eV$ and $F_{ext} = 1 \times 10^{-1}$ V nm^{-1}.
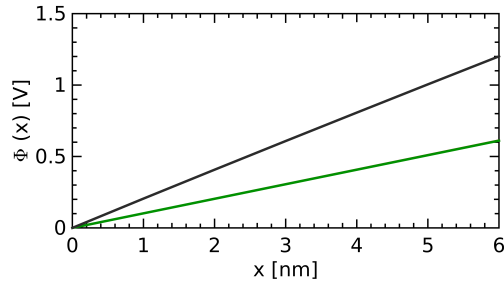
Figure 6.20: Electrostatic potential $\Phi(x)$ as a function of the distance from the electrode x, where the electrode is placed at $x = 0$ for different disorder values σ. Figure 6.20a, Figure 6.20c, and Figure 6.20e show $\Phi(x)$ for the $\Delta = 0.4\ eV$ barrier and Figure 6.20b, Figure 6.20d, and Figure 6.20f show $\Phi(x)$ for the $\Delta = 0.7\ eV$ barrier.

As we have seen in in Chapter 6.2.1, the charge-carrier density fluctuates greatly for the $6\ k_B \cdot T$ disorder. In those cases, we expect the uncertainty of $\Phi(x)$ to reach large values.

We try to estimate the uncertainty of the voltage calculation, by considering four test points. These are inspired by the simulations of Chapter 5.4, where we tried to compare against the work of Ref. [3] and saw large variations from the reference publication.

We calculate $\Phi(x)$ by fitting a second order spline to the charge-carrier density of the N

layers as given by Equation 6.1:

$$n(x) = \sum_{i=1}^{N-1} P_i(x) = \sum_{i=1}^{N-1} [a_i x^2 + b_i x^1 + c_i x^0] \cdot 1_{(x_i \leq x < x_{i+1})}. \qquad (6.1)$$

and then integrating twice to obtain the electrostatic potential as described in Chapter 4.4.

It is difficult to calculate the numerical error by propagation of uncertainty, as the charge-carrier density is integrated twice and influencing the integration constant of the next polynomial. Thus, we attempt the following estimation: Each layer averaged charge-carrier density corresponds also an average over eight morphologies (for $\sigma > 0$). Therefore, we can calculate a sample variance following Equation 4.8 for each $n(x)$. For the extrapolation of the charge-carrier density, we simply take the largest sample variance of the charge-carrier densities between layer eight and 20. We now calculate a lower and an upper bound electrostatic potential by adding up the maximum sample variance from its mean value $n(x)$.

The results for the test points of the 6 $k_B \cdot T$ disorder are shown in Figure 6.21. We first investigate the uncertainty of the voltage drop, i.e., of $\Phi(x = L)$. It can be seen, that the uncertainty increases with increasing field F_{ext} and decreasing barrier value Δ. Figure 6.21a shows, that for the highest barrier of 0.7 eV and the lowest external field $F_{ext} = 1 \times 10^{-3}$ V nm^{-1}, the voltage drop of 103 mV only varies by 5 mV at most, which corresponds to an uncertainty of 5%. At the medium field of $F_{ext} = 1 \times 10^{-2}$ V nm^{-1} and a low barrier of 0.2 eV the uncertainty of the voltage drop is already 10%. The highest uncertainty of more than 25% is observed at the lowest barrier and the highest field, as shown in Figure 6.21d.

In Figure 6.22, we now investigate the uncertainty of the electrostatic potential in the first layer, i.e., of $\Phi(x = 1nm)$, by plotting $\Phi(x)$ and its uncertainty for the same test points only until a distance x of 1 nm from the electrode.

Only at the 1×10^{-2} V nm^{-1} field and the 0.2 eV barrier (Figure 6.22b) the uncertainty is 10%. The remaining first layer potentials yield uncertainties of 20% (Figure 6.22a, Figure 6.22c, and Figure 6.22d).

For fields higher than $F_{ext} = 1 \times 10^{-2}$ V nm^{-1} the uncertainty of the voltage drop exhibits 10% for low fields, and a disorder of $6 k_B \cdot T$. The uncertainty of the electrostatic potential in the first layer $\Phi(x = 1nm)$ even exhibits 20% for the low barriers and the highest field.

The such determined uncertainty has two implications: A quantitative comparison to results obtained either considering a voltage, corresponding here to $\Phi(x = L)$, such as Ref. [3], or rely on macroscopic charge-carrier density and fields, such as Ref. [12], has to be considered with great care. Also, when calculating the electrochemical potential from $\Phi(x = 1nm)$ to compare against macroscopic models the profound uncertainty does not allow for a reliable comparison.
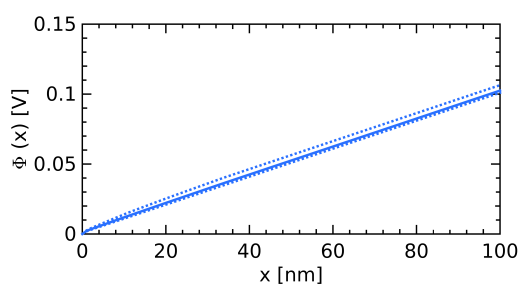
(a) Calculated potential $\Phi(x)$ (solid line) and its error bounds (dotted lines) at 6 $k_B \cdot T$ disorder, a 0.7 eV barrier and an external field $F_{ext} = 1 \times 10^{-3}$ V nm^{-1}.
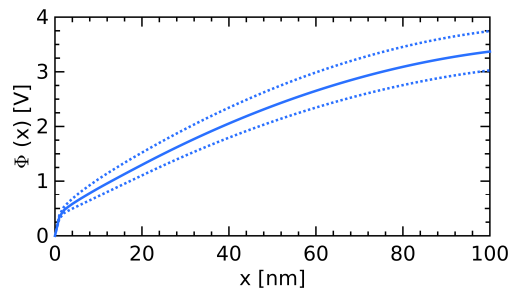
(b) Calculated potential $\Phi(x)$ (solid line) and its error bounds (dotted lines) at 6 $k_B \cdot T$ disorder, a 0.2 eV barrier and an external field $F_{ext} = 1 \times 10^{-2}$ V nm^{-1}.
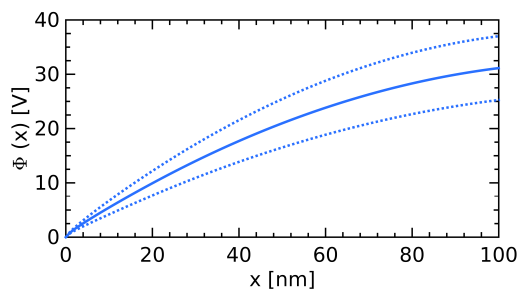
(c) Calculated potential $\Phi(x)$ (solid line) and its error bounds (dotted lines) at 6 $k_B \cdot T$ disorder, a 0.2 eV barrier and an external field $F_{ext} = 1 \times 10^{-1}$ V nm^{-1}.

(d) Calculated potential $\Phi(x)$ (solid line) and its error bounds (dotted lines) at 6 $k_B \cdot T$ disorder, a 0.1 eV barrier and an external field $F_{ext} = 1 \times 10^{-1}$ V nm^{-1}.

Figure 6.21: Estimate of the error (dotted lines) of the calculated potential (solid line) of the test points.
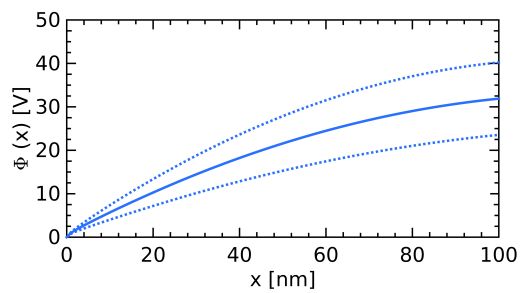
(a) Calculated potential $\Phi(x)$ (solid line) and its error bounds (dotted lines) at $6\ k_B \cdot T$ disorder, a 0.7 eV barrier and an external field $F_{ext} = 1 \times 10^{-3}$ V nm^{-1} plotted till the first layer.

(b) Calculated potential $\Phi(x)$ (solid line) and its error bounds (dotted lines) at $6\ k_B \cdot T$ disorder, a 0.2 eV barrier and an external field $F_{ext} = 1 \times 10^{-2}$ V nm^{-1} plotted till the first layer.

(c) Calculated potential $\Phi(x)$ (solid line) and its error bounds (dotted lines) at $6\ k_B \cdot T$ disorder, a 0.2 eV barrier and an external field $F_{ext} = 1 \times 10^{-1}$ V nm^{-1} plotted till the first layer.

(d) Calculated potential $\Phi(x)$ (solid line) and its error bounds (dotted lines) at $6\ k_B \cdot T$ disorder, a 0.1 eV barrier and an external field $F_{ext} = 1 \times 10^{-1}$ V nm^{-1} plotted till the first layer.
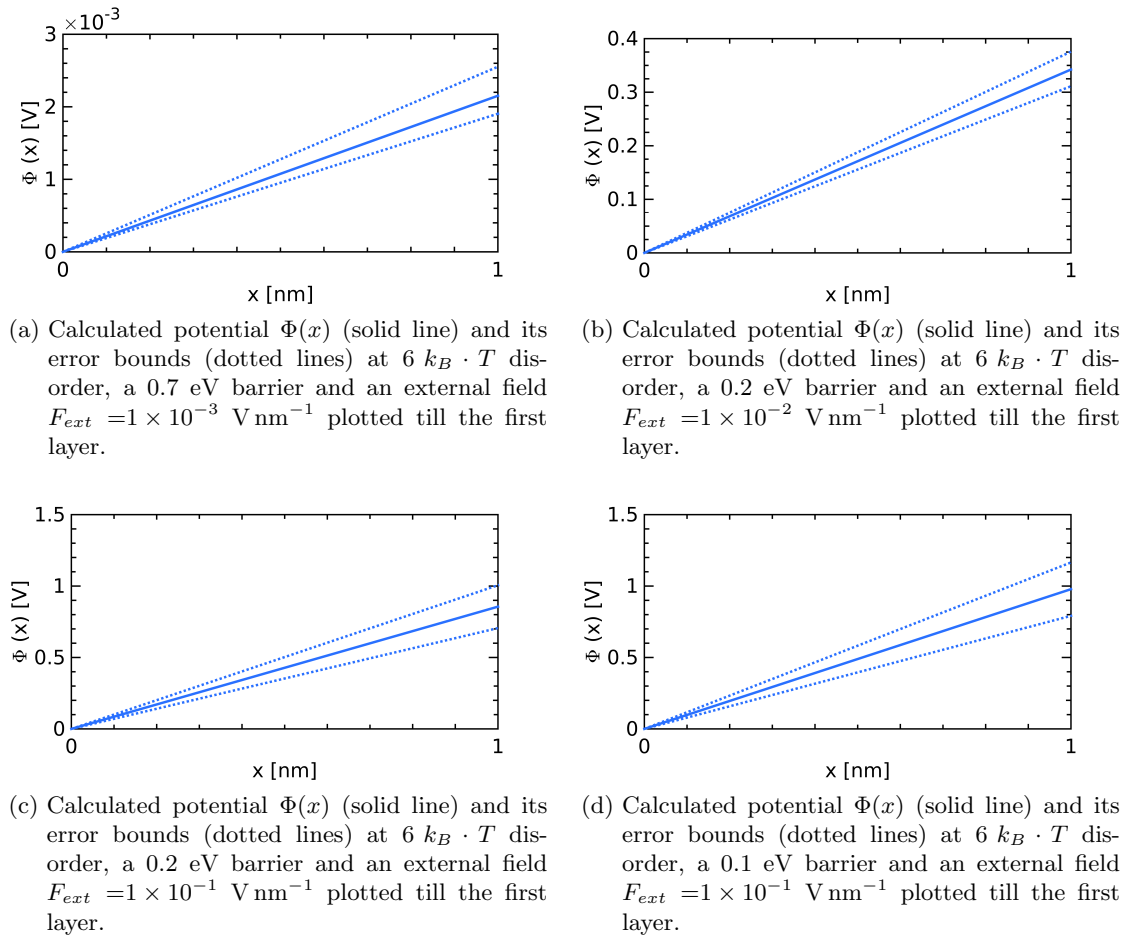
Figure 6.22: Estimate of the error (dotted lines) of the calculated potential (solid line) of the test points.

6.3 Comparison to present analytical models

In this chapter, we compare our results to selected works presented in Chapter 2.2. Neither Ref. [11] nor Ref. [1] could be taken for a qualitative analysis, as the former reference uses an unknown normalization factor and latter does not present a current density, which would be the only observable we could use for a comparison (cf. Chapter 4.4). We note, however, that our simulations using a $3\,k_B \cdot T$ disorder qualitatively agree with the 80 eV disorder $j - F$ curves shown in Ref. [11], where also the current densities of the 0.2 and 0.4 eV barrier values approach a space charge limited current (SCLC) for the field of 1×10^{-1} V nm^{-1}. Similar to our simulations, no SCLC is observed for the 0.7 eV barrier.

A comparison to Ref. [3] is problematic due to the high uncertainty in the voltage results (cf. Chapter 6.2.2) and the different experimental design. A proof of the validity of our model, where we checked the general trends of our model and Ref. [3] was, however, presented in Chapter 5.4. Also, a comparison to Ref. [2] is not possible, as that model focuses on the simulation of an OPV and the related effects, rather than on the process of injection.

The models that are left for a comparison are from Ref. [9], where one is provided with a closed equation with well defined parameters, and Ref. [12], where certain assumptions on some parameters have to be made, in order to compare against our KMC model.

In latter case, we tried to calculate the disorder from the total density of states and adopt the attempt frequency to match the $j - V$ characteristic from the reference. However, due to the high uncertainty of both, our current and especially voltage calculation, it was not possible to gain meaningful results for a comparison. We note, however, that we observed the same space charge limited current regime, that was reported in Ref. [12] for high external fields.

As a consequence, we restrict ourselves to the model of Scott and Malliaras for a quantitative comparison to a macroscopic model (cf. Chapter 6.3.3).

6.3.1 The model of Neumann et al.

The model of Neumann *et al.*, assumes that only charge carriers injected from the metal contribute to the current as the conduction band of the organic is taken to be far away from its valence band. This is in agreement with our model, which also only considers charges that are injected from the metal. Moreover, that model considers the effect of space-charges, which is also inherent in our model.

In contrast to our model, however, trapping due to disorder is not considered.

In order to be able to compare against the model of Ref. [12], we had to set up new simulations, to reach an agreement with the parameters of that reference publication and also cover the wide voltage- (i.e., field-) range depicted in that work. The current voltage characteristics that are used for comparison here, have been obtained by Kinetic Monte Carlo and the parameters as given in Table 6.1.

The values for ϵ_r, T and Δ are given in Ref. [12]. The attempt frequency ν_0 was adopted such that we obtain similar current densities as Ref. [12]. The overlap factor γ is the same as for our previous simulations.

To reproduce the $j - V$ curves given in Ref. [12], the field strengths F_{ext} corresponding to selected voltage values were estimated with $F_{ext} \approx V/L$, with $L = 100$ nm being the device length. These yielded values for F_{ext} of $1 \times 10^{-4}, 1 \times 10^{-3}$, $1 \times 10^{-2}, 1 \times 10^{-1}$, and 1 V nm^{-1}, for which the corresponding current densities j were determined.

To determine the value of the disorder parameter σ, we evaluated Equation 6.2, given

Table 6.1: Parameters used for the simulations to compare against Ref. [12].

$rate$	$Miller - Abrahams$
$size$	$101 (or\ 25) \times 51 \times 51$
a_{latt}	1.0 nm
ϵ	3
T	$300K$
ν_0	$6.76 \times 10^{17}\ s^{-1}$
γ	$10/a_{latt}$
σ	45 meV
Δ	$varied$
F_{ext}	$varied$

in that work, for different values of σ until we obtained a value of $N = 1$ nm^{-3} which corresponds to a value of 1×10^{21} cm^{-3}, given in Ref. [12]:

$$N = \int_{-\infty}^{\infty} g(\epsilon|0,\sigma) \exp\left(-\frac{\epsilon}{k_B T}\right) d\epsilon. \tag{6.2}$$

The calculations yielded a disorder parameter of $\sigma = 45$ meV. As we are interested in a qualitative comparison, and due to the high uncertainty of our voltage calculations, the simulations were only carried out for one morphology.

In Figure 6.23 the $j - V$ characteristics of Ref. [12] (Figure 6.23a) and our simulations (Figure 6.23b) are depicted.

As can be seen in Figure 6.23, the $j - V$ curves of our simulations yield the same slope as that of the 0 eV barrier of the reference (Figure 6.23a). Also, in our simulations, the $j - V$ characterstics perform transition into a SCLC regime for all barriers used for this comparison (i.e., $\Delta \leq 0.4$ eV) at large fields F_{ext}. In contrast to the reference, we already observe this transition for $20 - 40$ V, compared to approximately 100 V of the reference.

The regime at voltages below this transition voltages (i.e., injection limited regime) are difficult to compare, due to the high voltage and current density uncertainty. We can, however, observe that the current of the highest barrier (0.4 eV) is lower than the current density of the 0 eV barrier for the same voltage, in accordance with Ref. [12]. In contrast to Ref. [12], however, we do not observe a constant slope for the 0 eV barrier.

To investigate this in more detail, we plot the current density j against the applied electric field F_{ext} in Figure 6.24. Here, a vanishing barrier ($\Delta = 0\ eV$, square), j is undergoing a transition from a constant value at low fields to a linear rise of slope 2 at $F_{ext} = 1 \times 10^{-2}$ V nm^{-1}, which is indicating a space-charge-limited current. We believe the reason for the constant current density in the reference publication, as compared to the curve observed in our simulations, as well as the different voltage for a transition into SCLC to be as follows: The mobility in the reference is constant over all fields. In our simulations, and for real materials, however, the mobility depends on the external field F_{ext} and the disorder value σ. At low fields, the mobility will drop, and, as a result, also the current density will decrease, as observed in our simulations.
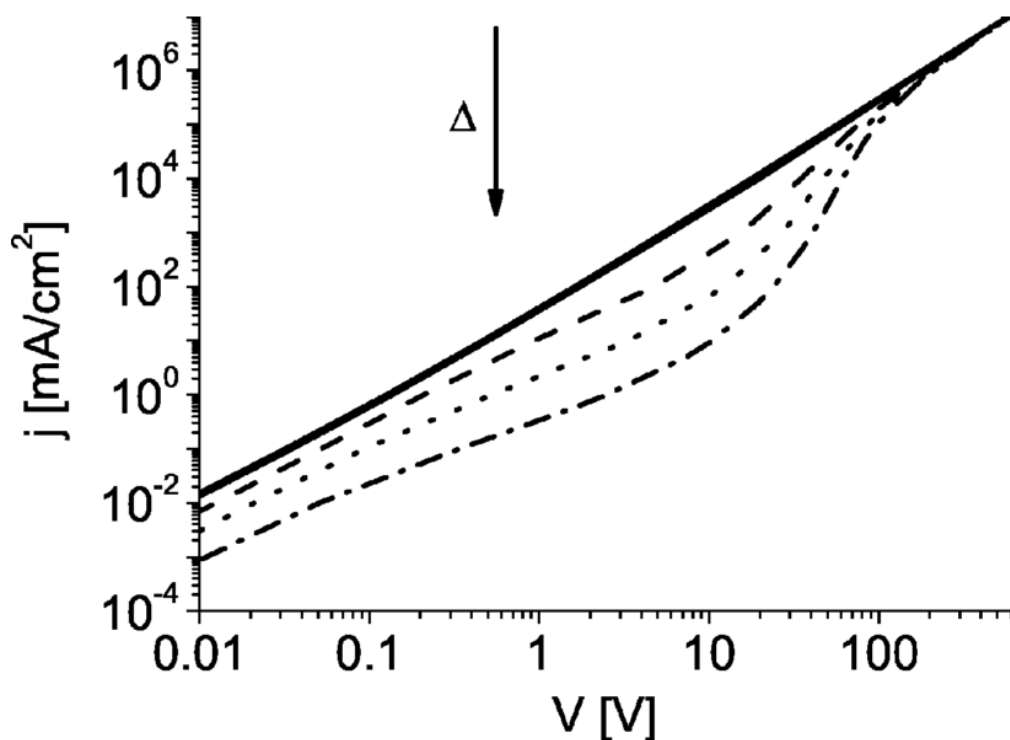
(a) $j-V$ characteristics for barrier heights Δ of 0, 0.2, 0.3, 0.35, and $0.4 eV$ of the model presented in Ref. [12]. Adopted from Ref. [12].
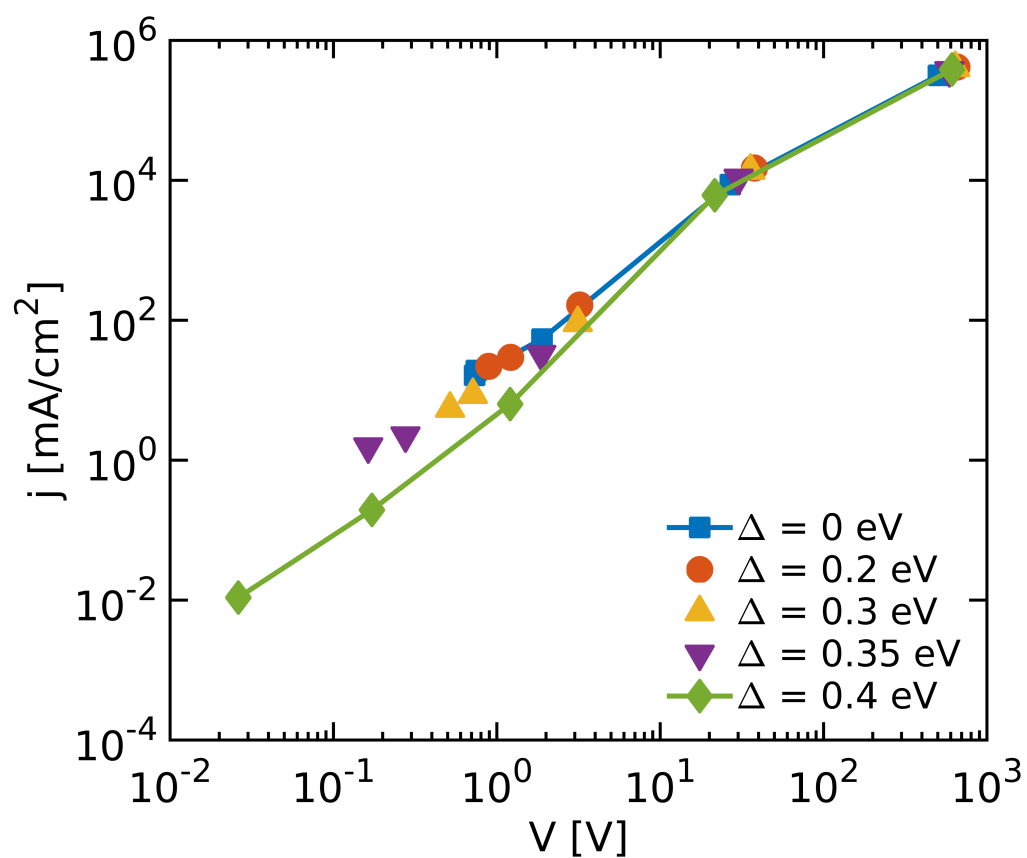
(b) $j-V$ characteristics of our simulations for barrier heights Δ of 0, 0.2, 0.3, 0.35, and $0.4\,eV$.

Figure 6.23: Comparison of the $j-V$ characteristics of Ref. [12] (Figure 6.23a) and our simulations (Figure 6.23b).
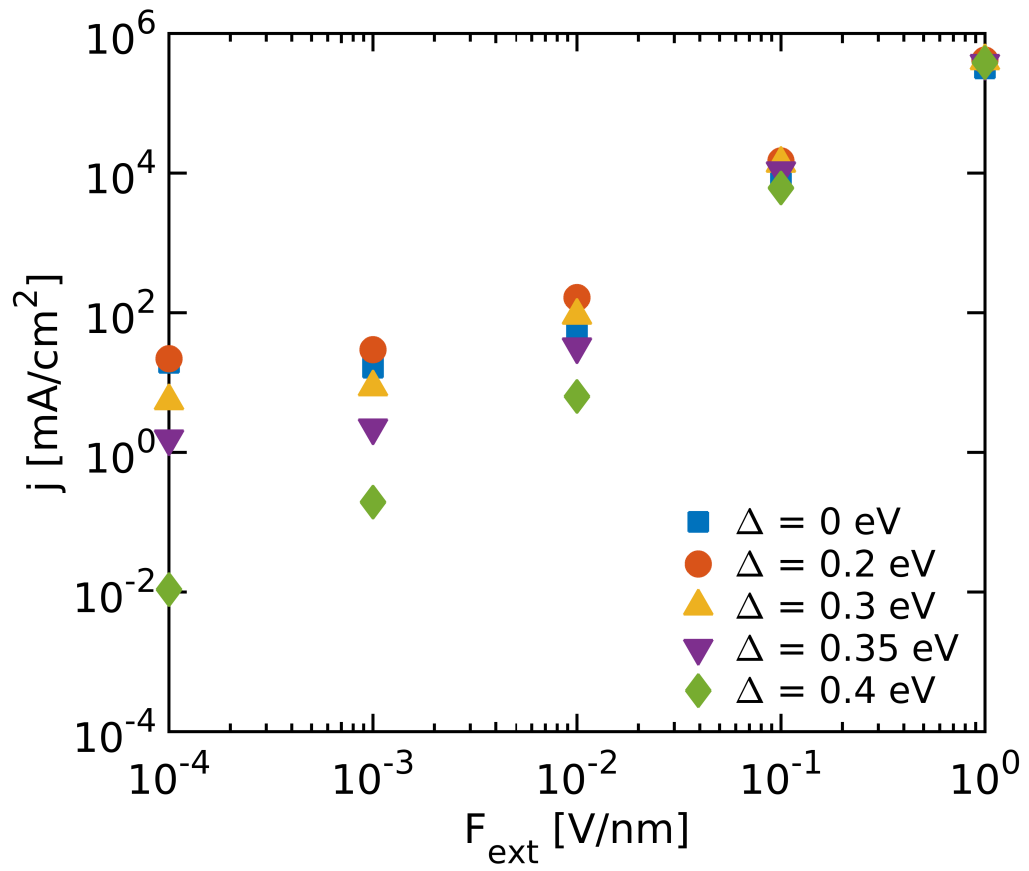
Figure 6.24: $j - F$ characteristics of our simulations for barrier heights Δ of 0, 0.2, 0.3, 0.35, and $0.4\,eV$.

6.3.2 The model of Arkhipov et al.

A comparison to the analytical curves of Ref. [11] and KMC-simulations by Ref. [1] are of high interest, as it is possible to see (1) how our model compares to an analytical approach based on similar assumptions as KMC and (2) in which way the consideration of Coulomb-Coulomb-interactions in our simulations changes the macroscopic behaviour. For a qualitative comparison to the work of Ref. [11], we chose $j - F$ characteristics of Ref. [11] (Figure 6.25a), which were simulated and analytically calculated for external fields ranging from 1×10^{-2} to 1 V nm^{-1}. The value for T is 300 K, as in our simulations. The disorder parameter σ is 80 meV in that work, which we can nicely compare to our simulations, where we used $\sigma = 3\, k_B \cdot T$, i.e., 75 meV. The overlap factor γ for these plots is not explicitly given. We assume, that the value of $\gamma = 5/a_{latt}$ is implied by Ref. [1] (Chapter 5.2) to which the subsequent analytical calculations refer to. This is equal to a value of $\gamma = 8.3$ nm^{-1} due to the lattice constant of $a_{latt} = 0.6$ nm used in Ref. [1]. This value is only slightly different to $\gamma = 10$ nm^{-1} used in our simulations. The relative permittivity $\epsilon_r = 3.5$ in the simulations of Ref. [1]. This value is the same as in our simulations.

Hence, the current densities only differ in ν_0. The attempt frequency ν_0 is a scaling factor, and causes an offset along the y-axis in the double logarithmic plot of Figure 6.25. We cannot, thus, compare the absolute value of j, but the relative distance between the different curves.

In Figure 6.25 the $j - F$ characteristics of Ref. [11] (Figure 6.25a) and our simulations (Figure 6.25b) are depicted.

When comparing the behaviour of the 0.2 and 0.4 eV curves, we can see, that the curves are closer together than the analytical curves of Figure 6.25a and even more than the reference curves from the simulations of Ref. [1]. This clearly indicates, that for such small barriers the accumulation of space charges due to the Coulomb-Coulomb-interactions leads to a lower current for a given field. This, in fact, implies that a space-charge limited current is formed at lower field strengths.

The current density of the 0.7 eV barrier is higher than in the reference simulations and the analytical curves. This increase in j as described in Chapter 6.1.1, is attributed to Coulomb-Coulomb-interactions that promote injection via the proximity effect.
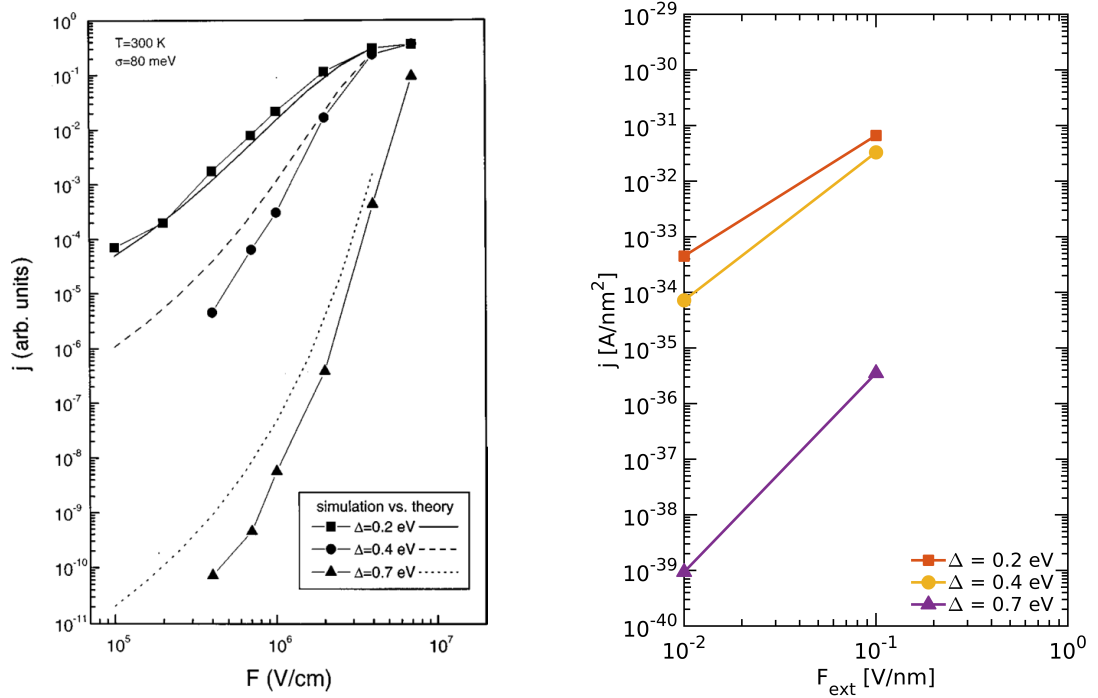
(a) $j - F$ characteristics for different barrier heights Δ for a disorder parameter $\sigma = 80$ meV of the analytical model (lines without symbols) and simulations (lines with symbols) presented in Ref. [11]. Adopted from Ref. [11].

(b) $j - F$ characteristics of our simulations for different barrier heights Δ for a disorder parameter $\sigma = 75$ meV. The lines serve as a guide to the eye.

Figure 6.25: Comparison of the $j - F$ characteristics of Ref. [11] (Figure 6.25a) and our simulations (Figure 6.25b).

6.3.3 The model of Scott and Malliaras

We start by describing how we determined the parameters for the current density equation suggested by Scott and Malliaras [9], followed by a $j - F$ plot to compare that model against our results. We conclude by discussing the deviations from our model and suggesting how the model of Scott and Malliaras could be extended for a better match with the predictions of our model.

In the model of Scott and Malliaras, as described in Chapter 2.2, the current density as a function of the applied field F_{ext} is given as:

$$ j_{SM} = 4\Psi(f)^2 N_0 e\mu F_{ext} \exp\left(-\frac{\Delta}{k_B T}\right) \exp\sqrt{f(F_{ext})}. $$

The barrier value Δ and the temperature T are taken from the KMC simulation parameters. Also, the constants e and k_B are given. The site density, N_0, is 1 nm^{-3} due to the lattice constant, a_{latt}, of our model being 1 nm. The mobility, μ, is determined from the trajectories of single charges in the bulk at specific fields and disorder and the parameters from our injection simulation. The reason for using a single, non-interacting charge for the determination of μ, is that the model of Scott and Malliaras only takes into account the interaction between a charge and its own image but not with any other charge. One could, however, calculate the surface charge-carrier density n_0 as given by Ref. [9] to calculate the bulk mobility of interacting charges. The values we obtained by that expression differed from the charge-carrier density of our simulations by orders of magnitude. Therefore, we decided to use simulations of non-interacting charges. Also, as assessed in Chapter 5.3, the mobilities vary only slightly for the bulk charge-carrier density as we saw already in Chapter 6.2.1 ($\langle n \rangle(x) < 1 \times 10^{-3}$ m^3) for disorder parameters $\sigma \leq 4\,k_B \cdot T$. In order to get a morphology independent mobility for a disorder $\sigma > 0$, μ is averaged over eight morphologies.

Nevertheless, the authors of Ref. [9] also suggest to incorporate the fact that mobilities are field-dependent. The field dependent function $f(F_{ext})$ is calculated by

$$ f(F_{ext}) = \frac{eF_{ext}r_c}{k_B T}, $$

where r_c is the Coulomb capture radius as given by Equation 2.9. The prefactor $\Psi(f)$ is given by

$$ \Psi(f) = f^{-1} + f^{-1/2} - f^{-1} \cdot \left(1 + 2f^{1/2}\right)^{1/2}. $$

In Figure 6.26, the current density j is plotted as a function of the externally applied field F_{ext} for different barriers Δ and disorders σ. The simulations by our model are marked with closed symbols. Solid lines represent the corresponding results calculated by the model of Scott and Malliaras.

As we saw in Chapter 6.1.2, for low barrier values ($\Delta \leq 0.2$ eV) we obtain the regime of SCLC. Here, the charge-carrier density in the bulk is mostly independent of the barrier and the current density is determined by the product of the charge-carrier density and the corresponding mobility. The charge-carrier density in the model of Scott and Malliaras is also barrier-dependent. However, there are no space charge effects taken into account in that model, which are expected to arise for low barrier values, as we have seen in Chapter 6.1.2 and Chapter 6.3.1. Therefore, we expect the model of Scott and Malliaras not to be in agreement with our model for low barrier values. The deviation from that model due to SCLC can be seen for all disorders in Figures 6.26a to 6.26d, where the curves of the 0.1 and the 0.2 eV barrier coincide in our simulations. The model of Scott and
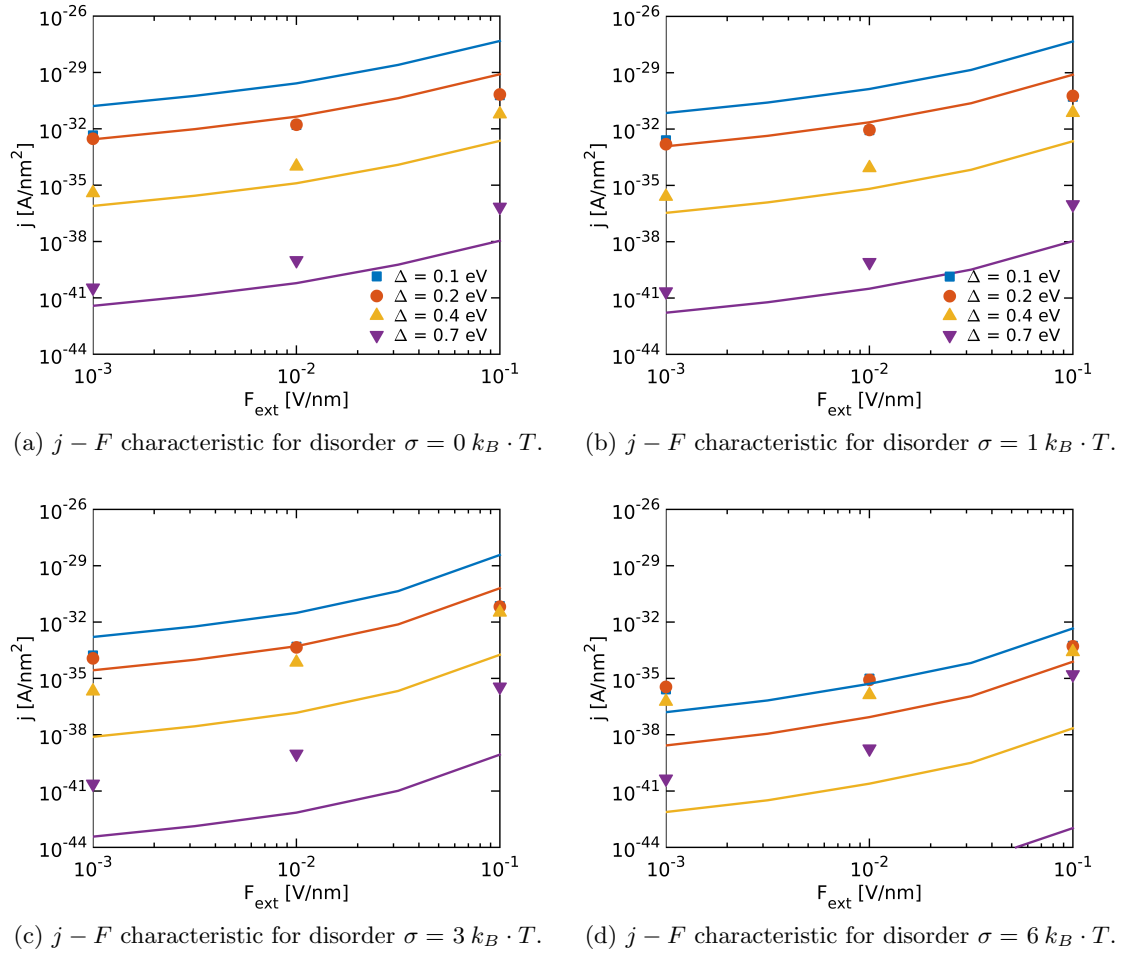
(a) $j - F$ characteristic for disorder $\sigma = 0\,k_B \cdot T$.

(b) $j - F$ characteristic for disorder $\sigma = 1\,k_B \cdot T$.

(c) $j - F$ characteristic for disorder $\sigma = 3\,k_B \cdot T$.

(d) $j - F$ characteristic for disorder $\sigma = 6\,k_B \cdot T$.

Figure 6.26: Current density j as a function of the externally applied field F_{ext} for different barriers Δ and disorders σ (increasing from left to right and top to bottom). Closed symbols represent the points of simulations with our KMC model. Lines of corresponding color show the corresponding results determined with the model of Scott and Malliaras as described in the text.

Malliaras (1) does not yield the SCLC-related saturation of the characteristic for high fields and (2) the match of the characteristics with the two low barrier values (SCLC). We will, therefore, continue our discussion for barrier values, where space charge effects play a minor role.

One would expect a good agreement of our model with that of Scott and Malliaras for low disorder ($\sigma \leq 1\,k_B \cdot T$) and sufficiently high barrier values ($\Delta \geq 0.4$ eV). Firstly, because the expected charge-carrier densities are small enough, such that its dependence on the mobility and space charges should be negligible. Secondly, the disorder-induced lowering of the effective barrier should be low. However, we can see in Figure 6.26a and 6.26b (triangles), that our data does not correspond to the model also in this case. We think that the reason for this is (1) the proximity effect as described in Chapter 6.1.1, which is not accounted for in a macroscopic model and (2) a lowering of the effective injection barrier due to disorder.

As a first step to comprehend the impact of the former effect, one could try to map the proximity effect on a factor accounting for a lowering of the effective barrier for the

$0\,k_B \cdot T$ disorder case. Then the current density j_{SM} would change to j'_{SM} as given by Equation 6.3, with a lowering energy contribution Δ_a:

$$j'_{SM} = j_{SM} \exp\left(\frac{\Delta_a}{k_B T}\right). \tag{6.3}$$

By simply equating the current density from our KMC model to that of Scott and Malliaras at $0\,k_B \cdot T$ disorder and 0.7 eV barrier value, we fit the parameter Δ_a to 54 meV. The resulting current densities for $\Delta \geq 0.4$ eV match nicely for the two low fields, as can be seen in Figure 6.27. For high fields, however, the proximity effect is stronger, as we saw in Chapter 6.1.1, which we did not account for in our simple approximation of Equation 6.4.
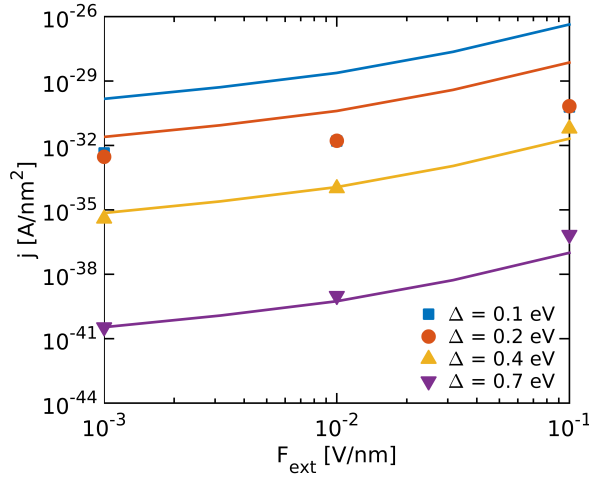

Figure 6.27: Current density j as a function of the externally applied field F_{ext} for different barriers Δ and $0\,k_B \cdot T$ disorder. Closed symbols represent the points of simulations with our KMC model. Lines of corresponding color show the corresponding results determined with the model of Scott and Malliaras, adopted by Equation 6.3, as described in the text.

For a disorder $\sigma > 0\,k_B \cdot T$, we expect paths to form below the barrier. This idea was also suggested by Burin and Ratner [27]; the associated barrier lowering is proportional to the disorder parameter σ and the square-root of the field. Here, we only consider the barrier lowering due to the disorder and adopt the current density of Scott and Malliaras to j'_{SM} as given by Equation 6.4:

$$j'_{SM} = j_{SM} \exp\left(\frac{b \cdot \sigma}{k_B T}\right). \tag{6.4}$$

Here, b is a fitting factor, that takes into account, that particles are able to hop onto sites with values below the effective barrier for a non-vanishing disorder. As the lowering of the effective barrier is supposed to be affected by the disorder, the induced barrier lowering is assumed to be $b \cdot \sigma$. Note that Equation 6.4 does not consider the proximity effect (cf. Equation 6.3).

Again, we equate the current density from our KMC model to that of Scott and Malliaras at $1\,k_B \cdot T$ disorder and 0.7 eV barrier value, and find that $b = 2.5$ yields a good agreement for all $j - F$ curves in Figure 6.28a. The resulting current densities for $\Delta = 0.7$ eV match nicely for all disorders, as can be seen in Figure 6.28. For the barrier of $\Delta = 0.4$ eV, however, the characteristics of model and simulation deviate with

increasing disorder. Presumably, this is due to an increasing charge-carrier accumulation that increases with disorder. Thus, the lowering of the barrier is much more pronounced than for the $\Delta = 0.7$ eV barrier. The effect of space-charges however, can not be treated that easily by an adoption of an effective injection barrier height.
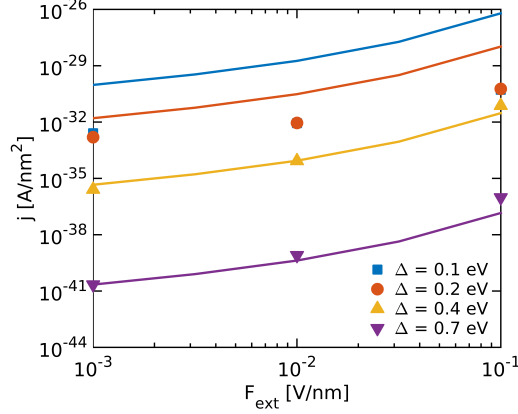
(a) $j - F$ characteristic for disorder $\sigma = 1\, k_B \cdot T$.
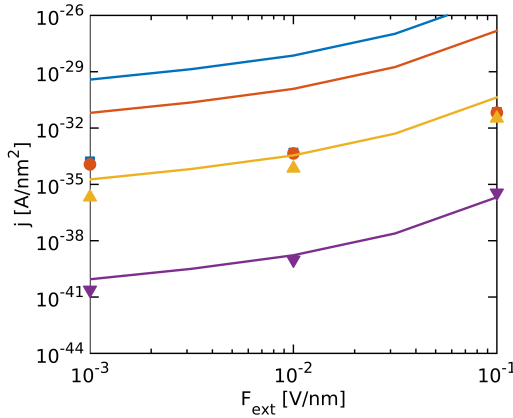
(b) $j - F$ characteristic for disorder $\sigma = 3\, k_B \cdot T$.
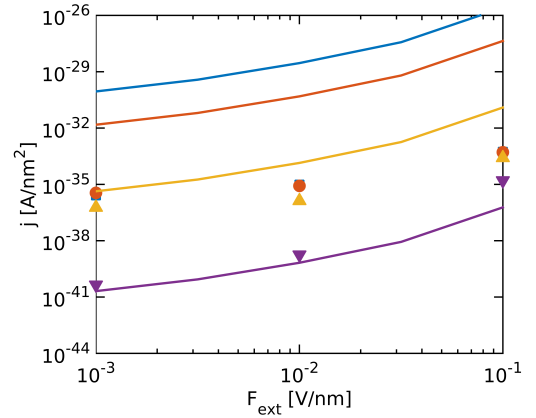
(c) $j - F$ characteristic for disorder $\sigma = 6\, k_B \cdot T$.

Figure 6.28: Current density j as a function of the externally applied field F_{ext} for different barriers Δ and disorders σ (increasing from left to right and top to bottom). Closed symbols represent the points of simulations with our KMC model. Lines of corresponding color show the corresponding results determined with the model of Scott and Malliaras, adopted by Equation 6.3, as described in the text.

We conclude that the model of Scott and Malliaras fails to describe the $j-F$ characteristics of low injection barriers correctly, where space-charges predominantly determine the behaviour. Our simulation results suggest, that the current density predicted by Scott and Malliaras requires an additional exponential factor, that corrects the effective injection barrier height for disorder and space-charge effects. To account for the proximity effect at vanishing disorder the barrier height is lowered by a constant value (Equation 6.3), whereas for non-vanishing disorder, the exponent is disorder-dependent (Equation 6.4), since sites below the effective barrier are available for transport. This works well for intermediate barriers ($\Delta \geq 0.4$ eV), until high disorder leads to charge accumulation at the interface, which promotes space-charge-limited current.

7 Conclusions and Outlook

Within this thesis, we developed a model for the charge injection from a metal electrode into a disordered organic semiconductor. We used the KMC method, because all relevant microscopic processes are intrinsically contained in the model and macroscopic observables can easily be obtained. In our approach, we go beyond the only present KMC implementation of injection, described in Ref. [1].

Our model simulates the injection of charges from a metal electrode into an organic semiconductor, discretized into cubes of edge length a_{latt} and a thickness of 25 nm and larger, as a function of a superimposed electric field F_{ext}. The density of states in the organic material is assumed to be Gaussian. All hopping rates are calculated with the Miller - Abrahams rate equation. For the sake of consistency, in the organic material and at the interface to the metal the same parameters we used. The model includes Coulomb-Coulomb-interactions between all particles and all images up to a cut-off radius r_c.

As the simulation framework was developed from scratch, we started with a set-up as simple as possible, and, then, increased the complexity of the simulation step by step. At each step, the results of the implementation were compared to references in order to notice errors in an early stage. Those comparisons were taken from Ref. [2], Ref. [1] and Ref. [18].

Finally, our model was compared to the results of Ref. [3], which is the only KMC reference, that directly includes all Coulomb-Coulomb-interactions. We observed the same trends. The small quantitative deviations found in some scenarios were shown to originate from the different set-up of our model system and a large uncertainty in our observables in both the current density and the voltage.

By determining the current density over a wide range of external fields, disorder values, and barrier values, we were able to identify two regimes of the disorder-dependent current density $j(\sigma)$. In both regimes, i.e., for all barrier values considered, there is a profound accumulation of charges at the metal-organic interface. The regime changes as a function of the barrier value:

For low values of the barrier Δ, charges accumulate in the first layer, adjacent to the metal surface due to the interactions with their image charges. This leads to a space-charge-limited current, associated to a charge-carrier density in the bulk being almost constant over all fields. As a result, (1) the current densities for the two lowest barrier values assumed in this work ($\Delta = 0.1$ and 0.2 eV) are essentially equal and (2) the current densities decrease with increasing disorder, due to a lowering of the bulk mobility as a result of traps. The model of Scott and Malliaras [9] is not able to account for this space charge effect. The model of Neumann *et al.* [12] considers the impact of charge accumulation at the contact but disregards the field- and disorder-dependence of the mobility entering the space-charge-limited current.

A second regime is established for high barrier values ($0.4 \leq \Delta \leq 0.7$ eV). There, the current density increases with disorder, due to a hopping of charges between the electrode and the first layer, which leads to an increase of the energy of nearby charges, which, as a result, get pushed into the bulk. This proximity effect is not covered by any macroscopic model known to the author. Also, a simple extension of the model of Scott

and Malliaras [9] to account for the proximity effect did not yield satisfying results for all fields, as this effect can be compensated by a second effect:
We have also learned from our comparison to the model of Scott and Malliaras [9], that the effective injection barrier is lowered by introducing disorder, which competes with a decreased mobility due to disorder. By augmenting the current density computed with the model of Scott and Malliaras [9] by a simple, field-independent exponential factor, we achieved noteworthy accordance with our simulations over the disorder range from $1 \, k_B \cdot T$ to $6 \, k_B \cdot T$ except for the highest field considered.

We also evaluated the electrostatic potential from the average charge-carrier density. However, we observe for intermediate fields and high disorder, that the uncertainty of the voltage drop across the model system exhibits more than 10%, and in selected cases, even larger. This makes comparison to the literature, such as Ref. [3] and Ref. [12] very difficult. Also the application of the calculated electrostatic potential $\Phi(x)$ in macroscopic models, such as drift-diffusion, is critical, (1), due to the high uncertainty and, (2), due to the inability to account for the proximity effect.

Hence, in order to exploit our results in a drift-diffusion model, the best way is, therefore, a simple look up table, that predicts a current density j as a function of the fields, disorder and barrier value, which delivers valid input values for a drift-diffusion model of the bulk region.

We note here the following list of future steps aiming at resuming and verifying our results:

1. Investigate the dependence on the temperature T.

2. Formulate criteria for establishing SCLC using parameters such as Δ, F_{ext} and T.

3. Explore the field-dependence of the barrier lowering,
   a) by considering more field values and possibly a larger range of F_{ext}, and
   b) by investigating the net current as a function of the site-energy at the position of the barrier-shape maximum.

4. Perform simulations to discriminate between the proximity effect and the disorder induced barrier lowering.

5. Explore the impact of tunnelling for large values of Δ.

6. Perform experiments to compare our results against.

7. Model inhomogeneous electrodes, as a more realistic approach to model real world devices.

8 Bibliography

1. U. Wolf, V. Arkhipov, and H. Bässler,
    "Current injection from a metal to a disordered hopping system. I. Monte Carlo simulation". *Physical Review B* **59,** 7507 (1999).

2. R. A. Marsh, C. Groves, and N. C. Greenham,
    "A microscopic model for the behavior of nanostructured organic photovoltaic devices". *Journal of Applied Physics* **101,** 083509 (2007).

3. J. van der Holst, F. van Oost, R. Coehoorn, and P. Bobbert,
    "Monte Carlo study of charge transport in organic sandwich-type single-carrier devices: Effects of Coulomb interactions". *Physical Review B* **83,** 1 (2011).

4. K. A. Fichthorn and W. H. Weinberg,
    "Theoretical foundations of dynamical Monte Carlo simulations". *The Journal of Chemical Physics* **95,** 1090 (1991).

5. S. K. Possanner, K. Zojer, P. Pacher, E. Zojer, and F. Schürrer,
    "Threshold Voltage Shifts in Organic Thin-Film Transistors Due to Self-Assembled Monolayers at the Dielectric Surface". *Advanced Functional Materials* **19,** 958 (2009).

6. A. F. Voter,
    "Introduction to the Kinetic Monte Carlo Method". *Radiation Effects* **235,** 1 (2005).

7. S. Sze, *Physics of Semiconductor Devices* (John Wiley & Sons, 1981).

8. M. Schwoerer and H. C. Wolf, *Organic Molecular Solids* (Wiley-VCH, 2007).

9. J. Scott and G. G. Malliaras,
    "Charge injection and recombination at the metal–organic interface". *Chemical Physics Letters* **299,** 115 (1999).

10. J. Barker, C. Ramsdale, and N. Greenham,
    "Modeling the current-voltage characteristics of bilayer polymer photovoltaic devices". *Physical Review B* **67,** 1 (2003).

11. V. Arkhipov, U. Wolf, and H. Bässler,
    "Current injection from a metal to a disordered hopping system. II. Comparison between analytic theory and simulation". *Physical Review B* **59,** 7514 (1999).

12. F. Neumann, Y. a. Genenko, C. Melzer, S. V. Yampolskii, and H. Von Seggern,
    "Self-consistent analytical solution of a problem of charge-carrier injection at a conductor/insulator interface". *Physical Review B - Condensed Matter and Materials Physics* **75,** 1 (2007).

13. Wikipedia, *Master equation — Wikipedia, The Free Encyclopedia* [Online; accessed 26-11-2014]. 2014. URL:
    `http://en.wikipedia.org/wiki/Master_equation`.

14. K. Jacobs. in *Stochastic Processes for Physicists* 127–150 (Cambridge Books Online, 2012).

15. J. van der Holst, "Three-dimensional modeling of charge transport, injection and recombination in organic light-emitting diodes", PhD thesis, TU Eindhoven (2010).

16. V. Coropceanu, J. Cornil, D. A. da Silva Filho, Y. Olivier, R. Silbey, and J.-L. Brédas, "Charge transport in organic semiconductors." *Chemical Reviews* **107,** 926 (2007).

17. A. R. Crofts, *Marcus theory* [Online; accessed 09-04-2015]. 2015. URL: `http://www.life.illinois.edu/crofts/bioph354/lect19.html`.

18. J. Zhou, Y. Zhou, J. Zhao, C. Wu, X. Ding, and X. Hou, "Carrier density dependence of mobility in organic solids: A Monte Carlo simulation". *Physical Review B* **75,** 153201 (2007).

19. V. Rühle, A. Lukyanov, F. May, M. Schrader, T. Vehoff, J. Kirkpatrick, B. Baumeier, and D. Andrienko, "Microscopic Simulations of Charge Transport in Disordered Organic Semiconductors." *Journal of Chemical Theory and Computation* **7,** 3335 (2011).

20. O. Stenzel, L. J. A. Koster, R. Thiedmann, S. D. Oosterhout, R. a. J. Janssen, and V. Schmidt, "A New Approach to Model-Based Simulation of Disordered Polymer Blend Solar Cells". *Advanced Functional Materials* **22,** 1236 (2012).

21. H. Wu, D. W. L. Sprung, and J. Martorell, "Potential energy of a point charge in a grounded conducting cavity". *European Journal of Physics* **21,** 413 (2000).

23. C. Groves, "Developing understanding of organic photovoltaic devices: kinetic Monte Carlo models of geminate and non-geminate recombination, charge transport and charge extraction". *Energy & Environmental Science* **6,** 3202 (2013).

24. H. G. Evertz, *Lecture Notes on Computer Simulations* University Lecture TU Graz. 2009.

25. R. G. E. Kimber, E. N. Wright, S. E. J. O'Kane, A. B. Walker, and J. C. Blakesley, "Mesoscopic kinetic Monte Carlo modeling of organic photovoltaic device characteristics". *Physical Review B* **86,** 235206 (2012).

26. W. Pasveer, J. Cottaar, C. Tanase, R. Coehoorn, P. Bobbert, P. Blom, D. de Leeuw, and M. Michels, "Unified Description of Charge-Carrier Mobilities in Disordered Semiconducting Polymers". *Physical Review Letters* **94,** 206601 (2005).

27. A. L. Burin and M. a. Ratner, "Charge injection into disordered molecular films". *Journal of Polymer Science, Part B: Polymer Physics* **41,** 2601 (2003).